# ON THE BEHAVIOR OF SPHERICAL AND NON-SPHERICAL GRAIN ASSEMBLIES, ITS MODELING AND NUMERICAL SIMULATION

THÈSE N$^{O}$ 3378 (2005)

PRÉSENTÉE À LA FACULTÉ SCIENCES DE BASE

Institut de mathématiques

SECTION DE MATHÉMATIQUES

ÉCOLE POLYTECHNIQUE FÉDÉRALE DE LAUSANNE

POUR L'OBTENTION DU GRADE DE DOCTEUR ÈS SCIENCES

PAR

Lionel POURNIN

ingénieur civil de l'Ecole des Mines de Nancy, France
et de nationalité française

acceptée sur proposition du jury:

Prof. Th. Liebling, directeur de thèse
Dr J.-A. Ferrez, rapporteur
Prof. S. Luding, rapporteur
Prof. A. Quarteroni, rapporteur
Prof. J. Rambau, rapporteur

Lausanne, EPFL
2005

# Acknowledgements

Since *acknowledgments* is an English word, I feel terribly encouraged to begin them as any reasonable frenchman would, *en Anglais*. Yet, this is not because I am reasonable, nor is it for the sake of tradition that I first think here to my supervisor, Thomas Liebling. He instigated this work, and without his guidance I would not have been able to write much of it. More than this, his kindness and humanity have been precious to me over the last few years. I wish to thank my referees, Jean-Albert Ferrez, Stefan Luding, Thomas Mountford, Alfio Quarteroni and Jörg Rambau for their careful reading of my thesis and their helpful comments. And since I am reasonable and French, I will go on writing in a more familiar way.

Je voudrais remercier ma famillle, mes sœurs, mes parents et ma grand-mère pour bien plus que ce que je ne pourrais formuler ici. Je pense aussi a Nicole, Denis, Emmanuelle et Véronique Gira. Merci pour votre soutien et votre amitié au travers de toutes ces années, dans les épreuves comme dans les moments de joie.

Cette page j'aurai pu l'écrire d'un petit coin vert de Roumanie, de Satu-Mare ou du pays de Oaş. Beaucoup des idées qui ont conduit à cette thèse ont été formulées là-bas, à Negreşti-Oaş et à Gherţa Mica. Imi e dor de acolo, şi de tine, Lum. Mulţumesc pentru tot.

Une autre de mes pensées ici est pour Frédéric qui dans sa Syrie adoptive, au monastère de Mar-Musa, se charge de la prière que trop souvent, la paresse me fait remplacer par un sommeil profond mais tout de même bien agréable.

Je pense aussi a ceux avec qui j'ai vecu durant les années qu'ont duré ma thèse, dont plusieurs générations de membres du ROSO. Je remercie particulièrement Marc-Olivier Boldi pour son amitié, Marco Ramaioli et Michel Tsukahara pour leur compagnie de tous les jours, mais aussi des statisticiens, géomètres, algébristes, peintres en batiment, bergers du Jura, banquiers genevois, petits patrons et chanteurs populaires : Christophe Osinski, Hugo Parlier, Gérard Maze, Sandrine Péché, Sylvain Sardy, Andrei Zenide, Jerôme Reboulleau et Roland Rozsnyo. Comment oublier ici le séminaire homonyme, réservé aux grandes personnes, et duquel on aurait pu dire (bien trop tard probablement) qu'il fût le ferment des grandes avancées de ce siècle ?

Je tiens a remercier quelques Mineurs de Nancy : Alain Mocellin à qui je dois ce parcours, mais aussi Guy Raguin, Matthieu Delost, Fabrice Morin et Géraldine Plas pour ces années pleines de rebondissements. Je pense aussi à toi, Romain, où que tu sois.

Last but not least, I would like to send some *greetings* to the members of a French demomaking-packing group, who made nice things on a famous 16-32bit computer between 1989 and 1993: Thierry Lemoult, Matthias Baillet, Christian Sabarot and Karim Ziouani.

This project was partially funded by the Swiss National Science Foundation, grant #200020-100499/1.

# Abstract

This thesis deals with the numerical modeling and simulation of granular media with large populations of non-spherical particles. Granular media are highly pervasive in nature and play an important role in technology. They are present in fields as diverse as civil engineering, food processing, and the pharmaceutical industry. For the physicist, they raise many challenging questions. They can behave like solids, as well as liquids or even gases and at times as none of these. Indeed, phenomena like granular segregation, arching effects or pattern formation are specific to granular media, hence often they are considered as a fourth state of matter.

Around the turn of the century, the increasing availability of large computers made it possible to start investigating granular matter by using numerical modeling and simulation. Most numerical models were originally designed to handle spherical particles. However, making it possible to process non-spherical particles has turned out to be of utmost importance. Indeed, it is such grains that one finds in nature and many important phenomena cannot be reproduced just using spherical grains. This is the motivation for the research of the present thesis.

Subjects in several fields are involved. The geometrical modeling of the particles and the simulation methods require discrete geometry results. A wide range of particle shapes is proposed. Those shapes, spheropolyhedra, are Minkowski sums of polyhedra and spheres and can be seen as smoothed polyhedra. Next, a contact detection algorithm is proposed that uses triangulations. This algorithm is a generalization of a method already available for spheres. It turns out that this algorithm relies on a positive answer to an open problem of computational geometry, the connectivity of the flip-graph of all triangulations. In this thesis it has been shown that the flip-graph of *regular* triangulations that share a same vertex set is connected.

The modeling of contacts requires physics. Again the contact model we propose is based on the existing molecular dynamics model for contacts between spheres. Those models turn out to be easily generalizable to smoothed polyhedra, which further motivates this choice of particle shape.

The implementation of those methods requires computer science. An implementation of this simulation methods for granular media composed of non-spherical particles was carried out based on the existing C++ code by J.-A. Ferrez that originally handled spherical particles.

The resulting simulation code was used to gain insight into the behavior of granular matter. Three experiments are presented that have been numerically carried out with our models. The first of these experiments deals with the flowability (i. e. the ability to flow) of powders. The flowability of bidisperse bead assemblies was found to depend only on their mass-average diameters. Next, an experiment of vibrating rods inside a cylindrical container shows that under appropriate conditions they will order vertically. Finally, experiments investigating the shape segregation of sheres and spherotetrahedra are perfomed. Unexpectedly they are found to mix.

# Résumé

Le sujet de cette thèse est la modélisation et la simulation numérique de milieux granulaires composés de grains non sphériques. Les matériaux granulaires abondent dans la nature et ont une place importante dans la technologie. On les trouve dans des domaines aussi divers que le génie civil, l'industrie agro-alimentaire ou l'industrie pharmaceutique. Pour le physicien, ils sont d'autre part la source de nombreuses questions.

A la fin du siècle dernier, l'augmentation de la puissance de calcul des ordinateurs a rendu possible l'utilisation de la simulation numérique pour l'étude les milieux granulaires. Au départ, la plupart des modèles numériques etaient développés pour traiter des particules sphériques. Pouvoir simuler des grains non-sphériques s'est révélé être d'une importance cruciale. En effet, les particules que l'on trouve dans la nature sont non-sphériques et un grand nombre de phénomènes importants ne peuvent pas êtres reproduits avec des grains spheriques. Ceci constitue la motivation de la recherche présentée dans cette thèse.

Il s'agit d'un travail pluridisciplinaire. La modélisation géométrique des particules et les méthodes de simulation se basent sur des résultats de géométrie algorithmique. Une grande variété de formes de particules est proposée. Ces formes ou spheropolyèdres, sont des sommes de Minkowski de polyèdres et de spheres et peuvent être vues comme des polyèdres lissés. Ensuite, un algorithme de détection des contacts utilisant des triangulations est proposée. Cet algorithme est la généralisation d'une méthode déjà implémentée pour les sphères. Il se trouve que la convergence de cet algorithme dépend de la réponse à un problème ouvert en géométrie algorithmique, la connexité du graphe des *flips* de toutes les triangulations. Dans cette thèse, la connexité du graphe des flips des triangulations régulières qui ont en commun leur ensemble de sommets a été démontrée.

La modélisation des contacts s'appuie sur la physique. Le modèle que nous proposons est basé sur les modèles de type dynamique moléculaire pour les contacts entre sphères. Ces modèles se généralisent facilement à nos polyèdres lissés, ce qui constitue une motivation de plus pour choisir cette famille de formes.

L'implémentation de ces méthodes pour des milieux granulaires composés de particules non-sphériques a été faite à partir du programme écrit en C++ par J.-A. Ferrez pour la simulation numérique de grains sphériques.

Ce programme a ensuite été utilisé pour étudier certains phénomènes liés aux milieux granulaires. Trois expériences ont été conduites numériquement avec nos modèles. Avec la première de ces expériences, la coulabilité des poudres, c'est-à-dire la facilité avec laquelle elles peuvent couler, a été étudiée. Il s'est trouvé que la coulabilité des ensembles de sphères bidisperses ne dépend que de leur diamètre moyen en masse. Ensuite, une expérience consistant a faire vibrer des particules alongées dans un container cylindrique montre que sous certaines conditions ces particules vont s'ordonner verticalement. Enfin, des expériences de ségrégation par formes de sphères et de sphérotétraèdres montrent que ces deux formes vont avoir tendance à se mélanger.

# Contents

**Introduction** **1**

Inter-particulate contact modeling . . . . . 2

Collision detection . . . . . 2

Is the flip-graph of regular triangulation connected ? . . . . . 3

Granular matter and numerical simulation . . . . . 3

**I Methods** **5**

**1 Mathematical preliminaries** **7**

1.1 Polyhedra and complexes . . . . . 7

1.2 On the flip-graph of regular triangulations . . . . . 10

1.2.1 Geometric bistellar operations . . . . . 11

1.2.2 Monotone connectivity of the graph of regular triangulations . . 12

1.3 Weighted Delaunay triangulations and power diagrams . . . . . 14

**2 The Distinct Element Method** **19**

2.1 A model for particle shapes . . . . . 20

2.1.1 Contacts and overlaps between particles . . . . . 21

2.2 Contact force modeling . . . . . 25

2.3 Tuning molecular dynamics models with real experiments . . . . . 27

**3 A triangulation-based contact detection method** **31**

3.1 Spherical particles . . . . . 31

3.2 Non-spherical particles . . . . . 32

3.2.1 Covering the particles with spheres . . . . . 33

3.3 Building and handling the triangulation . . . . . 38

3.3.1 Building the initial triangulation . . . . . 38

3.3.2 Triangulation Maintenance . . . . . 39

**4 Some implementation details** **41**

4.1 Intoduction . . . . . 41

4.2 Structure of the simulation environment . . . . . 42

4.3 Enhancing the robustness of triangulation maintenance . . . . . 44

4.4 Experimental complexity analysis . . . . . 46

4.5 Some inertia matrices . . . . . 49

4.5.1 Inertia matrix estimation . . . . . 50

4.5.2 Exact inertia matrices of some spherosimplices . . . . . 51

**II Applications** **55**

**5 A Study of Arching Effects and Flowability** **57**

5.1 The flowability experiment . . . . . 58

5.2 The mean critical diameter of a granular piling . . . . . 59

5.3 The influence of friction . . . . . 62

5.4 Flowability of bidisperse granular media . . . . . 64

5.5 Conclusions . . . . . 65

**6 Spherocylinder Crystallization** **67**

6.1 The Experiments . . . . . 67

6.2 Crystallization mechanisms . . . . . 68

**7 On the segregation of spheres and tetrahedra** **75**

7.1 The experiments . . . . . 76

7.2 Results and discussion . . . . . 77

7.3 Conclusion . . . . . 82

**Conclusion** **83**

**Bibliography** **85**

# Introduction

This thesis deals with the numerical modeling and simulation of granular media with large populations of non-spherical particles. Granular materials are constituted of solid bodies that are large enough for mutual microscopical interactions to be negligible. They can behave like solids, as well as liquids or even gases and at times as none of these. Granular media are therefore said by some to constitute a fourth state of matter. Indeed, a grain assembly will undergo anisotropic stresses at rest, flow when submitted to external forces and fill all available volume under sufficient agitation. However, the stresses inside a granular piling are far from homogeneous [LNS+95], granular flows will be confined to a boundary layer at the free surface of a sand pile [AD99] and granular gases can show clustering [MY96]. One of the major concerns of material engineers is to link microscopic and macroscopic scales, in order to understand how observable macroscopic behaviors derive from microscopic phenomena. While this link is quite well understood and described for solids, liquids and gases, nothing comparable exists for granular matter so far. This alone is more than enough to arouse the interest of scientists. What is further appealing in their study is that granular media constitute a good portion of all materials handled by man, in factories for example. The need to understand the physics of granular matter is therefore not only due to the curiosity natural to scientific minds but also comes from the industrial world.

Around the turn of the century, the increasing availability of large computers made it possible to start investigating granular matter by using numerical modeling and simulation. Among many other advantages, this technique allows to check the validity of microscopic granular interaction models using macroscopical experiments. Another advantage is that some of the limitations particular to usual real-world experiments disappear. Indeed, almost any experiment is feasible and any parameter can be measured in a numerical framework. However, numerical simulation methods suffer from the limitation of computing power. Their main drawback though, is that they strongly rely on the model chosen for grain-grain interactions, which most of the time shows strong inaccuracies in given situations [MY92; LCB+94]. Most numerical models were originally designed to handle spherical particles. However, making it possible to process non-spherical particles has turned out to be of utmost importance. Indeed, it is such grains that one finds in nature and many important phenomena cannot be reproduced just using spherical grains.

This thesis is organized in two parts. The first one describes the tools and methods that we use to model non-spherical grains and to handle them numerically (chapters 1, 2, 3, 4). The second part features three experiments that have been carried out with our

models. Those experiments investigate some quite unexpected phenomena related to granular matter (chapters 5, 6, 7).

## Inter-particulate contact modeling

Among the available methods for contact modeling, one finds *event-driven* (ED) methods, *molecular dynamics* (MD) and *contact dynamics* (CD) as sub-categories of the *distinct element method* (DEM). While the medium is treated as a sequence of instantaneous collisions in event driven methods, with methods using molecular dynamics, the system is driven by explicit inter-particulate forces. On the contrary, the explicit parameter in contact dynamics is displacement. In this thesis, we focus exclusively on the molecular dynamics method. This method was originally designed to handle spherical particles. In chapter 2, the reader will find a generalization of the distinct element method to a wide range of non-spherical particles. This is a subject to which researchers have been showing a growing interest over the past few years. Alternate ways to handle non-spherical particles can be found in [O'C96; MLH00; MMEL04; MEL05].

## Collision detection

Granular media simulation does not only require realistic physical contact modeling but also efficient contact detection algorithms. Indeed, in order to apply contact models, one first needs to determine which are the pairs of contacting particles. The complexity of naive contact detection methods is quadratic. This becomes quickly prohibitive when large populations of particles need to be simulated. The question of detecting contacting objects is not specific to numerical simulation. Geometric modeling, computer graphics and robotics require efficient contact detection methods as well for their own purposes. Most contact detection methods are found in [AT87]. The most widely used among those are spacial subdivision methods. The idea underlying to those methods is to cut space into cells and to check for contact inside each cell and between neighboring cells. The way the cells should be laid out and handled (cell size, adaptive subdivision) leads to a wide range of algorithms [SSW00; Sam84]. Other methods keep track of neighbors lying inside a bounded area surrounding each particle [Sch99; MMEL04; MEL05]. The contact detection method we use here was first implemented by D. Müller [ML95; Mül96a] for discs and polygons in two dimensions and extended to three dimensional spheres by J. A. Ferrez [Fer01; FL02]. The method relies on *constrained triangulations* for polygonal particles and *weighted Delaunay triangulations* (otherwise called *regular triangulations*) for discs and spheres. Those triangulations have the nice property that they provide informations about inter-particle distances among a set of spheres. The reader will find an extension of this triangulation-based algorithm to non-spherical particles in chapter 3. The proof that this method theoretically works, either for spheres and non spherical particles is presented in chapter 1. A discussion of the practical complexity of the method will be found in chapter 4.

## Is the flip-graph of regular triangulation connected ?

By its very nature, our triangulation-based contact detection method heavily uses results from computational geometry. It turns out that some of the regularization algorithms presented in chapters 3 and 4 rely on a positive answer to an open problem (see [DMO05]). The general question is : is it possible to transform a triangulation of a given point set into another triangulation of the same point set by only using local transformations (called flips) that do not add or delete vertices ? This question is usually formulated in terms of a particular graph called *flip-graph*. While the general case remains open, the answer is yes in two dimensions [Law77], no in dimensions above six [San00a]. Moreover, if has been shown in [GZK90] that all *regular* triangulations are connected by flips, if we allow for the deletion and addition of vertices. In the context, the contribution of this thesis is the proof that two regular triangulations sharing the same vertex set are connected by flips that do not add nor delete vertices (chapter 1) so that all the intermediate triangulations are regular.

## Granular matter and numerical simulation

The second part of this thesis is devoted to experiments on granular media that have been carried out numerically. Chapter 5 presents a study of the ability of bead assemblies to flow. Chapter 6, reports on granular crystallization of elongated particles submitted to vertical vibrations. This numerical findings correspond to experimental observations from [VLMJ00] and constitutes a validation of our simulation techniques. The reader will finally find a study of the shape-segregation of mixtures of spheres and tetrahedra in chapter 7. We observe that spheres and tetrahedra with same volume and density tend to mix which is not what one would have expected from granular materials.

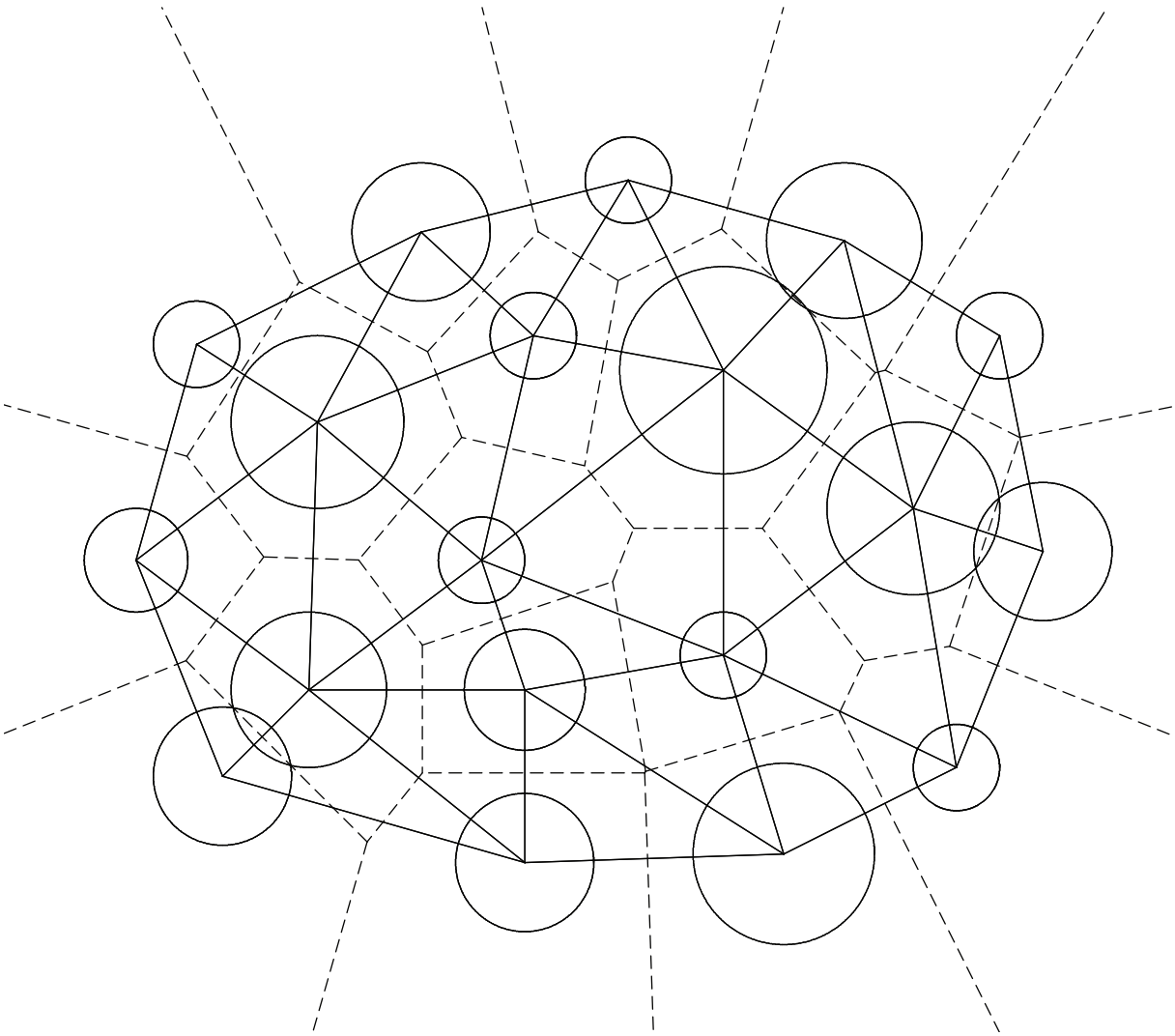

# Part I

# Methods

# Chapter 1

# Mathematical preliminaries

The particular simulation method for granular media proposed in this thesis relies on the properties of simple geometrical objects as polyhedra and triangulations. Indeed, the particle shapes this method handles can be described as smoothed polyhedra. Moreover, the method to detect the pairs of contacting particles will use the regularity properties of a particular class of triangulations, known as either "weighted Delaunay triangulations" or "regular triangulations".

The reader will find the definitions of those geometrical objects in this chapter, as well as those properties that are useful for contact modeling (chapter 2) and contact detection algorithms (chapter 3). Sections 1.1 and 1.3 introduce the formalism in $\mathbb{R}^d$ for $d \in \mathbb{N}$, since all definitions can be stated in any dimension. Still our natural framework is $\mathbb{R}^3$ and this chapter also can be read replacing $d$ by 3. Section 1.2 presents theoretical results about a geometrical problem that happen to be crucial for the regularization of the triangulations used in the contact detection method (chapter 3).

## 1.1 Polyhedra and complexes

We denote $\mathrm{conv}(p)$ the convex hull of a subset $p$ of $\mathbb{R}^d$ and $\mathrm{aff}(p)$ its affine hull. If $A$ and $B$ are collections of subsets of $\mathbb{R}^d$, the set $\{\mathrm{conv}(p \cup q) : (p,q) \in A \times B\}$ is denoted by $A \star B$. We denote by $x.y$ the Euclidean scalar product of two vectors $x$ and $y$, by $\|x\|$ the Euclidean norm of a vector $x$ and by $|\lambda|$ the absolute value of a scalar $\lambda$.

A *polyhedron* is the intersection of finitely many closed affine halfspaces. The *dimension* of a polyhedron $p$, denoted by $\dim(p)$ is the dimension of its affine hull. A *face* of $p$ either is the empty set, $p$ itself, or its intersection with a supporting hyperplane [BY95]. Observe that faces of a polyhedron are polyhedra. We call *dimension* of a face its dimension as a polyhedron. The faces of a polyhedron $p$ of dimension $\dim(p) - 1$ will be called *facets* and those of dimension 0 will be called *vertices*. The vertex set of a polyhedron $p$ will be denoted by $\mathcal{V}(p)$.

A *cone* is the intersection of finitely many closed linear halfspaces and as such it is a particular case of polyhedron. A *polytope* is a bounded polyhedron. A *simplex* $s$ is a polytope whose vertex set is affinely independent. It proceeds from the following proposition that a polytope is the convex hull of its vertex set. This is a classical result in geometry, which detailed proof can be found in [BY95].

**Proposition 1.** *A polytope is the convex hull of finitely many points.*

Polyhedra will be the basic elements constituting polyhedral complexes, according to the following definition :

**Definition 1.** *We call polyhedral complex in $\mathbb{R}^d$ a set $C$ of polyhedra of $\mathbb{R}^d$ so that all pairs $(p,q) \in C^2$ satisfy the two following statements :*

*i)* $p \cap q$ *belongs to* $C$.

*ii)* $p \cap q$ *is a common face of* $p$ *and* $q$.

The elements of a polyhedral complex $C$ will be called *faces* of $C$. We call *underlying space* of $C$ and denote by $\mathrm{dom}(C)$ the pointwise union of its faces. We call *dimension* of $C$ and denote by $\dim(C)$ the dimension of its underlying space's affine hull. A face whose dimension is that of $C$ is called a *cell* of $C$, a face whose dimension is $dim(C) - 1$ is called a *facet* of $C$ and a face of dimension 0 is called a *vertex* of $C$. We denote by $\mathcal{V}_C$ the set of all vertices of the polyhedral complex $C$.

We call *fan* in $\mathbb{R}^d$ a polyhedral complex in $\mathbb{R}^d$ whose faces are cones. A fan in $\mathbb{R}^d$ is *complete* if its underlying space is $\mathbb{R}^d$. Now we introduce particular polyhedral complexes related to finite point sets. We call *point configuration* any finite subset $\mathcal{A}$ of $\mathbb{R}^d$. The set of all polytopes whose vertices are in $\mathcal{A}$ is denoted by $\mathcal{P}_\mathcal{A}$.

**Definition 2.** *A polyhedral subdivision of a point configuration $\mathcal{A}$ is a subset of $\mathcal{P}_\mathcal{A}$ which is a polyhedral complex and whose underlying space is $conv(\mathcal{A})$.*

We call *triangulation* of a point configuration $\mathcal{A}$ any polyhedral subdivision $T$ of $\mathcal{A}$ whose faces are simplices. As an example, figure 1.1 shows a point configuration and two of its triangulations.

A face $f$ of $T$ is called *interior* if it intersects the relative interior of $\mathrm{dom}(T)$. For a face $s$ of a triangulation $T$, we call *star* of $s$ in $T$ the set $\{p \in T : \mathrm{conv}(s \cup p) \in T\}$ and *link* of $s$ in $T$ the set $\{p \in T : \mathrm{conv}(s \cup p) \in T, s \not\subset p\}$. Let $\mathcal{A}$ be a point configuration of $\mathbb{R}^d$. A *height function* on $\mathcal{A}$ is any function $w : \mathcal{A} \to \mathbb{R}$. Height functions induce particular polyhedral subdivisions of their underlying point configurations according to the following proposition :

**Proposition 2.** *Let $\mathcal{A}$ be a point configuration of $\mathbb{R}^d$ and $w$ a height function on $\mathcal{A}$. There is a unique polyhedral subdivision $T(\mathcal{A},w)$ of $\mathcal{A}$ so that for all $p \in T(\mathcal{A},w)$, there exists $y \in \mathbb{R}^d$ satisfying the following two statements :*

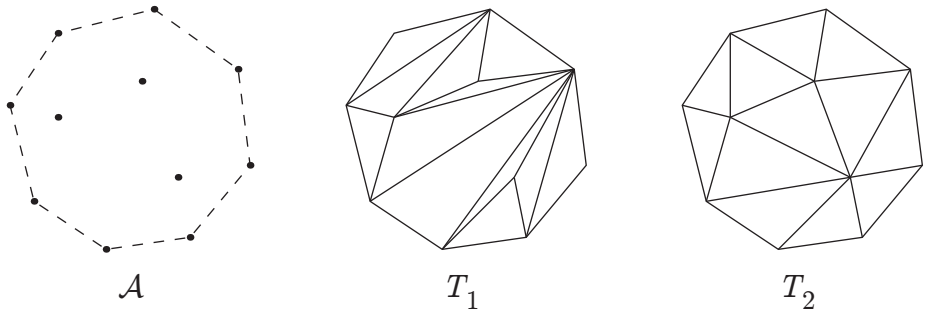


Figure 1.1: A point set $\mathcal{A}$ in the plane and two of its triangulations $T_1$ and $T_2$.

*i) For all $a \in \mathcal{V}(p)$, $a.y = w(a)$.*

*ii) For all $a \in \mathcal{A} \setminus \mathcal{V}(p)$, $a.y < w(a)$.*

For all $a \in \mathcal{A}$, call $a^w$ the point $(a, w(a)) \in \mathbb{R}^{d+1}$. The faces of $T(\mathcal{A}, w)$ can actually be obtained by projecting the lower faces of the polytope $\text{conv}(\{a^w : a \in \mathcal{A}\})$ back on $\mathbb{R}^d$. Polyhedral subdivisions that can be constructed in this way exhibit particular regularity properties [dLRS04], which earns them to be denominated accordingly :

**Definition 3.** *A polyhedral subdivision $T$ of a point configuration $\mathcal{A}$ is called regular if there exists a height function $w$ so that $T = T(\mathcal{A}, w)$. In this case we say that $w$ realizes $T$.*

Observe that not all subdivisions of a point configuration are regular. The usual example of a triangulation that is not regular is shown on figure 1.2. This particular triangulation is actually what one can see when looking at Schönhardt's polyhedron [Sch28; Ramar] from the top.

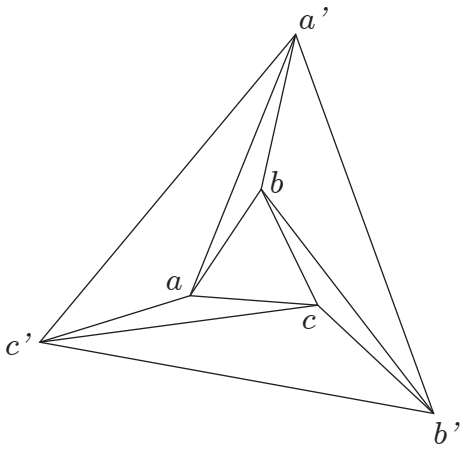


Figure 1.2: A non-regular triangulation, commonly referred to as "mother of all examples".

## 1.2 On the flip-graph of regular triangulations

In the method described in chapter 3, a way to regularize triangulations will be needed. The problem can be stated as follows. Let $(S_i)_{1\leq i\leq n}$ be a set of spheres with centers $(R_i)_{1\leq i\leq n}$. Provided a triangulation $T$ of the point configuration $\mathcal{A} = \{x_i : 1 \leq i \leq n\}$ is known, one needs to transform $T$ into the weighted Delaunay triangulation generated by $(S_i)_{1\leq i\leq n}$ at the lowest possible cost.

In order to proceed to this regularization, we will use local transformations called geometric bistellar flips, or simply flips, as shown on figure 1.4. The two dimensional flip of figure 1.4a) amounts to exchange the diagonals of a convex quadrilateral. The analogous tridimensional flip is that of figure 1.4d) and exchanges 1 edge, 3 triangles and 3 tetrahedra for 1 triangle and 2 tetrahedra. Locally performing those flips within a triangulation will produce different triangulations of a given point configuration. As an example, figure 1.3 shows a way to obtain one triangulation of figure 1.1 from the other by successive flips. This problem of changing a triangulation into another by performing flips can be formulated for point sets in any dimensions. This demands proper definitions of both triangulations and flips which will be given in the following.

A crucial object here is the flip-graph of all triangulations of a point configuration $\mathcal{A}$. This graph has the triangulations of $\mathcal{A}$ as vertices and the flips between those triangulations as edges. It is connected if it is possible to change a triangulation into any other one by performing flips. It has been shown [Law77] that two dimensional point configurations are always linked by a succession of flips. However, according to [San00a], there are six-dimensional point configurations whose flip-graph is disconnected. For point sets in dimensions three to five, the connectivity of this graph is still subject to investigations, though there are some results bounding the degree of its vertices [dLSU99; San00a; San00b].

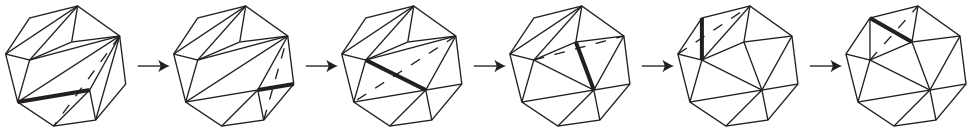

Figure 1.3: A sequence a flips connecting triangulations $T_1$ and $T_2$ of figure 1.1. Dashed lines show the edges that are flipped out and bold ones show the edges that are flipped in.

The subgraph induced by regular triangulations in the flip-graph is the 1-skeleton of the secondary polytope introduced in [GZK90]. As such, the flip-graph of regular triangulations exhibits a very nice intuitive structure. In particular, it is connected [GZK90; GKZ94]. The reader should refer to [dLRS04] for a comprehensive explanation on the subject.

This section report results about particular paths in the flip-graph of regular triangulations. Those results can also be found in [PL05b]. As follows from the above definition of triangulations, not all points in a point configuration $\mathcal{A}$ need be vertices of a triangulation of $\mathcal{A}$. Moreover, figures 1.4b) and 1.4c) show that some flips make points

appear or disappear in the triangulation. It is possible to flip a triangulation of a point configuration to another by going through triangulations whose vertex sets are quite different. Indeed, the only points strictly required as vertices for any triangulation of $\mathcal{A}$ are the extreme points of the convex hull of $\mathcal{A}$. Theorem 3 states that when flipping a regular triangulation into another whose vertex set is a subset of the first, it is possible to keep monotone the number of vertices of the triangulations met in the process. As a corollary, the flip-graph of regular triangulations whose vertex sets are identical is connected. This connectivity property actually reveals crucial for our contact detection method (see chapter 3), where the vertices of the triangulation represent particles. Deleting those vertices while a simulation proccesses is therefore inappropriate in this case.

### 1.2.1 Geometric bistellar operations

The notion of flip has been illustrated in the introduction by the two dimensional example of figure 1.4a) that consists in exchanging the diagonals of a convex quadrilateral. Observe that the flip shown in figure 1.4b) exhibits a different structure, as it makes a vertex appear or disappear. Degenerate cases may occur as well, like the flip of figure 1.4c) where five vertices are involved, three of them being aligned, and one of them appearing or disappearing depending on the triangulation in which the flip is performed. The simplest three-dimensional flip, shown in figure 1.4d) consists in exchanging two tetrahedra and a triangle for three tetrahedra, three triangles and an edge. Of course, flips analogous to those of figures 1.4b) and 1.4c) also exist in three dimensions. In this section, we give a definition in any dimension of those geometric bistellar operations, thus gathering the flips of figure 1.4 into one unique description.

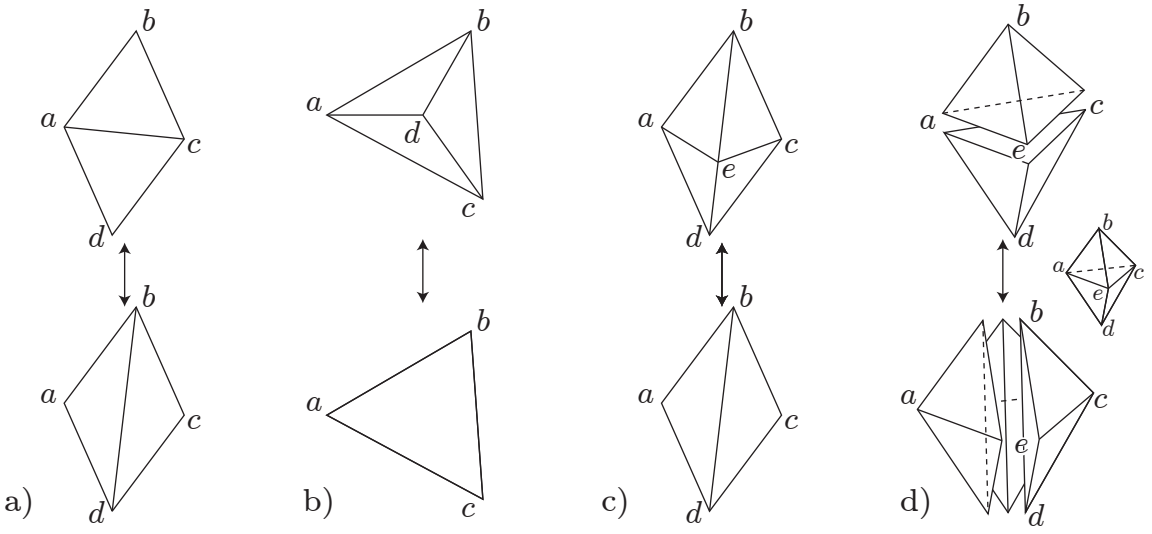


Figure 1.4: Some flips

We call *circuit* any minimal affinely dependent subset $Z$ of $\mathbb{R}^d$ and for a point configuration $\mathcal{A}$, we denote by $\mathcal{C}_\mathcal{A}$ the set of all circuits $Z \subset \mathcal{A}$. The set $\{a,b,c,d\}$ is a circuit in figures 1.4a) and 1.4b) and $\{b,d,e\}$ is one in figure 1.4c). A circuit admits exactly

two triangulations. This comes from the existence of the so-called *Radon partition* of circuits, according to the following theorem :

**Theorem 1.** *Let $Z \subset \mathbb{R}^d$ be a circuit. There exists a unique partition $(Z_-, Z_+)$ of $Z$ so that $conv(Z_-) \cap conv(Z_+) \neq \emptyset$.*

Let $(Z_-, Z_+)$ be the Radon partition of a circuit $Z$ and consider the two subsets of $\mathcal{P}_Z$ defined by $T_- = \{s \in \mathcal{P}_Z : Z_- \not\subset s\}$ and $T_+ = \{s \in \mathcal{P}_Z : Z_+ \not\subset s\}$. Every simplex in $\mathcal{P}_Z$ either belongs to $T_-$ or to $T_+$. Moreover, one can check that both $T_-$ and $T_+$ are triangulations by using the unicity of $(Z_-, Z_+)$ as a partition of $Z$ so that $\text{conv}(Z_-) \cap \text{conv}(Z_+) \neq \emptyset$. This proves that $Z$ admits $T_-$ and $T_+$ as its only two triangulations. While knowing that a circuit admits exactly two triangulations is not strictly required to proceed with the definition of flips, it helps to understand the structure of circuits, which are the minimal point configurations admitting more than one triangulation.

**Definition 4.** *Let $T$ be a triangulation of a point configuration $\mathcal{A}$. Suppose the two following statements are satisfied by some circuit $Z \subset \mathcal{A}$ :*

*i) Some triangulation $T_-$ of $Z$ is a subcomplex of $T$.*

*ii) All cells of $T_-$ have the same link $L$ in $T$.*

*Then, we say that $Z$ is a flippable circuit in $T$. Moreover, a triangulation $T'$ of $\mathcal{A}$ can be obtained by replacing $T_- \star L$ by $T_+ \star L$ in $T$. This operation is called a geometric bistellar flip and we say that $T$ and $T'$ are geometric bistellar neighbors.*

Observe on figures 1.4a) and 1.4b) that $\{a, b, c, d\}$ are flippable circuits, the link $L$ stated in ii) being empty. On figure 1.4c), however, $\{b, d, e\}$ is a flippable circuit with $L = \{a, c\}$. Actually, statement ii) will only be useful when the circuit to be flipped is not full-dimensional, the flip itself being degenerate as that of figure 1.4c).

### 1.2.2 Monotone connectivity of the graph of regular triangulations

Let $\mathcal{A}$ be a configuration of $n$ points in $\mathbb{R}^d$. Since the space of height functions on $\mathcal{A}$ is a vector space of dimension $n$, we will identify it with $\mathbb{R}^n$ from now on. For a given regular polyhedral subdivision $T$ of $\mathcal{A}$, we denote by $\mathcal{C}_{\mathcal{A}}(T)$ the set $\{w \in \mathbb{R}^n : T = T(\mathcal{A}, w)\}$ of all height functions realizing $T$. We further denote by $\mathcal{C}_{\mathcal{A}}$ the collection of the $\mathcal{C}_{\mathcal{A}}(T)$ over all regular polyhedral subdivisions $T$ of $\mathcal{A}$. The following proposition is proven in [GZK90] :

**Proposition 3.** *The set $\mathcal{C}_{\mathcal{A}}$ is a complete polyhedral fan. Moreover, for a regular polyhedral subdivision $T$ of $\mathcal{A}$, the polyhedral cone $\mathcal{C}_{\mathcal{A}}(T)$ is full-dimensional if and only if $T$ is a triangulation.*

The fan $\mathcal{C}_{\mathcal{A}}$ is called *secondary fan* of $\mathcal{A}$, and for a regular polyhedral subdivision $T$ of $\mathcal{A}$, the cone $\mathcal{C}_{\mathcal{A}}(T)$ is referred to as *secondary cone* of $T$. The following theorem states a crucial property of the secondary fan. Its proof can be found in [dLRS04] :

**Theorem 2.** *Two regular triangulations $T$ and $T'$ of a point configuration $\mathcal{A}$ are geometric bistellar neighbors if and only if their secondary cones share a common facet.*

To these results, we now add another one which will be used in the proof of theorem 3 to make sure that the sequence of triangulations we search for is monotone. For any point $a \in \mathcal{A}$ we call $\mathcal{K}_{\mathcal{A}}(a)$ the set $\{w \in \mathbb{R}^n : a \in T(\mathcal{A}, w)\}$ of all height functions whose induced polyhedral subdivisions of $\mathcal{A}$ admit $a$ as a vertex.

**Lemma 1.** *Let $\mathcal{A} \subset \mathbb{R}^d$ be a point configuration. For all $a \in \mathcal{A}$, the set $\mathcal{K}_{\mathcal{A}}(a)$ is convex.*

*Proof.* Let $w$ and $w'$ be two elements of $\mathcal{K}_{\mathcal{A}}(a)$ and $\lambda$ an element of $[0,1]$. We will show that $w'' = \lambda w + (1-\lambda)w'$ still belongs to $\mathcal{K}_{\mathcal{A}}(a)$. According to proposition 2, there exist two vectors $y$ and $y'$ in $\mathbb{R}^d$ so that $y.a = w(a)$ and $y'.a = w'(a)$ while for all $v \in \mathcal{A} \setminus \{a\}$, $y.v < w(v)$ and $y'.v < w'(v)$. Call $y''$ the vector $\lambda y + (1-\lambda)y' \in \mathbb{R}^d$. By linearity of the scalar product, one finds $y''.a = w''(a)$ while for all $v \in \mathcal{A} \setminus \{a\}$, $y''.v < w''(v)$. It follows from proposition 2 that $a$ is a vertex of $T(\mathcal{A}, w'')$, which proves that $\mathcal{K}_{\mathcal{A}}(a)$ is convex. □

Actually, for $a \in \mathcal{A}$ the set $\mathcal{K}_{\mathcal{A}}(a)$ is a full-dimensional open polyhedral cone. However, we only need its convexity here which explains the way lemma 1 has been stated. We are now ready to prove our main result :

**Theorem 3.** *Let $\mathcal{A} \subset \mathbb{R}^d$ be a point configuration. Let $T$ and $T'$ be regular triangulations of $\mathcal{A}$ so that $\mathcal{V}(T') \subset \mathcal{V}(T)$. Then there exists a finite sequence $T_0$, ..., $T_n$ of regular triangulations of $\mathcal{A}$ so that $T = T_0$, $T' = T_n$ and for any $i \in \{0, \ldots, n-1\}$,*

*i) $T_i$ and $T_{i+1}$ are geometric bistellar neighbors.*

*ii) $\mathcal{V}_{T_{i+1}} \subset \mathcal{V}_{T_i}$.*

*Proof.* Observe that any regular triangulation of $\mathcal{V}(T)$ is a regular triangulation of $\mathcal{A}$. We can therefore assume without loss of generality that $\mathcal{A} = \mathcal{V}(T)$.

According to proposition 3, the cones $\mathcal{C}_{\mathcal{A}}(T)$ and $\mathcal{C}_{\mathcal{A}}(T')$ are full dimensional and as such, their interiors are not empty. Observe that it is then possible to choose two height functions $w$ and $w'$ in the interiors of $\mathcal{C}_{\mathcal{A}}(T)$ and $\mathcal{C}_{\mathcal{A}}(T')$ respectively so that all faces of $\mathcal{C}_{\mathcal{A}}$ intercepted by segment $\mathrm{conv}(w, w')$ either are facets or cells. Let $(w, w')$ be such a pair of height functions.

We denote by $T_0$, ...., $T_n$ the sequence of regular triangulations of $\mathcal{A}$ so that $\mathcal{C}_{\mathcal{A}}(T_0)$, ..., $\mathcal{C}_{\mathcal{A}}(T_n)$ are those cells of $\mathcal{C}_{\mathcal{A}}$ successively met when $\mathrm{conv}(w, w')$ is traversed from $w$ to $w'$. Observe that $T_0 = T$ and $T_n = T'$. For any $i \in \{0, \ldots, n-1\}$, according to the way $(w, w')$ was chosen, the secondary cones $\mathcal{C}_{\mathcal{A}}(T_i)$ and $\mathcal{C}_{\mathcal{A}}(T_{i+1})$ share a common facet. Theorem 2 then makes sure that triangulations $T_0$, ...., $T_n$ satisfy statement i).

For any $i \in \{0, \ldots, n-1\}$, let $a$ be a vertex of $T_{i+1}$. Since $a$ is a vertex of $T_0$ as well, the convexity of $\{w \in \mathbb{R}^n : a \in T(\mathcal{A}, w)\}$ provided by lemma 1 implies that $a$ is a vertex of $T_i$. Triangulations $T_0$, ...., $T_n$ then satisfy statement ii) and the theorem is proven. □

While theorem 3 is the main result of this section, we now state a corollary that may be more appealing for it asserts the connectivity of some subgraphs of the flip-graph of regular triangulations. This result is particularly interesting for practical applications, and in particular for the contact detection method described in chapter 3. Indeed, the vertices of a triangulation represent the particles, therefore deleting them in the course of the simulation is inappropriate.

**Corollary 1.** *Let $\mathcal{A}$ be a point configuration in $\mathbb{R}^d$. The flip-graph of those regular triangulations of $\mathcal{A}$ that share $\mathcal{A}$ as a common vertex set is connected.*

## 1.3 Weighted Delaunay triangulations and power diagrams

Previous sections introduce regular triangulations by using height functions. This section presents another way to look at that particular class of triangulations, using the formalism of power diagrams. This formalism makes it possible to derive some of their properties that will be used in chapter 3, such as their ability to evaluate distances between neighbors among an assembly of spheres.

Assume $(S_i)_{1\leq i\leq n}$ is an assembly of $n$ spheres in $\mathbb{R}^d$ whith centers $(x_i)_{1\leq i\leq n}$ and radii $(R_i)_{1\leq i\leq n}$. Consider the *power distance* $\pi_i$ to the sphere $S_i$ defined on $\mathbb{R}^d$ by :

$$\pi_i : \begin{array}{ccc} \mathbb{R}^d & \rightarrow & \mathbb{R}, \\ x & \mapsto & \|x - x_i\|^2 - R_i^2. \end{array} \tag{1.1}$$

When $x$ lies outside $S_i$, $\pi_i(x)$ is the square of the distance between point $x$ and sphere $S_i$ measured along a line tangent to $S_i$, as figure 1.5 suggests. Now, call $p_i$ the subset of $\mathbb{R}^d$ constituted by points $x$ so that for all $j \neq i$, $\pi_i(x) \leq \pi_j(x)$. The $(p_i)_{1\leq i\leq n}$ happen to be polyhedra which are the cells of a polyhedral complex $C$ called *power diagram* or sometimes *Laguerre complex* generated by the spheres $S_1$, ..., $S_n$. Such a power diagram is shown on figure 1.6 in two dimensions. More details about power diagrams, and particularly proofs of above assertions can be found in [BY95].

The power diagram $C$ generated by spheres $(S_i)_{1\leq i\leq n}$ happens to be a geometrical dual of a particular regular triangulation of the point configuration $\mathcal{A} = \{x_i : 1 \leq i \leq n\}$. Indeed, for each face $p$ of $C((S_i)_{1\leq i\leq n})$, consider the polyhedron $p^*$ whose vertices are those $x_i$ so that $p$ is a face of $C_i$. The set $\{p^* : p \in C\}$ is then a polyhedral subdivision of $\mathcal{A}$ (see [BY95] for proofs). Moreover, this subdivision is realized by the following height function :

$$w : \begin{array}{ccc} \mathcal{A} & \rightarrow & \mathbb{R}, \\ x_i & \mapsto & \|x_i\|^2 - R_i^2. \end{array} \tag{1.2}$$

Thus, $\{p^* : p \in C\}$ is a regular subdivision of $\mathcal{A}$. When $w$ is in general position, $\{p^* : p \in C\}$ is a regular triangulation called *weighted Delaunay triangulation* generated

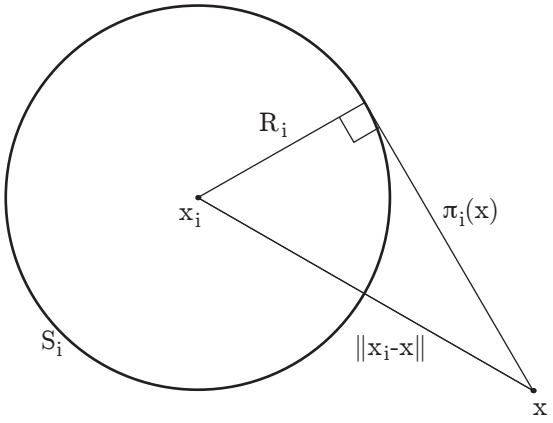


Figure 1.5: The power distance of point $x$ with respect to sphere $S_i$.

by the spheres $(S_i)_{1\leq i\leq n}$. We say that the spheres $(S_i)_{1\leq i\leq n}$ are in *general position* whenever the height function (1.2) they provide is in general position. Figure 1.6 depicts the weighted Delaunay triangulation corresponding to the power diagram already mentioned above in two dimensions.

We say that two spheres $S_i$ and $S_j$ are *less than orthogonal* if $\|x_j - x_i\|^2 > R_i^2 + R_j^2$. This condition, forbids spheres $S_i$ and $S_j$ to overlap too much. More precisely, their overlap should be strictly lower than in the case where they are orthogonal. We call *orthogonality condition* the following condition on the spheres $(S_i)_{1\leq i\leq n}$ :

$$\forall (i,j) \in \{1,...,n\}^2, i \neq j \Rightarrow \|x_j - x_i\|^2 > R_i^2 + R_j^2. \tag{1.3}$$

Whenever this condition is satisfied, the weighted Delaunay triangulation generated by the spheres $(S_i)_{1\leq i\leq n}$ is able to provide all the intersecting pairs among those spheres, according to the following theorem :

**Theorem 4.** *Let $(S_i)_{1\leq i\leq n}$ be a set of spheres in general position that satisfy the orthogonality condition (1.3). For any $i \neq j$, if spheres $S_i$ and $S_j$ intersect then $conv(\{x_i, x_j\})$ is a face of the weighted Delaunay triangulation generated by $(S_i)_{1\leq i\leq n}$.*

*Proof.* Suppose that $S_i$ and $S_j$ intersect and consider $k \in \{1,...,n\} \setminus \{i,j\}$. Call $x$ the point in $\text{conv}(\{x_i, x_j\})$ so that $\pi_i(x) = \pi_j(x)$. As the pair $(S_i, S_k)$ is less than orthogonal, we have $\|x_k - x_i\|^2 > R_i^2 + R_k^2$. Introducing $x$ in the left hand side of this inequation and developing the scalar product, one finds $\pi_k(x) + \pi_i(x) > 2(x_k - x).(x_i - x)$. The same arguments hold for the pair $(S_j, S_k)$ and we obtain the following system :

$$\begin{cases} \pi_i(x) + \pi_k(x) & > & 2(x_k - x).(x_i - x) \\ \pi_j(x) + \pi_k(x) & > & 2(x_k - x).(x_j - x) \end{cases} \tag{1.4}$$

Since spheres $S_i$ and $S_j$ intersect, $x$ lies inside both of them, which implies that $\pi_i(x) \leq 0$ and $\pi_j(x) \leq 0$. From inequations (1.4), $\pi_k(x)$ is then strictly greater than both $2(x_k -$

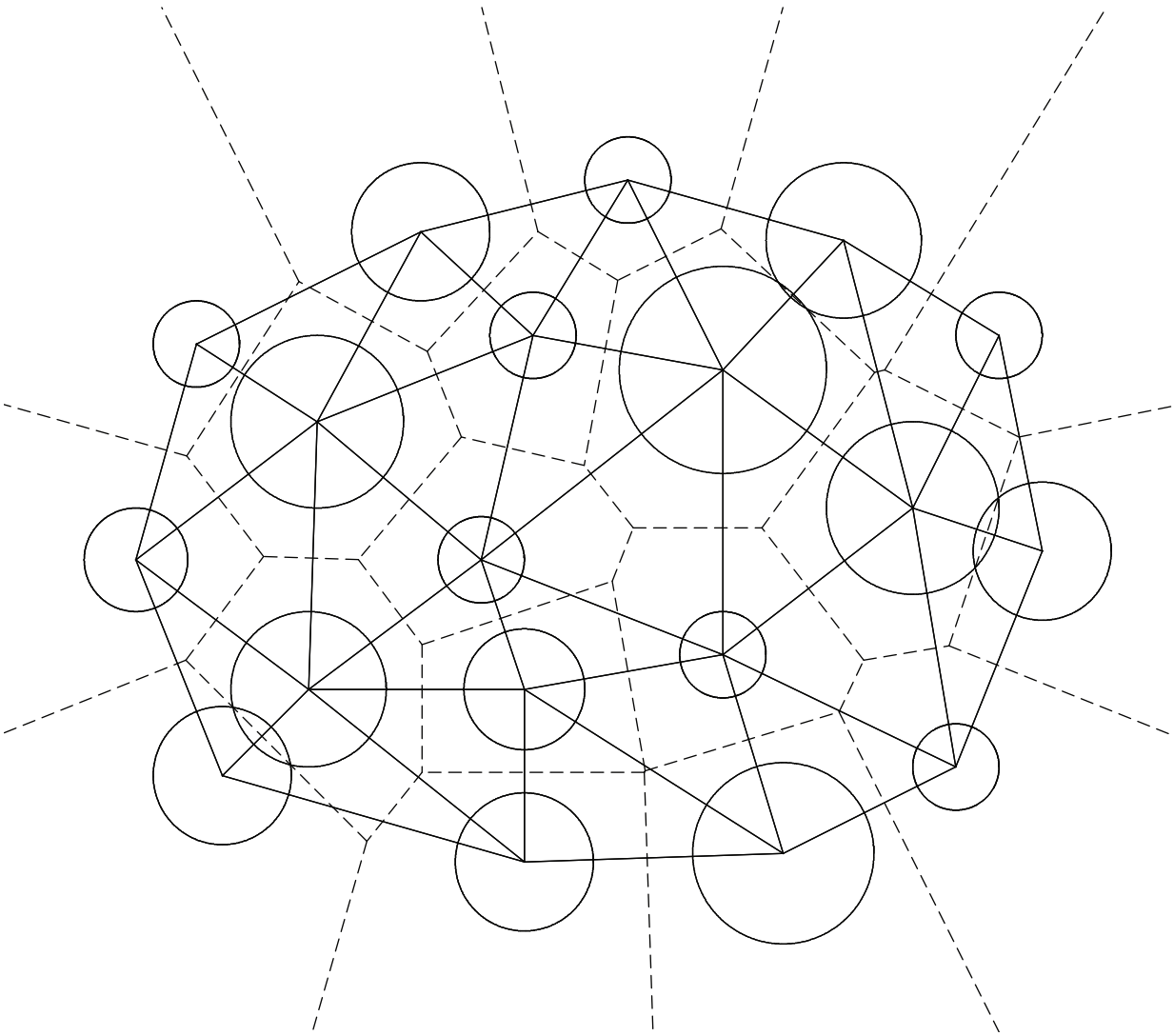

Figure 1.6: The weighted Delaunay triangulation (solid lines) and the power diagram (dashed lines) generated by a set of circles in the plane.

$x).(x_i - x)$ and $2(x_k - x).(x_j - x)$. Since those two quantities have opposite signs, we obtain $\pi_k(x) > 0$. As a consequence, $\pi_k(x)$ is strictly greater than both $\pi_i(x)$ and $\pi_j(x)$, and this for all $k \notin \{i, j\}$. This means that $x$ lies in the relative interior of a common facet of $C_i$ and $C_j$. According to the way the weighted Delaunay triangulation is deduced from the power diagram, $\mathrm{conv}(\{x_i, x_j\})$ then is a face of the weighted Delaunay triangulation generated by spheres $(S_i)_{1 \leq i \leq n}$. □

Assuming that the spheres $(S_i)_{1 \leq i \leq n}$ are spherical grains constituting a granular medium, they should physically satisfy the orthogonality condition and theorem 4 makes sure that all interparticle contacts will be found among the edges of the weighted Delaunay triangulation they generate. This property has already been used in the theses of D. Müller [Mül96a] and J.-A. Ferrez [Fer01] (see also [FL02]) in order to detect contacts between spherical grains in two and three dimensions respectively.

Theorem 4 can be generalized by appropriately relaxing the orthogonality condition.

Consider the following condition on spheres $(S_i)_{1\leq i\leq n}$, called *overlapping condition* :

$$\forall (i,j) \in \{1,...,n\}^2, i \neq j \Rightarrow \|x_j - x_i\|^2 > |R_j^2 - R_i^2|. \tag{1.5}$$

Observe that if spheres $(S_i)_{1\leq i\leq n}$ satisfy this overlapping condition, all the $x_i$ are vertices of the weighted Delaunay triangulation they generate. Assume spheres $(S_i)_{1\leq i\leq n}$ satisfy the overlapping condition, and let $I$ be a subset of $\{1,...,n\}$. We say that spheres $(S_i)_{i\in I}$ are *congruous* if they satisfy the following statement :

$$\forall (i,j) \in I \times \bar{I}, \|x_j - x_i\|^2 > R_i^2 + R_j^2, \tag{1.6}$$

where $\bar{I} = \{1,...,n\} \setminus I$. The weighted Delaunay triangulation generated by $(S_i)_{1\leq i\leq n}$ can be used to detect whether two congruous sets of spheres overlap, according to the following theorem :

**Theorem 5.** *Let $(S_i)_{1\leq i\leq n}$ be a set of spheres in general position that satisfy the overlapping condition (1.5) and let $(S_i)_{i\in I}$ and $(S_i)_{i\in J}$ be two distinct congruous subsets of $(S_i)_{1\leq i\leq n}$. If $\cup_{i\in I} conv(S_i)$ and $\cup_{j\in J} conv(S_j)$ intersect, there exist $i \in I$ and $j \in J$ so that $conv(\{x_i, x_j\})$ is a face of the weighted Delaunay triangulation generated by $(S_i)_{1\leq i\leq n}$.*

*Proof.* Among those pairs $(i,j) \in I \times J$ for which $\text{conv}(S_i)$ and $\text{conv}(S_j)$ intersect, take one that minimizes $\|x_j - x_i\|^2 - R_i^2 - R_j^2$. Call $x$ the point in $\text{conv}(\{x_i, x_j\})$ so that $\pi_i(x) = \pi_j(x)$. Let $k \in \{1,...,n\} \setminus \{i,j\}$.

If $k \notin I \cap J$, pairs $(S_i, S_k)$ and $(S_j, S_k)$ are less than orthogonal and using the same arguments as in the proof of theorem , we find that $\pi_k(x)$ is strictly greater than both $\pi_i(x)$ and $\pi_j(x)$.

Now assume that $k$ is in $I \cap J$. The situation is symmetric in $I$ and $J$ and we can therefore assume without loss of generality that $k \in J$. Using (1.1), we have :

$$\pi_k(x_i) - \pi_j(x_i) = \|x_k - x_i\|^2 - R_k^2 - R_i^2 - \|x_j - x_i\|^2 + R_j^2 + R_i^2. \tag{1.7}$$

From the way $(i,j)$ was chosen, $\|x_j - x_i\|^2 - R_i^2 - R_j^2$ is not greater than $\|x_k - x_i\|^2 - R_i^2 - R_k^2$ and equation (1.7) gives $\pi_k(x_i) \leq \pi_j(x_i)$, that is $x_j$ lies in the affine half-space $E$ defined by $\pi_k - \pi_j \geq 0$..

Now observe that the overlapping condition (1.5) implies $\pi_k(x_j) > \pi_j(x_j)$. Point $x_k$ therefore lies in the interior of $E$ and by convexity of $E$, so does the relative interior of the line segment $\text{conv}(\{x_j, x_k\})$. In particular, $x$ lies in the interior of $E$ which reads $\pi_k(x) > \pi_j(x)$.

We have shown that for all $k \in \{1,...,n\} \setminus \{i,j\}$, $\pi_k(x)$ is strictly greater than both $\pi_i(x)$ and $\pi_j(x)$. Point $x$ therefore lies in the relative interior of a common facet of $C_i$ and $C_j$. According to the way the weighted Delaunay triangulation is deduced from the power diagram, $\text{conv}(\{x_i, x_j\})$ is a face of the weighted Delaunay triangulation generated by spheres $(S_i)_{1\leq i\leq n}$. □

Theorem 5 will be used in chapter 3 for the detection of contacts between non-spherical grains. We will now give a local characterization of weighted Delaunay triangulations as well as a property that will turn out to be crucial for the regularization algorithm of section 3.3.

Assume $(S_i)_{1\leq i\leq n}$ is an assembly of $n$ spheres in general position in $\mathbb{R}^d$ with centers $(x_i)_{1\leq i\leq n}$ and radii $(R_i)_{1\leq i\leq n}$ and let $T$ be a triangulation of the point configuration $\{x_i : 1 \leq i \leq n\}$. Let $f$ be an interior facet of $T$, and $(a,b)$ the pair of vertices of $T$ so that $\text{conv}(\{a\} \cup f)$ and $\text{conv}(\{b\} \cup f)$ are maximal faces of $T$. Let $x$ be the center of the circumsphere $S$ of $\text{conv}(\{b\} \cup f)$ and $R$ its radius. According to (1.1), the power of $a$ with respect to sphere $S$ reads $\|x-a\|^2 - R^2$. We say that $f$ is *legal* if $\|x-a\|^2 - R^2 > 0$ and *illegal* if $\|x-a\|^2 - R^2 < 0$. Since spheres $(S_i)_{1\leq i\leq n}$ are in general positions, the case $\|x-a\|^2 = R^2$ does not occur. We say that a facet $f$ is *flippable* if its vertex set together with $\{a,b\}$ is a flippable circuit. The following theorem is a classical result of computational geometry and its proof can be found in [BY95] or in [ES96]:

**Theorem 6.** *A triangulation of $\{x_i : 1 \leq i \leq n\}$ is the weighted Delaunay triangulation $D$ generated by spheres $(S_i)_{1\leq i\leq n}$ if and only if its vertex set contains that of $D$ and all its interior facets are legal.*

This theorem provides a way to check whether a triangulation is the weighted Delaunay triangulation generated by spheres $(S_i)_{1\leq i\leq n}$ by performing one local test for each of its interior facets. Intuition suggests that we can obtain the weighted Delaunay triangulation generated by spheres $(S_i)_{1\leq i\leq n}$ by successively flipping illegal flippable facets in a triangulation $T$. We can formulate the following theorem:

**Theorem 7.** *Any triangulation of $\{x_i : 1 \leq i \leq n\}$ can be flipped to a triangulation that admits no facet simultaneously illegal and flippable.*

*Proof.* We will only sketch the proof of theorem 7 here. Let $T$ be a triangulation of $\{x_i : 1 \leq i \leq n\}$. Observe that lifting the vertices of $T$ to $\mathbb{R}^{d+1}$ using the height function (1.2) allows to represent $T$ as a polyhedral surface $\Sigma$ in $\mathbb{R}^{d+1}$. Assume that $T$ admits illegal flippable facets. It turns out that the illegal facets of $T$ correspond to the non-convexities of $\Sigma$. Therefore if $f$ is an illegal flippable facet of $T$, flipping it will produce a triangulation $T'$ whose associated polyhedral surface $\Sigma'$ lies strictly below $\Sigma$ (which can also be formulated as : the volume below $\Sigma'$ is strictly smaller than the volume below $\Sigma$). By *strictly below*, we mean that $\Sigma'$ is below $\Sigma$, while it is not identical to $\Sigma$. This means that it is impossible to cycle by successively flipping illegal flippable facets. Since the number of triangulations of $\{x_i : 1 \leq i \leq n\}$ is finite, a triangulation that admits no facet simultaneously illegal and flippable will eventually be reached. □

Observe that the triangulation $T'$ eventually reached by successively flipping illegal flippable facets from a triangulation $T$ of $\{x_i : 1 \leq i \leq n\}$ may not be the weighted Delaunay triangulation $D$ generated by spheres $(S_i)_{1\leq i\leq n}$. It can be proven that when flipping illegal flippable facets, vertices of the weighted Delaunay triangulation generated by spheres $(S_i)_{1\leq i\leq n}$ will never appear or disappear. Therefore if the vertex set of $T$ does not contain that of $D$, triangulation $T'$ cannot be equal to $D$. If $\mathcal{V}_D \subset \mathcal{V}_T$ then $\mathcal{V}_D \subset \mathcal{V}_{T'}$ as well but $T'$ still may admit illegal facets. According to theorem 6, $T'$ will be equal to $D$ if and only if $\mathcal{V}_D \subset \mathcal{V}_T$ and $T'$ has no illegal facet.

# Chapter 2

# The Distinct Element Method

The distinct element method is widely used to simulate phenomena involving grains. It allows to simulate on a computer the time evolution of a set of particles submitted to forces such as interparticle contact forces and gravity. Suppose $P_1$, ..., $P_k$ are particles in a three dimensional space evolving between a time $t_0$ and a time $t_f$. What the distinct element method needs to proceed are the spacial configuration of $P_1$, ..., $P_k$ a time $t_0$ and a way to compute the forces acting on $P_1$, ..., $P_k$ at a time $t \in [t_0, t_f]$, from the only knowledge of their spacial configuration. Several methods can be used to integrate the motion of the particles. Here, we consider the simplest one: *Euler's integration scheme*. A time step $\Delta t = \frac{t_f - t_0}{N}$ is used to discretize $[t_0, t_f]$ in a number $N \in \mathbb{N}^*$ of time intervals $[t_0 + i\Delta t, t_0 + (i+1)\Delta t]$ for $i \in \{0, ..., N-1\}$. This method further assumes that all the forces the particles are submitted to are constant within each of those time intervals of duration $\Delta t$. Therefore, by integrating the motion equations, the spacial configuration of $P_1$, ..., $P_k$ at time $t_0 + (i+1)\Delta t$ is easily deducible from that at time $t_0 + i\Delta t$. The overall process can be summarized as follows :

1. From the configuration of $P_1$, ..., $P_k$ at time $t_0 + i\Delta t$, compute the forces acting on $P_1$, ..., $P_k$.
2. Assuming the forces acting on the particles are constant within $[t_0 + i\Delta t, t_0 + (i+1)\Delta t]$, solve the motion equation for each individual particle inside the time interval $[t_0 + i\Delta t, t_0 + (i+1)\Delta t]$ and find its position at time $t_0 + (i+1)\Delta t$.
3. set $i + 1 \to i$ and return to 1.

Though this general description gives an overall idea of the DEM framework, some of its key components need to be further described in order for any implementation to be possible. In particular, a way to compute the forces acting on the particles from the sole knowledge of their spacial configuration still has to be practically formulated. This requires to model contacts between particles together with contact forces, but also the very shapes of the particles. These few issues are discussed in the remaining of this chapter.

## 2.1 A model for particle shapes

Let $S$ be the pointwise union of a finite number of simplices of $\mathbb{R}^3$ and $r > 0$ a real number. The particle $\Pi(S,r)$ consists of the points $x \in \mathbb{R}^3$ whose euclidean distance to $S$ is not greater than $r$. This amounts to taking the Minkowski sum of the set $S$ with the ball of $\mathbb{R}^3$ of radius $r$ centered at point 0. The set $S$ is called *skeleton* of $\Pi(S,r)$ and the real number $r$ is called *radius* of $\Pi(S,r)$. If $S$ is a point, $\Pi(S,r)$ is the ball of $\mathbb{R}^3$ of radius $r$ centered at point $S$. If $S$ is a line segment, $\Pi(S,r)$ is called *spherosegment*, or more usually *spherocylinder*. If $S$ is a triangle, $\Pi(S,r)$ is called *spherotriangle* and if it is a tetrahedron, $\Pi(S,r)$ is called *spherotetrahedron*. Balls, spherosegments, spherotriangles and spherotetrahedra are what we call *spherosimplices* (figure 2.1). When $S$ is a polyhedron, $\Pi(S,r)$ is a *spheropolyhedron*. Let $s_1$, ..., $s_k$ be the simplices whose pointwise union is the set $S$. The particle $\Pi(S,r)$ is then exactly the union $\cup_{i=1}^{k}\Pi(s_i,r)$ of basic spherosimplices.

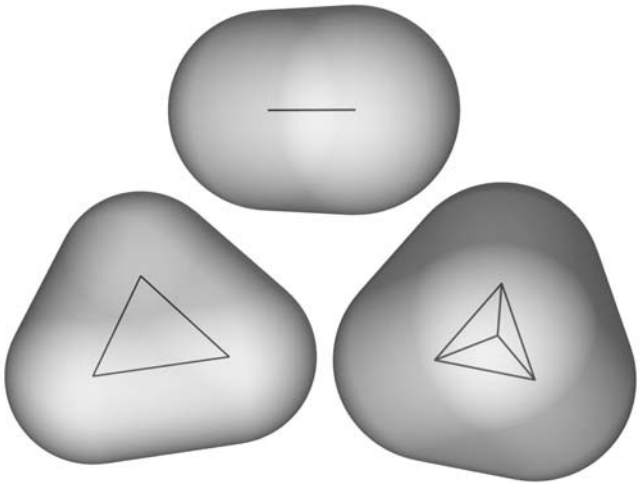

Figure 2.1: The Minkowski sums of a sphere with a line segment, a triangle and a tetrahedron. These particular shapes, called spherosimplices are some of the basic objects constituting the general particle model used in this work.

Actually, some skeletons may contain superfluous information as sketched in figure 2.2. Indeed, if $p$ is a point in $S$ whose distance to the boundary of $\Pi(S \setminus \{p\},r)$ is strictly greater than $r$, then $\Pi(S,r) = \Pi(S \setminus \{p\},r)$. Using particles so that the distance of any point $p \in S$ to the boundary of $\Pi(S \setminus \{p\},r)$ is $r$ will simplify their handling, avoiding useless calculations due to unnecessarily complex skeletons.

Observe that this geometrical description of the particle shapes assumes that they have a given position in space. Upon introduction of the time variable, the particles will be allowed to move accordingly to the rules underlying to the DEM framework. The particles will therefore be allowed to translate and rotate as a response to the physical constraints they will be subject to, but their shapes will remain unchanged. It follows that the skeleton $S$ of a particle will be a function $S(t)$ of time whose values will be deducible one from the other by a translation and a rotation. While $P$ will then be the function of time $P(t) = \Pi(S(t),r)$, $P$ and its incarnation $P(t)$ at different times $t$ will be used indifferently whenever $t$ does not need to be specified.

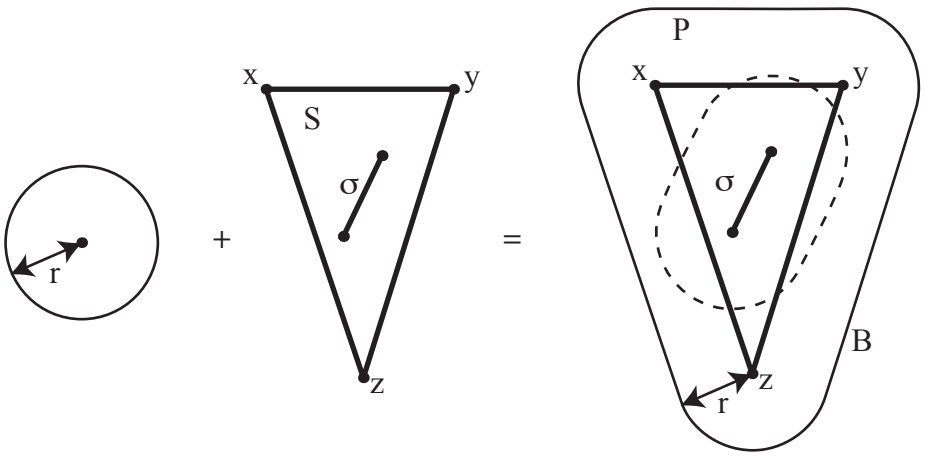


Figure 2.2: A two-dimensional particle $P = \Pi(S,r)$ obtained as the Minkowski sum of a set of simplices $S$ with a ball of radius $r$. The skeleton $S$ contains a line segment $\sigma$ whose Minkowski sum $\Pi(\sigma,r)$ with the same ball is sketched as a dashed line. The set $\Pi(\sigma,r)$ strictly lies in the interior of $P$ and therefore removing $\sigma$ from $S$ will not change $P$

### 2.1.1 Contacts and overlaps between particles

Two particles $P_1$ and $P_2$ are said to be in contact if they overlap, that is if $P_1 \cap P_2 \neq \emptyset$. This simple notion may seem shockingly unrealistic as two distinct solids will never simultaneously occupy the same portion of space. However, this model does have a physical interpretation and turns out to be very convenient for quantifying the geometrical properties of a contact when attempting to decide of a model for its physical behaviour.

Indeed, two particles experiencing a contact slightly deform at the contact point. Instead of using an explicit model for the deformation of the grain shapes, which would demand forbiddingly large computational efforts anyway, the shapes of the particles will remain unchanged and the deformation of the contact area will be modeled by the an overlapping between the particles, as sketched in figure 2.3.

The idea is that the relative position between the two undeformed particles in contact should be that they would have if they could deform. The amplitude of the overlap will then model the amount of deformation deformable particles would show in the same contact conditions. Observe that from the definition of a particle, two particles $P_1 = \Pi(S_1,r_1)$ and $P_2 = \Pi(S_2,r_2)$ overlap if and only if there exist two points $x_1 \in S_1$ and $x_2 \in S_2$ so that $\|x_1 - x_2\| < r_1 + r_2$. If two particles $P_1$ and $P_2$ are in contact and at least one of them is non-convex, the overlapping area $P_1 \cap P_2$ is not necessarily connected, that is $P_1$ and $P_2$ have several contacting areas as shown on figure 2.4.

This case shows that the above definition of a contact needs to be further refined. To this end, advantage can be taken of the way the particles have been defined and the following distance function can be introduced :

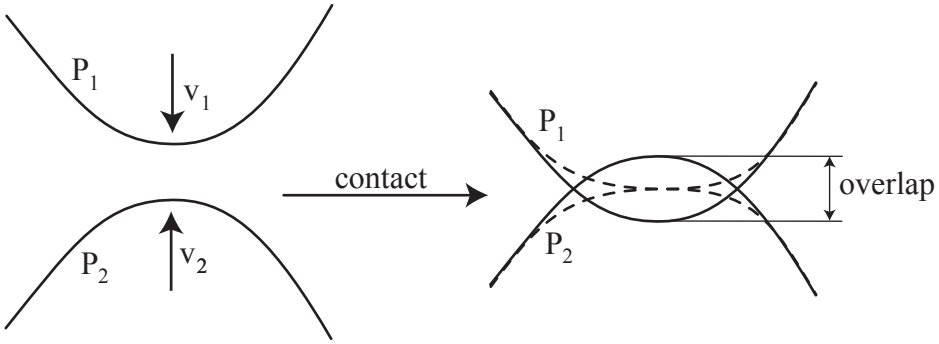


Figure 2.3: The deformation at the contact point is modeled by an overlapping of undeformed particles. The dashed line on the right-hand side sketches the deformation the contacting particles would experience if they were deformable

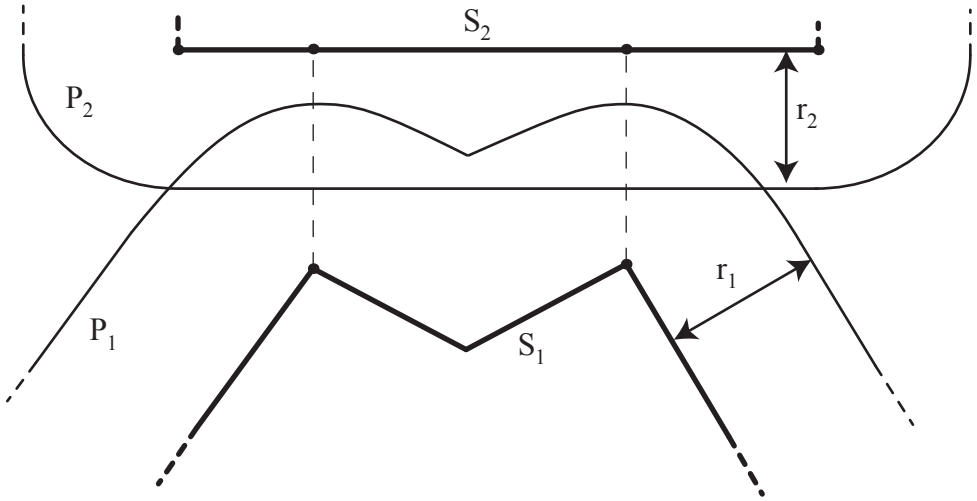


Figure 2.4: Two particles experiencing several simultaneous contacts because one of them is non-convex.

$$d : \begin{array}{ccc} S_1 \times S_2 & \rightarrow & \mathbb{R}^+ \\ (y_1, y_2) & \mapsto & \|y_2 - y_1\| \end{array} \tag{2.1}$$

Contacts between $P_1$ and $P_2$ will each be identified with a local minimum of function $d$. This function therefore separates the individual contact areas. Still not all among the local minima of function $d$ will correspond to a contact. As an example, figure 2.5 shows a local minimum of function $d$ where no overlapping occurs between $P_1$ and $P_2$. It follows that the local minima $(x_1, x_2)$ of function $d$ such that $r_1 + r_2 - \|x_2 - x_1\| < 0$ will not provide any contact point between $P_1$ and $P_2$.

Given a local minimum $(x_1, x_2)$ of function $d$, the distance between point $x_1$ and the boundary of $P_1$ along segment $\overline{x_1 x_2}$ reads :

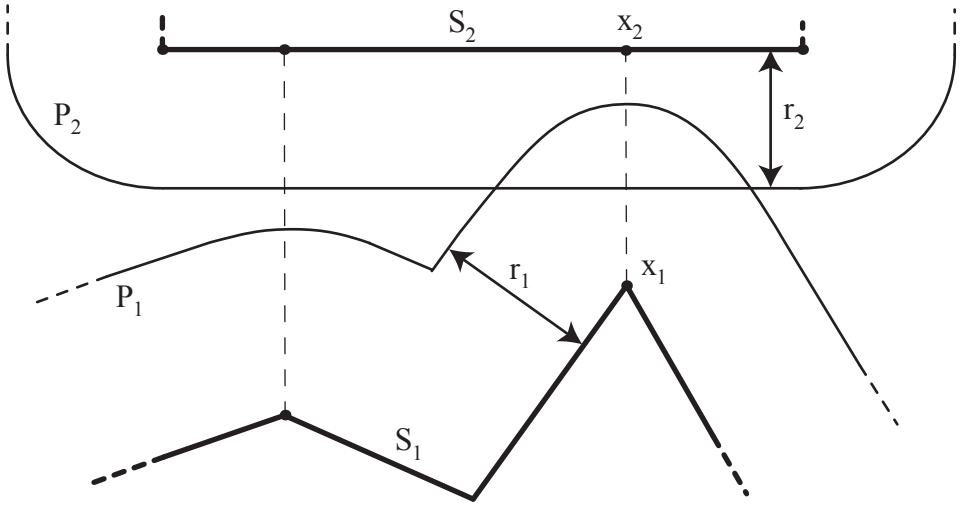


Figure 2.5: Some local minima of function $d$ may not correpond to overlapping areas

$$\delta(x_1, x_2) = d(x_1, \overline{x_1 x_2} \cap \complement_{\mathbb{R}^3} P) \tag{2.2}$$

The case may arise where a local minimum $(x_1, x_2)$ of $d$ satisfies $r_1 + r_2 - \|x_2 - x_1\| > 0$ but is so that either $\delta(x_1, x_2) > r_1$ or $\delta(x_2, x_1) > r_2$. Such a case is shown on figure 2.6. This kind of case provides an imaginary contact point. Moreover, there is always another local minimum $(y_1, y_2)$ of $d$ corresponding to the same contact area and simultaneously verifying the following three constraints called *contact conditions* :

$$\begin{array}{lcl} r_1 + r_2 - \|y_2 - y_1\| & > & 0 \\ \delta(y_1, y_2) & = & r_1 \\ \delta(y_2, y_1) & = & r_2 \end{array} \tag{2.3}$$

In order to avoid both imaginary contacts and non-overlapping areas, contacts will be identified with those local minima of function $d$ that satisfy the contact conditions (3.2). The contact detection method of chapter 3 will naturally sort out those situations.

Observe that if a contact occurs between two spherical particles, points $x_1$ and $x_2$ simply are the centers of those spheres. Using the couple $(x_1, x_2)$, we single out a point $x_c$, called contact point and to which we will suppose contact forces are applied, as will be explained in the following. The point $x_c$ is located on segment $\overline{x_1 x_2}$ at distance $d = \frac{d(x_1,x_2)}{2} - \frac{r_1^2 - r_2^2}{2d(x_1,x_2)}$ of $x_1$ (see figure 2.7). We call *contact plane* $\mathcal{C}$ the plane containing point $x_c$ which is orthogonal to segment $\overline{x_1 x_2}$.

Aside from the location of the contacts, points $x_1$ and $x_2$ also provide a model for the geometry of those contacts. By geometry, we mean the orientation of the contact (given by the vector $n$ normal to the contact area) and the amplitude of the overlap between the two particles at the contact point along the normal to the contact area, or *normal overlap*. The vector $n$ is simply defined as $n = \frac{x_2 - x_1}{d(x_1,x_2)}$ and the normal overlap $\xi_n(x_c)$

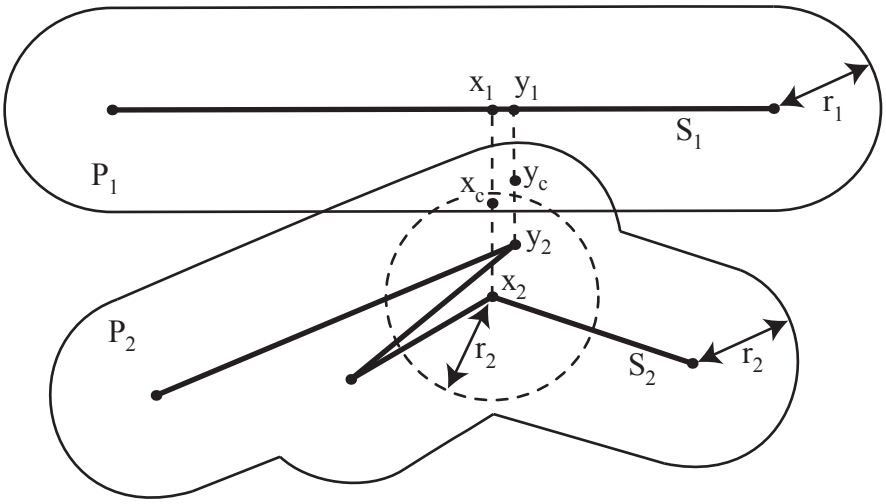


Figure 2.6: A contact between particles $P_1 = \Pi(S_1, r_1)$ and $P_2 = \Pi(S_2, r_2)$. The local minima of $d$ are $(x_1, x_2)$ and $(y_1, y_2)$ and they both satisfy the first contact condition as $r_1 + r_2 - \|x_2 - x_1\| > 0$ and $r_1 + r_2 - \|y_2 - y_1\| > 0$. However, $P_1$ and $P_2$ only admit one contact point given by the local minimum $(y_1, y_2)$. In order to avoid processing local minima such as $(x_1, x_2)$ which provide imaginary contact points, one should only consider such local minima $(z_1, z_2)$ of $d$ so that $\delta(z_1, z_2) = r_1$ and $\delta(z_1, z_2) = r_2$

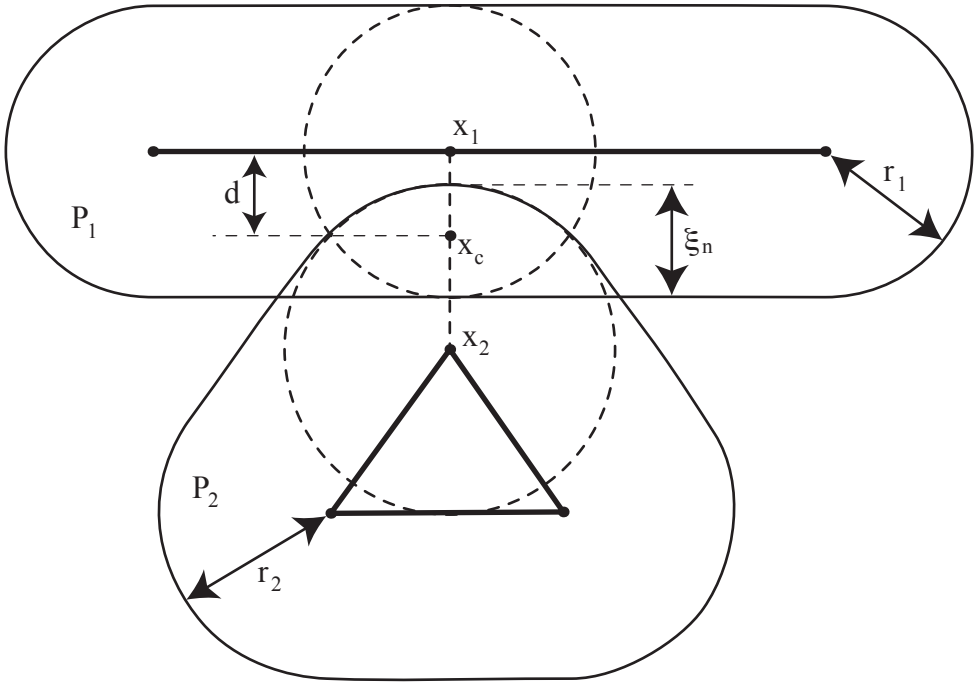


Figure 2.7: Geometrical modeling of a contact point

at the contact point reads $\xi_n(x_c) = r_1 + r_2 - d(x_1, x_2)$. The quantities $x_c$, $n$ and $\xi_n(x_c)$ can be easily computed anytime a local minimum $(x_1, x_2)$ of function $d$ is found that satisfies the contact conditions and will be useful in the following to model the contact forces. Observe that the geometry of a contact has been reduced here to its normal

components. Though a tangential overlap will be defined in the following section, it will not depend on the geometrical shape of the contact area. Therefore, whether the projection of the contact area on the plane tangential to the contact is isotropic or strongly anisotropic will make no difference on the behaviour of the contact except for its implicit correlation with $x_c$, $n$ and $\xi_n(x_c)$ (see figure 2.8). This clear choice keeps the model simple, while leaving room for improvements.

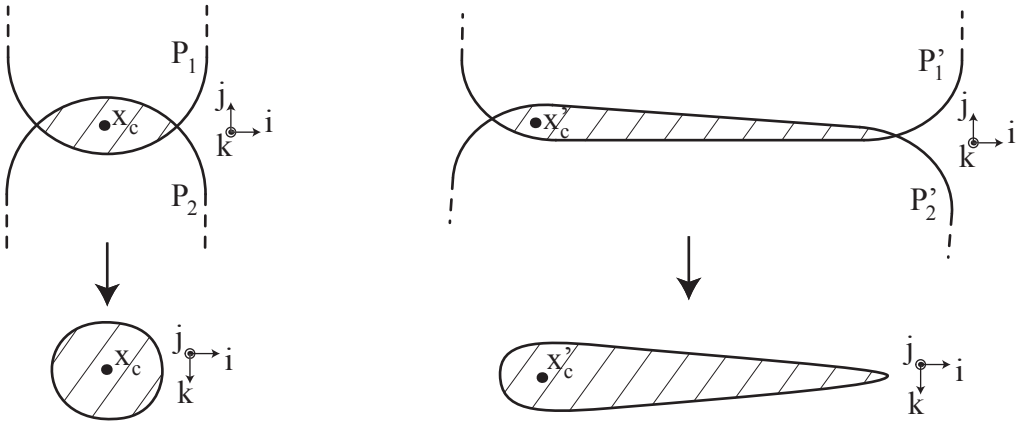


Figure 2.8: Isotropic (left) and anisotropic (right) contact areas in three-dimensional situations. A side view of the two contacting particles is sketched (top) as well as a view from above of the contact area (bottom). The contact force will be applied to points $x_c$ and $x_c'$ respectively.

## 2.2 Contact force modeling

When a contact is detected between two particles $P_1(S_1,r_1)$ and $P_2(S_2,r_2)$, a contact model is needed which exhibits the following two properties :

i) A contact has to be repulsive. The kinetic energy brought to the contact should be totally or partly stored and a part of it should be used to limit the penetration of the grains and eventually to be released as kinetic energy in order for the grains to separate.

ii) A contact has to be dissipative. The kinetic energy brought to the contact should be partly lost.

With such a physical contact model, we may obtain modeled granular media approximating real ones. In order to formulate such a model, we introduce repulsive forces $f_{P_2\to P_1}$ and $f_{P_1\to P_2}$ acting respectively on $P_1$ and $P_2$ at the contact point $x_c$ introduced in section 2.1.1 and depending on the geometrical and dynamical conditions the contact area is submitted to. The third Newton law allows us to simplify things a little bit as it reads $f = f_{P_1\to P_2} = -f_{P_2\to P_1}$. Still the dependence of the contact force $f$ on

the geometrical and dynamical conditions the contact area is submitted to has to be defined. The geometry of the contact area will be modeled by the overlap $\xi_n$ and the unitary vector $n$ normal to the contact surface already introduced in section 2.1.1 (see also figure 2.7), while the relative velocity $v_r(x_c)$ of $P_1$ and $P_2$ at point $x_c$ will model its dynamics. Calling $\omega_1$ and $\omega_2$ the spin vectors of $P_1$ and $P_2$, $v_r(x_c)$ reads :

$$v_r(x_c) = \dot{x}_2 - \dot{x}_1 + n \wedge (r_1\omega_1 + r_2\omega_2) \tag{2.4}$$

One can easily check that the primitive of $v_r(x_c).n$ which is zero when the contact begins is exactly $\xi_n$. Actually $v_r(x_c)$ can also be used to define a tangential overlap. Consider the following differential equation :

$$\dot{\xi} = (n \wedge \dot{n}) \wedge \xi - v_r(x_c) \tag{2.5}$$

We define the vector overlap $\xi$ as the solution of equation (2.5) which is zero when the contact begins. The normal and tangential overlaps are then given by :

$$\begin{array}{rcl} \xi_n & = & \xi.n \\ \xi_s & = & \xi - (\xi.n)n \end{array} \tag{2.6}$$

Practically, $\xi_n$ is given by $\xi_n = r_1 + r_2 - \|x_2 - x_1\|$ and under the assumption that the contact plane does not move much, $\xi_s$ is given by the following simpler equation :

$$\xi_s = \int_{t_0}^{t} v_r(x_c)du, \tag{2.7}$$

where $t_0$ is the instant the contact begins. The tangential deformation $\xi_s$ gives the distance between the current position of the contact point and the contact point at instant $t_0$ in a referential attached to the contact plane and accounts for the amount of tangential deformation at the contact point in the case of a pure sticky contact. However, a contact may also slip, in which case the tangential deformation either remains constant or decreases. A slipping behaviour will be made possible by using Coulombian friction to limit the magnitude of $\xi_s$.

In the molecular dynamics procedure, the contact forces are computed as functions of the overlaps $\xi_n$ and $\xi_s$ and their time derivatives $\dot{\xi}_n$ and $\dot{\xi}_s$ :

$$f = \phi_n(\xi_n, \dot{\xi}_n)n + \phi_s(\xi_s, \dot{\xi}_s) \tag{2.8}$$

where $\phi_s$ is a vector quantity parallel to the contact plane $\mathcal{C}$. Assuming that the tangential force $\phi_s(\xi_s, \dot{\xi}_s)$ does not already take into account the Coulomb friction, one has to replace it in (2.8) by :

$$\phi_s^C(\xi_s, \dot{\xi}_s) = \min(\mu\phi_n(\xi_n, \dot{\xi}_n), \| \phi_s(\xi_s, \dot{\xi}_s) \|)u_s \tag{2.9}$$

Where $\mu$ is the friction coefficient, and

$$u_s = \begin{cases} \frac{\phi_s(\xi_s, \dot{\xi}_s)}{\|\phi_s(\xi_s, \dot{\xi}_s)\|} & \text{if} \quad \phi_s(\xi_s, \dot{\xi}_s) \neq 0 \\ 0 & \text{if} \quad \phi_s(\xi_s, \dot{\xi}_s) = 0 \end{cases} \tag{2.10}$$

Observe that Coulomb law (2.9) should be implemented by bounding $\xi_s$ when needed. Here are two examples of force models, which are the most frequently used ones for practical simulations. We describe those models without the Coulomb friction, which has to be added afterwards according to (2.9).

- **Viscoelastic force** : this force, proposed by Cundall and Strack [CS79] is a linear combination of elastic and viscous terms. Energy is dissipated at the contact point by the viscous term. We give the linear expression of this force, but non-linear versions have been proposed and investigated (see [KK87])

$$\phi_n(\xi_n, \dot{\xi}_n) = k_n \xi_n + c_n \dot{\xi}_n \tag{2.11}$$

$$\phi_t(\xi_t, \dot{\xi}_t) = k_t \xi_t + c_t \dot{\xi}_t \tag{2.12}$$

- **Walton force** : this force, which models the elastoplastic behaviour of the grains at the contact point was proposed by Walton and Braun [WB86]. The energy is dissipated at a contact as plastic deformation. The loading is assumed elastoplastic and the unloading elastic. In either loading and unloading phases, the force is taken as a linear function of the overlap. As the force only depends on the overlap, the loading-unloading paths obtained with the Walton force model can be drawn on a force-overlap diagram, as sketched on figure 2.9, left. In order to take into account the elastoplastic loading, the loading slope $k^{(1)}$ has to be lower than the purely elastic unloading slope $k^{(2a)}$. If a reloading takes place, the force follows a purely elastic slope until it reaches the first loading path (this corresponds to part $(3)$ on the left diagram of figure 2.9). It would have been more realistic to model the loading phase as a first purely elastic part followed by a plastic part, and to take into account the $3/2$ exponent given by the Hertz theory for the elastic part, but this simple model contains the overall behaviour of elastoplastic materials and is therefore sufficient for a first approximation. The normal force reads

$$\phi_n(\xi_n, \dot{\xi}_n) = \begin{cases} \min(k_n^{(2a)}(\xi_n - \xi_n^m) + \phi_n^m, k_n^{(1)}\xi_n) & (\text{for } \dot{\xi}_n > 0) \\ \max(k_n^{(2a)}(\xi_n - \xi_n^M) + \phi_n^M, 0) & (\text{for } \dot{\xi}_n < 0) \end{cases} \tag{2.13}$$

where $\xi_n^M$ and $\phi_n^M$ (resp. $\xi_n^m$ and $\phi_n^m$) are the values of $\xi$ and $\phi$ at the beginning of the current unloading (resp. loading) phase (see figure 2.9, left diagram). A simple expression for the tangential Walton force roughly takes on the same features as the normal Walton force :

$$\phi_s(\xi_s, \dot{\xi}_s) = \begin{cases} \min(k_t^{(2a)}(\xi_s - \xi_s^m) + \phi_s^m, k_s^{(1)}\xi_s)u_s & (\text{for } \dot{\xi}_s > 0) \\ \max(k_t^{(2a)}(\xi_s - \xi_s^M) + \phi_s^M, 0)u_s & (\text{for } \dot{\xi}_s < 0) \end{cases} \tag{2.14}$$

Where $u_s$ is the unit vector defined when $\xi_s \neq 0$ by $u_s = \xi_s/\xi_s$. Both $\phi_n$ and $\| \phi_s \|$ may be drawn as functions of the overlaps (respectively $\xi_n$ or $\xi_s$) on a force-overlap diagram as the left one of figure 2.9.

## 2.3 Tuning molecular dynamics models with real experiments

The molecular dynamics models described in section 2.2 are technically operational, but the parameters of the force models ($k_n$, $k_s$, $c_n$, $c_s$ or the viscoelastic model and $k_n^{(1)}$,

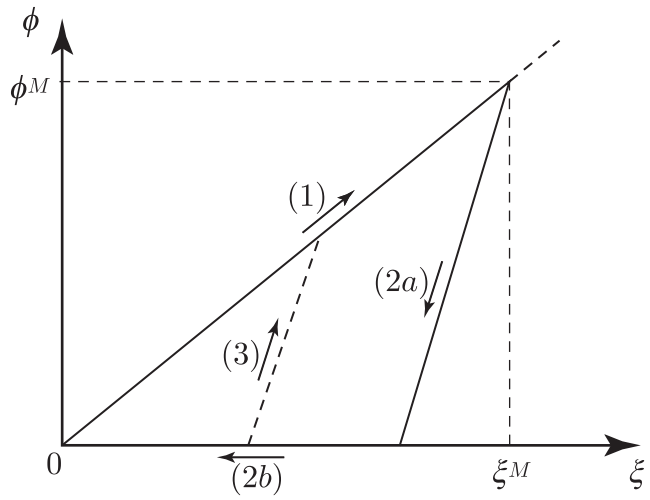


Figure 2.9: Behaviour of force-overlap path for Walton force model. The diagram can be used either for a normal or a tangential force. The path divide in (1) : loading, (2a, 2b) : unloading, (3) : reloading

$k_s^{(1)}$, $k_n^{(2a)}$, $k_s^{(2a)}$ for the Walton model) do not have a true physical reality, which means they have no *a priori* expressions for which the modeled behaviour will be realistic. Those parameters then have to be set empirically, so that the model quantitatively reproduces some real and well-known experiment. Experiments which involve more than one contact at a time usually do not provide measures which allow any analytic linking between the experiment and the model parameters, the number of cases to investigate for the resolution would be too high, and numerical implementation would be very heavy. We are left with single contact experiments to set our parameters, with no guarantee that situations which involve several simultaneous contacts will then be realistically modeled.

The experiment we will work with is the collision of two grains $P_1$ and $P_2$ having no initial spin. Three key quantities can be measured : the duration of the contact $t_c$ and the normal and tangential restitution coefficients $e_n$ and $e_s$, defined as follows using the notations of section 2.2 :

$$\begin{cases} e_n &= -\frac{\dot{\xi}_n^f}{\dot{\xi}_n^i} \\ e_s &= -\frac{\dot{\xi}_s^f}{\dot{\xi}_s^i} \end{cases} \tag{2.15}$$

Where $i$ and $f$ as exponents refer to quantities immediately before and immediately after the collision. Note that $e_s$ depends on the impact angle when the contact is slippery but is constant for a sticky contact. In this section, we assume the contact is and remains sticky. The tangential restitution coefficient then has a fixed value. This also allows us to use directly equation (2.8), without Coulomb friction for the analytic resolutions. The slippery behaviour of the contact, together with the subsequent alteration of $e_s$ will be provided afterwards trough equation (2.9). We will find here the analytic expressions for $t_c$, $e_n$ and $e_s$ for the modelled contact as functions of the model parameters. By inverting those expressions we will be able to set the model parameters so that $e_n$, $e_s$ and $t_c$ are controlled for single contact situations. The motion equations for

the grains $P_1$ and $P_2$ read :

$$\begin{cases} m_1\ddot{x}_1 &= -f \\ m_2\ddot{x}_2 &= f \\ I_1\dot{\omega}_1 &= -R_1 n \wedge f \\ I_2\dot{\omega}_2 &= -R_2 n \wedge f \end{cases} \tag{2.16}$$

As the two grains experience the collision, plane $\mathcal{C}$ will not move much, which allows us to assume $n$ is a constant. (2.5) then simplifies to $\dot{\xi} = -v_c$ and equation (2.4) gives :

$$\ddot{\xi} = \ddot{x}_1 - \ddot{x}_2 - n \wedge (r_1\dot{\omega}_1 + r_2\dot{\omega}_2) \tag{2.17}$$

From (2.16) and (2.17) one finds :

$$\ddot{\xi} = -\frac{1}{m_{eff}} f - (\frac{r_1^2}{I_1} + \frac{r_2^2}{I_2})\phi_s(\xi_s, \dot{\xi}_s) \tag{2.18}$$

Where $1/m_{eff} = 1/m_1 + 1/m_2$ As the grains have no initial spin, the centers of the grains will move in a plane. Calling $u_\perp$ a unit vector normal to that plane, we define a unit vector tangential to the contact by $u_s = n \wedge u_\perp$. Equation (2.18) then projects on $u_n$ and $u_t$ as follows :

$$\begin{cases} \ddot{\xi}_n = -\frac{1}{m_{eff}}\phi_n(\xi_n, \dot{\xi}_n) \\ \ddot{\xi}_s = -(\frac{1}{m_{eff}} + \frac{r_1^2}{I_1} + \frac{r_2^2}{I_2})\phi_s(\xi_s, \dot{\xi}_s).u_s \end{cases} \tag{2.19}$$

Where $\xi_s = \xi_s.u_s$. Those differential equations can be solved for $\xi_n$ and $\xi_s$, provided expressions for $\phi_n$ and $\phi_s$ such as (2.11, 2.12) or (2.13, 2.14). For those two cases, we have the following solutions :

- **Viscoelastic force** : from (2.11), (2.12) and (2.19) we find the following set of differential equations :

$$\begin{cases} \ddot{\xi}_n + \frac{c_n}{m_{eff}}\dot{\xi}_n + \frac{k_n}{m_{eff}}\xi_n &= 0 \\ \ddot{\xi}_s + c_s(\frac{1}{m_{eff}} + \frac{R_1^2}{I_1} + \frac{R_2^2}{I_2})\dot{\xi}_s + k_s(\frac{1}{m_{eff}} + \frac{R_1^2}{I_1} + \frac{R_2^2}{I_2})\xi_s &= 0 \end{cases} \tag{2.20}$$

  Solving (2.20) provides expressions for $e_n$, $e_s$ and $t_c$ according to (2.15) as functions of $k_n$, $c_n$, $k_s$ and $c_s$. Inverting those expressions we find :

$$\begin{cases} k_n &= \frac{m_{eff}}{t_c^2}(\pi^2 + \ln(e_n)^2) \\ c_n &= -\frac{2m_{eff}}{t_c}\ln(e_n) \\ k_s &= \frac{1}{t_c^2(\frac{1}{m_{eff}} + \frac{R_1^2}{I_1} + \frac{R_2^2}{I_2})}(\pi^2 + \ln(e_s)^2) \\ c_s &= -\frac{1}{t_c(\frac{1}{m_{eff}} + \frac{R_1^2}{I_1} + \frac{R_2^2}{I_2})}\ln(e_s) \end{cases} \tag{2.21}$$

  The set of equations (2.21) allows to derive the contact parameters from the values of $e_n$, $e_s$ and $t_c$ for single sticky contacts situations with the viscoelastic force model.

- **Walton force** : from (2.13), (2.14) and (2.19) we find the following differential equations :

$$\begin{cases} \ddot{\xi}_n + \frac{k_n^{(1)}}{m_{eff}}\xi_n = 0 & (\text{for } \dot{\xi}_n > 0) \\ \ddot{\xi}_s + k_s^{(1)}(\frac{1}{m_{eff}} + \frac{R_1^2}{I_1} + \frac{R_2^2}{I_2})\xi_s = 0 & (\text{for } \dot{\xi}_s > 0) \\ \ddot{\xi}_n + \frac{k_n^{(2a)}}{m_{eff}}\xi_n = \frac{k_n^{(2a)} - k_n^{(1)}}{m_{eff}}\xi_n^M & (\text{for } \dot{\xi}_n < 0) \\ \ddot{\xi}_s + (\frac{1}{m_{eff}} + \frac{R_1^2}{I_1} + \frac{R_2^2}{I_2})k_s^{(2a)}\xi_s & \\ \quad = (\frac{1}{m_{eff}} + \frac{R_1^2}{I_1} + \frac{R_2^2}{I_2})(k_s^{(2a)} - k_s^{(1)})\xi_s^M & (\text{for } \dot{\xi}_s < 0) \end{cases} \tag{2.22}$$

Where the quantities $\xi_n^M$ and $\xi_s^M$ refer to the values of $\xi_n$ and $\xi_s$ at the end of the loading phases. Solving (2.22) for solutions with continuous derivatives gives expressions for $e_n$, $e_s$ and $t_c$ according to (2.15) as functions of $k_n$, $c_n$, $k_s$ and $c_s$. Inverting those expressions we find :

$$\begin{cases} k_n^{(1)} = m_{eff}(\frac{\pi(1+e_n)}{2t_c})^2 \\ k_n^{(2a)} = m_{eff}(\frac{\pi(1+e_n)}{2t_c e_n})^2 \\ k_s^{(1)} = \frac{1}{\frac{1}{m_{eff}} + \frac{R_1^2}{I_1} + \frac{R_2^2}{I_2}}(\frac{\pi(1+e_s)}{2t_c})^2 \\ k_s^{(2a)} = \frac{1}{\frac{1}{m_{eff}} + \frac{R_1^2}{I_1} + \frac{R_2^2}{I_2}}(\frac{\pi(1+e_s)}{2t_c e_s})^2 \end{cases} \tag{2.23}$$

Equations (2.23) allow to control the values of $e_n$, $e_s$ and $t_c$ for single sticky contacts situations with the Walton force model.

By expressing the coefficients of the force models as shown in this section, we know that any single sticking contact situation will be realistically modelled. However we have no guarantee that situations involving several simultaneous contacts will be realistic.

# Chapter 3

# A triangulation-based contact detection method

This chapter describes a method based on triangulations for detecting contacts between particles in the DEM framework. This method, first imagined and implemented in the two dimensional case by D. Müller [Mül96a] was extended for tridimensional spherical particles by J.-A. Ferrez [Fer01]. While D. Müller designed two versions of the code, one that could handle spheres and one that could handle polygonal particles, this last version could not be naturally extended to polyhedra due to theoretical limitations. Indeed, the twodimensional code for polygonal grains uses *constrained triangulations* whose conditions of existence in dimensions higher than two [She05] are too restrictive for the algorithm to work. Still an adaptation to the non-spherical particles introduced in chapter 2 of the tridimensional algorithm for spherical particles is possible, and this is the main subject of this chapter. The first section describes the original method for spheres and the second one its generalization to non-spherical particles. The third section is about the handling of the weighted Delaunay triangulations used in the contact detection method.

## 3.1 Spherical particles

We are given a finite number of spheres $(P_i)_{1\leq i\leq n}$. Naively testing all the pairs for contact requires $O(n^2)$ time. This becomes prohibitive as $n$ grows, typically in practice $10^3 < n < 10^5$. Others have proposed using spacial decompositions to overcome this difficulty [AT87]. Here we use the weighted Delaunay triangulation generated by the family spheres $(P_i)_{1\leq i\leq n}$ as already proposed in [Mül96a; Fer01; FL02]. A long series of computational experiments has shown that with this approach, one can reduce the computational effort of contact detection from $O(n^2)$ to $O(n)$ (see chapter 4).

Observe first that since spheres $(P_i)_{1\leq i\leq n}$ model physical particles, their mutual overlaps should be rather small. It is therefore justified to assume that orthogonality condition (1.3) is satisfied. In this case, theorem 4 makes sure that all interparticle contacts

among spheres $(P_i)_{1\leq i\leq n}$ are identified by exactly one edge of the weighted Delaunay triangulation $T$ generated by spheres $(P_i)_{1\leq i\leq n}$. Provided this triangulation is known, contact detection can therefore be restricted to those pairs of spheres whose centers are linked by one of its edges.

Two problems have to be solved in order to make sure this method is efficient. The building and handling the weighted Delaunay triangulation along with the particle's motion, will be adressed in section 3.3. The second problem is a nice combinatorial one. Indeed, there exist weighted Delaunay triangulations that admit a quadratic number of edges [BY95]. In order to know whether or not those quadratic cases arise in practical situations, numerical investigations have been conducted whose complexity results are reported in chapter 4.

## 3.2 Non-spherical particles

In this section, we assume that $(P_i)_{1\leq i\leq n}$ are particles that are not necessarily spherical, yet their shapes can be described using the model of chapter 2. In order to detect all contacts occuring among those particles, it is possible to generalize the approach described in the preceding section.

Each particle $P_i$ will be associated with a set of spheres $\mathcal{S}_i$. We impose $P_i$ to lie inside $\cup_{S\in\mathcal{S}_i}\text{conv}(S)$. This restriction will be called *covering condition*. The weighted Delaunay triangulation $T$ generated by the set of all covering spheres $\mathcal{S}=\cup_{i=1}^{n}\mathcal{S}_i$ will be used to detect interparticle contacts, provided that the set of covering spheres $\mathcal{S}$ satisfies the overlapping condition (1.5) and that the spheres $\mathcal{S}_i$ associated to a particle are congruous (that is, satisfy (1.6)). Indeed, if two particles $P_i$ and $P_j$ intercept, sets $\cup_{S\in\mathcal{S}_i}\text{conv}(S)$ and $\cup_{S\in\mathcal{S}_j}\text{conv}(S)$ are bound to intercept as well according to the covering condition. Since the overlapping condition is satisfied and since $\mathcal{S}_i$ and $\mathcal{S}_i$ are congruous sets of spheres, theorem 5 then ensures that there exist $S_i\in\mathcal{S}_i$ and $S_j\in\mathcal{S}_j$ whose centers are linked by an edge of $T$. By successively testing all the edges of $T$, particle pairs candidate for contact can thus be detected.

As for the spherical case, this method requires building and updating the weighted Delaunay triangulation. This will be adressed in section 3.3. Of course the problem of knowing whether or not the number of edges of $T$ is quadratic or not in practical cases remains and one can refer to chapter 4 for numerical complexity tests. Two further problems arise in this non-spherical case. For one, covering each particle with spheres that satisfy the conditions stated above is required, which will be adressed in section 3.2.1. The other problem specific to non-spherical particles is that of finding actual contact points once a pair of particles has been selected using the triangulation.

Recall from chapter 2 that a contact between particles $P=\Pi(S_P,r_P)$ and $Q=\Pi(S_Q,r_Q)$ will be identified by a pair $(x_P,x_Q)\in S_P\times S_Q$ chosen among the local minima of function (2.1). If $P$ and $Q$ are two contacting spheres $x_P$ and $x_Q$ will always be the centers of those spheres. If $P$ and $Q$ are non-spherical particles however, $x_P$ and $x_Q$ depend on the relative position of the particles. Moreover if either $P$ or $Q$ are non-convex, there

may be several contact points between them, corresponding to different local minima of function (2.1). Observe that $S_P$ and $S_Q$ are the pointwise union of basic simplices, that is $S_P = \cup_{s\in\mathcal{S}_P} s$ and $S_Q = \cup_{s\in\mathcal{S}_Q} s$. For the non-spherical cases, we propose to compute the distance between every pair $(s,s') \in \mathcal{S}_P \times \mathcal{S}_Q$. The arrangement of simplices in each skeleton will immediately provide the local minima of function (2.1). Observe that the number of local minima may be infinite (think of parallel spherotriangles). In this case, the values for $x_P$ and $x_Q$ should be chosen as the barycenters of the possible candidates for minimization in $S_P$ and $S_Q$ respectively. Only those local minima that satisfy the contact condition will identify actual contacts.

The method proposed above to find the local minima of (2.1) that consists in computing the distance between all the pairs of simplices constituting $S_P$ and $S_Q$ proves useful in simple cases, when the skeletons are simplices for example. If the skeletons are constituted by many simplices, though, this process may be unnecessarily time consuming and one can think of better procedures depending on the situation at hand. In the case of convex skeletons, there only is one contact possible between two particles. The global minimum of function (2.1) then is its only local minimum, if we except the degenerate case of parallel simplices. The problem then amounts to minimize a quadratic function under linear constraints which can be done in a variety of ways.

Moreover, theorem 5 only states that a contact will for sure be identified by at least one edge of $T$. Depending on the way each particle is covered by its associated spheres, $T$ may give information on the localization of contacts. However, if this can be achieved, this has to be properly described and stated as a theorem analogous to theorems 4 and 5.

### 3.2.1 Covering the particles with spheres

The method described in section 3.2 that detects contacts between non-spherical particles requires particles to be covered with spheres. Those spheres are required to satisfy the overlapping condition (1.5) and spheres associated to a particle have to be congruous (according to statement (1.6)). In order for contact detection to be possible through all the simulation process, the set of spheres should keep those properties with the motion of the particles.

Provided those conditions remain satisfied, one can imagine adding covering spheres, deleting others, moving their centers with respect to their associated particles or changing their radii. Using all those degrees of freedom may provide a placement of covering spheres that is optimal for contact detection purposes. Observe though that finding such optimal placements requires that extensive information about the relative positions of the particles be known a priori. While a part of that information may be easily available, making it possible to enhance the quality of contact detection at low cost by proceeding to such modifications, we will not address this subject here and will only consider the coverings so that:

- no sphere is added or deleted,

- the centers of the spheres are motionless with respect to their associated particles,
- the radii of the spheres do not change while the particles move.

Still, the positions and radii of the covering spheres need to be defined. Observe that in order for the spheres associated to a particle to stay congruous while the particles move, one has to guarantee that any pair of spheres associated to different particles be less than orthogonal regardless of their relative positions. In order to characterize this, we assume in the following that the overlaps experienced by contacting particles will never exceed a quantity $\xi_m \geq 0$ called *maximal overlap*. As the overlap reflects the amount of deformation a particle would experience at a contact point, any realistic simulation will lead to small values for $\xi_m$. However, far away from any physical consideration, an upper bound will be provided later for $\xi_m$ which is only due to the contact detection method.

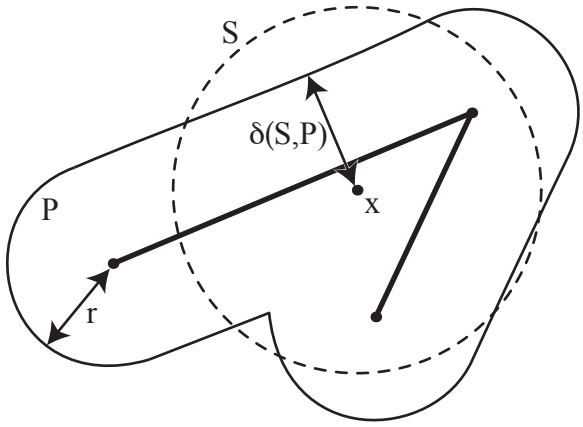


Figure 3.1: The distance $\delta(S,P)$ between the center $x$ of ball $S$ and the boundary its associated particle $P$ sketched in a particular case.

We also introduce the distance $\delta(S,P)$ sketched in figure 3.1 between the center $x$ of the covering sphere $S$ and the boundary of its associated particle $P$ as :

$$\delta(S,P) = d(x, \complement_{\mathbb{R}^3} P). \tag{3.1}$$

Using this notation, the distance between the centers of two spheres $S_P$ and $S_Q$ associated to different particles $P$ and $Q$ will always be greater or equal to $\delta(S_P,P) + \delta(S_Q,Q) - \xi_m$. Call $(R_P^1, d_P^1)$, ..., $(R_P^{k_P}, d_P^{k_P})$ the different values that a sphere $S_P$ associated to a particle $P$ may admit for the pair $(R_{S_P}, \delta(S_P,P))$ and consider the following system of inequations :

$$\begin{cases} (d_P^i + d_Q^j - \xi_m)^2 & \geq & {R_P^i}^2 + {R_Q^j}^2, & \forall P \neq Q, \forall (i,j) \in \{1,...,k_P\} \times \{1,...,k_Q\}, \\ R_P^i & \geq & d_P^i, & \forall P, \forall i \in \{1,...,k_P\}. \end{cases} \tag{3.2}$$

Following above remarks, admissible solutions of the system (3.2) of inequations provide values for the radii of the covering spheres and distances to the boundary of their associated particles that make sure that spheres associated to a particle are congruous independently of the relative positions of the particles. Moreover, this system requires the radii of covering spheres to be greater than the distance to the boundary of their associated particle, making it possible to actually cover the particles. While this system is not linear, fixing the values of the $d_P^i$, $i \in \{1,...,k_P\}$ for all particles $P$ will make it so. Choosing in addition $k_P = 1$ for all particles $P$ will provide the following simpler linear system, where the exponents have been dropped for obvious reasons :

$$\begin{cases} R_P^2 + R_Q^2 & \leq & (d_P + d_Q - \xi_m)^2, & \forall P \neq Q, \\ R_P^2 & \geq & d_P^2 & \forall P. \end{cases} \tag{3.3}$$

Calling $n$ the number of particles, this last system is left with $\frac{n(n-1)}{2} + n$ inequations. Once an admissible solution for either system (3.2) or system (3.3) has been found, it remains to cover the particles with spheres dimensioned accordingly, keeping in mind that the overlapping condition (1.5) has to be fulfilled. This constitutes an interesting optimization problem. It is not necessary to find a set of covering spheres which is minimal. It is sufficient that all particles be covered by their associated spheres while the overlapping condition is satisfied. However, in order for the complexity of the contact detection procedure to remain reasonable, it is of course better to keep the sets of covering spheres as small as possible.

There can be many ways to cover particles with spheres of given sizes. In the following, we propose some simple coverings in particular cases with given particle shapes.

#### 3.2.1.1 Spherocylinders

We assume that all particles to be simulated are spherocylinders with equal radii $r$. Observe that we do not impose any condition on the length of the particles. We further assume that all covering spheres will have same radii $R$ and that for all particles, $d_P = r$. Observe that, due to this last assumption, the overlapping condition (1.5) is automatically satisfied. In this framework, system (3.3) reduces to the pair of inequations $r \leq R \leq \sqrt{2}r - \xi_m/\sqrt{2}$. This means that covering all spherocylinders with spheres of radii $R = \sqrt{2}r - \xi_m/\sqrt{2}$ centered on their skeletons will provide a set of covering spheres with the required properties, i.e. satisfying the overlapping condition and so that spheres associated to a particle stay congruous independently of the relative positions of the particles.

Now consider one such spherocylinder $P$ of radius $r$ and call $\sigma$ the single line segment composing its skeleton. We denote $\lambda$ the length of $\sigma$. In order to cover it with spheres of radii $R$ centered on $\sigma$, one can place $\lceil (\lambda - 2(R-r))/(2\sqrt{R^2 - r^2}) \rceil + 1$ spheres. This result is optimal, which can easily be proven. Indeed, if fewer spheres are used, then there exists two spheres $S_i$ and $S_{i+1}$ consecutive along $\sigma$ whose centers $x_i$ and $x_{i+1}$ have a distance greater than $2\sqrt{R^2 - r^2}$. In this case the circle of radius $r$ centered on

| dimension of the skeleton | $d$ |
|---|---|
| 0 | $r_0$ |
| 1 | $r_1$ |
| 2 | $r_2$ |
| 3 | $r_3 + \frac{l_3}{3}$ |

Table 3.1: Values of $d$ for a sphere, a spherocylinder, a spherotriangle and a spherotetrahedron.

$\sigma$ that lies in the mediating plane of $\text{conv}(\{x_i, x_{i+1}\})$ happen to lie in $P$ while being outside of all covering spheres, which contradicts the covering condition.

#### 3.2.1.2 Spherosimplices with only one covering sphere

In this section, we adress the inverse problem of dimensioning the particles, in order for one only covering sphere to be needed for each of them. We restrict to symetrical particles. While spheres and spherocylinders always are symetrical, spherotriangles and sherotetrahedra will be symetrical if their skeletons are regular triangles and tetrahedra respectively. For such a symetrical spherosimplex, we call $r$ its radius, $x$ its mass center, $l$ the distance between $x$ and any vertex of its skeleton and $d$ the distance between $x$ and its boundary. We further impose spherosimplices of a same kind to be identical, which will allow to index all those dimensions when needed by the affine dimension of the spherosimplex's skeleton (0 for a sphere, 1 for a spherocylinder, 2 for a spherotriangle and 3 for a spherotetrahedron). We center a unique covering sphere at point $x$, and in order for the covering condition to be optimally satisfied, the radius of this covering sphere will be $l + r$. Observe that the triple $(r, l, d)$ is redundant since $d$ is a function of $l$ and $r$. The values of $d$ for each kind of spherosimplex are shown in table 3.2.1.2.

What we need to find are the values of $l$ and $r$. Observe first that if all particles are identical spheres, there is no bound on $r_0$. Now if all particles are identical spherocylinders, system (3.2) reduces to $l_1 \leq (\sqrt{2} - 1)r_1 - \frac{\xi_m}{\sqrt{2}}$ since the radius of the covering sphere $(l + r)$ is greater by definition to the radius of the spherocylinder. Bounding $\xi_m$ by $r_1/8$, one then obtains that with any ratio $l_1/r_1$ lower than $(\frac{15}{8\sqrt{2}} - 1) \approx 0.325$ the conditions our contact detection method requires are satisfied.

If all particles are identical spherotriangles, one can see that the same constraints apply to $(r_2, l_2)$ than to $(r_1, l_1)$ in the case of spherocylinders and we conclude as well that with any ratio $l_2/r_2$ lower than $(\frac{15}{8\sqrt{2}} - 1) \approx 0.325$ the contact detection method will work in this case of one covering sphere per particle (provided $\xi_m$ does not exceed $r_2/8$).

Now if all particles are identical spherotetrahedra, system (3.2) reduces to $l_3 \leq 3\frac{\sqrt{2}-1}{3-\sqrt{2}} r_3 - \frac{3\xi_m}{3\sqrt{2}-2}$. Bounding $\xi_m$ by $r_3/8$, we find that for any value of $l_3/r_3$ lower than $\frac{45-24\sqrt{2}}{24\sqrt{2}-16} \approx 0.616$, our contact detection method will work with one covering sphere per particle.

Let us address a simple bidisperse case. By bidisperse we mean that two kinds of spherosimplices are present in the system, the particles within each species being geometrically identical. If those two kinds of spherosimplices are spheres and spherocylinders, system (3.2) reads:

$$\left\{\begin{array}{lcl}(r_0+r_1-\xi_m)^2 & \geq & r_0^2+(r_1+l_1)^2,\\ r_0 & \geq & \frac{\xi_m}{2-\sqrt{2}},\\ r_1 & \geq & \frac{l_1}{\sqrt{2}-1}+\frac{\xi_m}{2-\sqrt{2}},\end{array}\right. \tag{3.4}$$

Observe that the second inequation of system (3.4) will be satisfied as soon as $r_0$ is greater than $\frac{\xi_m}{2-\sqrt{2}}$, which is not really constraining since $\xi_m$ should be small compared to the radii of the particles. The last inequation of system (3.4) provides the same upper bound for $l_1$ as that found above in the monodisperse case. Replacing $l_1$ by this bound in the first inequation of system (3.4) gives an inequality that is more constraining and admissible solutions of the following system therefore are admissible for system (3.4):

$$\left\{\begin{array}{lcl}r_1^2-r_0r_1+\frac{\xi_m^2}{4}+r_0\xi_m & \leq & 0,\\ r_0 & \geq & \frac{\xi_m}{2-\sqrt{2}},\\ r_1 & \geq & \frac{l_1}{\sqrt{2}-1}+\frac{\xi_m}{2-\sqrt{2}},\end{array}\right. \tag{3.5}$$

Observe that in order for the first inequation of system (3.5) to have a solution in $r_1$, one should impose $r_0^2-4\xi_m r_0-\xi_m^2\geq 0$, that is $r_0\geq(2+\sqrt{5})\xi_m$. We replace the second inequality of system (3.5) by this more constraining inequation. Solving the first inequation of system (3.5) for $r_1$ gives $0.5(r_0-\sqrt{r_0^2-4r_0\xi_m-\xi_m^2})\leq r_1\leq 0.5(r_0+\sqrt{r_0^2-4r_0\xi_m-\xi_m^2})$, which provides the following even more constraining system:

$$\left\{\begin{array}{lcl}r_1 & \geq & 0.5(r_0-\sqrt{r_0^2-4r_0\xi_m-\xi_m^2}),\\ r_1 & \leq & 0.5(r_0+\sqrt{r_0^2-4r_0\xi_m-\xi_m^2}),\\ r_0 & \geq & (2+\sqrt{5})\xi_m,\\ r_1 & \geq & \frac{l_1}{\sqrt{2}-1}+\frac{\xi_m}{2-\sqrt{2}},\end{array}\right. \tag{3.6}$$

Assuming that $r_0$ is given and satisfies the third inequation of system (3.6), one can find values for $r_1$ (given by the first two inequations of system (3.6)) and $l_1$ (last inequation of system (3.6)) so that our contact detection method applies. Assuming that $\xi_m\leq r_0/8$, we deduce from system (3.6) that any choice within the following bounds will be admissible for our contact detection method :

$$\left\{\begin{array}{lcl}l_1/r_1 & \leq & \frac{15}{8\sqrt{2}}-1(\approx 0.325),\\ r_1/r_0 & \leq & \frac{1}{2}+\frac{\sqrt{31}}{16}(\approx 0.847),\\ r_1/r_0 & \geq & \frac{1}{2}-\frac{\sqrt{31}}{16}(\approx 0.152).\end{array}\right. \tag{3.7}$$

Of course, such bounds can be found for other bidisperse systems, or for more complicated polydisperse systems but in those cases it is strongly advised to solve system (3.7) using adequate numerical methods.

## 3.3 Building and handling the triangulation

The weighted Delaunay triangulation used in the contact detection method provides a way to select pairs of particles that may experience a contact, which reduces the number of contacts to be tested from $O(n^2)$ to $O(m)$ ($n$ being the number of particles and $m$ being the number of edges in the triangulation). It will be shown in chapter 4 that for bounded particle shape complexities, in practical cases $m = O(n)$. This means that our contact detection method reduces the number of pairs to be tested from $O(n^2)$ to $O(n)$. In order to achieve this complexity, special attention has to be given to the way the triangulation used in the contact detection method is built and handled through the simulation process. Indeed, this maintenance contributes to the complexity of the method. In this section we describe the way this triangulation is built and handled with the motion of the grains.

For the sake of simplicity we deal here with triangulations which have exactly 4 exterior vertices constituting a tetrahedron $T$. This simplifies the implementation of the method, ensuring that the number of exterior vertices remains constant. Though the interior points of the triangulations dealt with here will be free to move, $T$ itself remains motionless. Moreover, no interior point is allowed to escape from $T$.

### 3.3.1 Building the initial triangulation

Assume we have a set of spheres $S_{-3}$, ..., $S_n$ with centers $x_{-3}$, ..., $x_n$ so that $S_{-3}$, $S_{-2}$, $S_{-1}$ and $S_0$ are the spheres of radii 0 whose centers are the vertices of tetrahedron $T$. In order to build the weighted Delaunay triangulation generated by spheres $(S_i)_{-3\leq i\leq n}$, we use the incremental method first introduced in [Joe89] for Delaunay triangulations and generalized in [ES96] to weighted Delaunay triangulations. The method starts with the weighted Delaunay triangulation $T_0$ generated by the four spheres $S_{-3}$, ..., $S_0$. This is the only triangulation that admits $T$ as its unique maximal face. At this point, vertices $x_1$, ..., $x_n$ are still missing in the triangulation. The method consists in inserting $x_1$, ..., $x_n$ in this sequence by performing flips. This will successively produce the weighted Delaunay triangulations $T_i$ generated by spheres $S_{-3}$, ..., $S_i$ for $1 \leq i \leq n$.

Assume that triangulation $T_i$ has been built and call $f$ the face of $T_i$ that contains $x_{i+1}$ and whose dimension is minimal. We can deduce from the structure of $T_i$ as a triangulation that the vertex set of $f$ together with $x_{i+1}$ is a flippable circuit in $T_i$. Moreover, flipping this circuit in $T_i$ produces a triangulation $T_i'$ of the point configuration $\{x_{-3}, ..., x_{i+1}\}$. It is shown in [ES96] that one can successively perform flips supported by circuits containing $x_{i+1}$ from $T_i'$ to the weighted Delaunay triangulation generated by spheres $S_{-3}$, ..., $S_{i+1}$, that is $T_{i+1}$. The circuits $Z$ to be flipped will be those that

successively minimize the power distance of $x_{i+1}$ with respect to the circumsphere $S$ of $Z \setminus \{x_{i+1}\}$ that is $\|x_{i+1} - c\|^2 - R^2$ where $R$ is the radius of $S$ and $c$ its center. We will not go into further details, but the reader can refer to [ES96] for formal proofs.

It is possible to build the weighted Delaunay triangulation from scratch whenever needed using the above algorithm. Still, one can use the motion of the particle to design a faster procedure. Indeed, the topology of a weighted Delaunay triangulation generated by a set of spheres will change little if those spheres move a little. Since the contact detection will be made at frequencies of the order of $1/\Delta t$ where $\Delta t$ is the time-step of the integration, the motion of the spheres between two detections should be limited and only minor topological changes should be needed between a triangulation and the next one.

### 3.3.2 Triangulation Maintenance

We introduce the time-dependence of the geometrical system in the form of a functional notation. Call $x_i(t)$ the center of sphere $S_i$ and $T(t)$ is the weighted Delaunay triangulation generated by spheres $S_{-3}$, ..., $S_n$ at time $t$. For $t' \geq t$, call $T(t,t')$ the set obtained from triangulation $T(t)$ if one moves its vertices from their positions at time $t$ to their position at time $t'$ without changing its topology. Formally, $T(t,t') = \{\text{conv}(\{x_i(t') : i \in I\}) : \text{conv}(\{x_i(t) : i \in I\} \in T(t)\}$. Three cases can occur :

- $T(t,t')$ and $T(t')$ are identical,
- $T(t,t')$ and $T(t')$ are different but $T(t,t')$ still is a triangulation,
- $T(t,t')$ is not a triangulation any more.

In the first of above cases, no change need be done to the topology of $T(t)$ between times $t$ and $t'$. In the second case, topological changes are needed to obtain $T(t)$ from $T(t')$, but those changes can directly be made on $T(t,t')$ whose geometrical structure can be taken advantage of. This is the case we address in this section. The last of above cases where $T(t,t')$ is not a triangulation any more requires that a particular version of the regularization algorithm be implemented which will be addressed in chapter 4.

Observe that the vertex sets of $T(t,t')$ and $T(t')$ are identical. According to theorem 7 we can then hope that starting with $T(t,t')$ and successively flipping illegal flippable facets, we will eventually reach $T(t')$. Unless we get stuck with a triangulation that still admits illegal facets, none of which is flippable. Our regularization algorithm 1 bets that $T(t,t')$ can be flipped to $T(t')$ anyway.

Many hundreds of simulation runs have been carried out. Within each of these, the above algorithm has been performed millions of times. It never failed. This means that all triangulations met in the course of the flipping process either were the expected weighted Delaunay triangulation or had facets simultaneously illegal and flippable. As a reason for this, one could invoke the proximity of $T(t,t')$ and $T(t)$. Indeed, since

**Algorithm 1** Regularization algorithm

$T \leftarrow T(t, t')$
**while** $T$ contains an illegal facet **do**
  **if** $T$ admits a facet $f$ that simultaneously is illegal and flippable **then**
    flip $f$ in $T$
  **else** {no facet of $T$ is simultaneously illegal and flippable}
    return failure statement
  **end if**
**end while**

it is close to $T(t)$, triangulation $T(t, t')$ could still be regular. Corollary 1 then predicts that there is a way to flip $T(t, t')$ into $T(t')$. Though, finding the succession of flips to perform requires that a height function realizing $T(t, t')$ be known which is not the case. However, one can show that all facets that will be flipped out in the sequence exhibited by corollary 1 are illegal, which means that, provided $t$ and $t'$ are close enough, a succession of illegal flippable facets exists between $T(t, t')$ and $T(t')$. But the fact that our algorithm never fails further suggests that any triangulation can be transformed into a weighted Delaunay triangulation by only flipping illegal facets as soon as their vertex sets are identical.

# Chapter 4

# Some implementation details

## 4.1 Intoduction

This chapter is dedicated to the implementation of a DEM simulation code using the method introduced in chapters 2 and 3. The DEM code of J.-A. Ferrez [Fer01; FL02] served as a basis for our implementation. This code was written in C++, a language which has the advantages to be widely available, to include built-in data structures through the Standard Template Library (STL) and to allow object oriented programming. The code by J.-A. Ferrez was originally designed to handle spherical particle and featured a number of functionalities such as a save and restore ability, exact floating point geometrical computations and a parallelized version.

The contact detection method between spheres already used weighted Delaunay triangulations as described in section 3.1 of chapter 3 (see also [Fer01] for further details), and all the structure to build and handle them, in particular data structures, were already implemented. A contact detection method using spacial sorting techniques was implemented later by M. Weber in the code of J.-A. Ferrez. At the time, a problem of degeneracies in the triangulations used for the detection of contacts was found to occur with setups involving particularly large scale differences. However, this was not a structural default of the implementation, nor was it a theoretical failure of the contact detection method (one could have thought about algorithm 1 failing to regularize a triangulation to the expected weighted Delaunay triangulation). This actually was due to the geometrical object to be regularized by algorithm 1 to be geometrically too far from a triangulation. This topic is addressed in section 4.3 below, where we propose a solution to this degeneracy problem.

In this chapter we only describe the differences between the original code and its modified version that handles non-spherical particles. For more details about the original code by J.-A. Ferrez, we encourage the reader to refer to [Fer01; FL02].

## 4.2 Structure of the simulation environment

The original structure of the code by J.-A. Ferrez was organized as shown in figure 4.1. There are a module for DEM that deals with the physical model for grains and contacts, a geometrical module that handles the dynamic weighted Delaunay triangulations and a container module responsible for the management of the data that either provides access of every element of the simulation to other elements and undertakes the exporting of data and statistics. On top of this, one finds the two kinds of simulation loops that can be used: one for single processor computations and the other for shared memory parallel computing. The nice thing there is the natural correspondence between the geometrical object and the physical ones. Indeed, spherical particles are in one-to-one correspondence with their centers, i.e. the vertices of the triangulation and the sphere-sphere contacts will be found among the edges of this triangulation. This coherence explains the choice of a dependence between physical and geometrical classes as shown in figure 4.1. As one can see in figure 4.1, force models, wall shapes or exporters can be added easily in the code. A description of the force model refered to as *Pournin's* can be found in [PLM02].

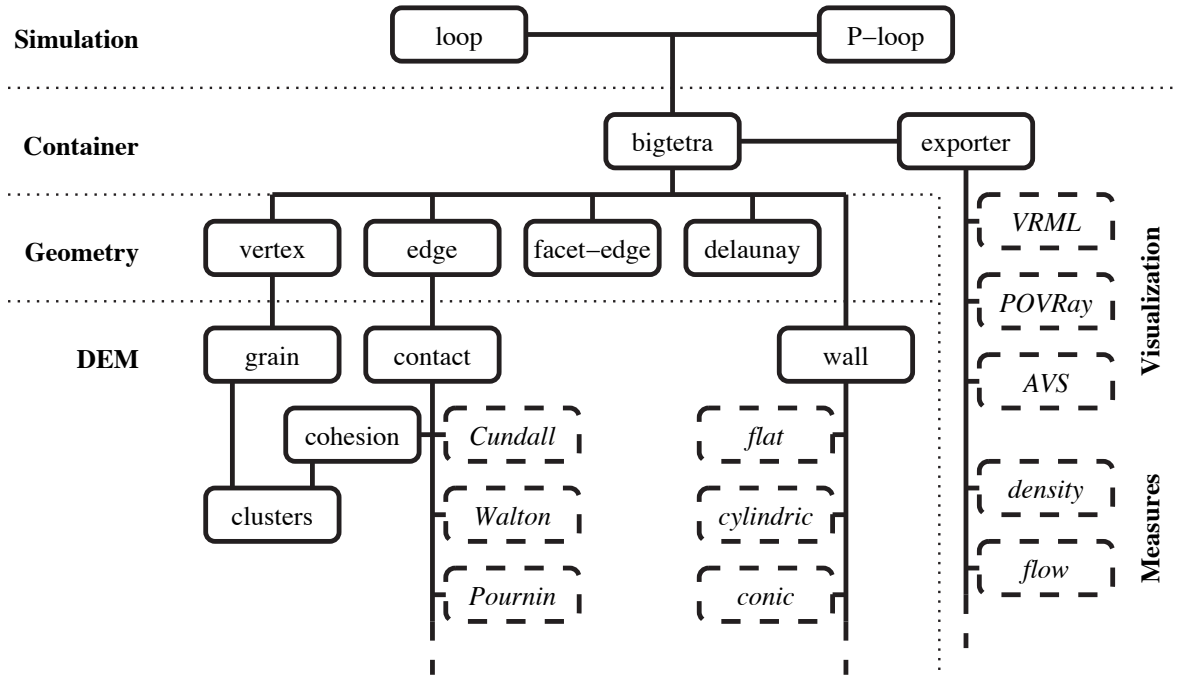


Figure 4.1: Original structure of the simulation environment by J.-A. Ferrez (Figure taken from [Fer01])

However, this nice correspondence does not exist any more with our non-spherical particles. Each particle is associated with those vertices of the triangulation that are the centers of its covering spheres and there may be several of them. Because of this, a pair of particles may have several edges of the triangulation between them that do not necessarily correspond to contacts. Therefore, we had to modify the class dependences as shown in figure 4.2. Both particle and contact classes now depend directly on *bigtetra*, where they used to depend on *vertex* and *edge* respectively. The link between particles and their covering spheres is now undertaken by a list of pointers on

the vertices of the triangulation. So far only spherosimplices (spheres, spherocylinders, spherotriangles and spherothetrahedra) have been implemented.

The class *particle* defines the mass center $c$ of a particle and three vectors $v_1$, $v_2$ and $v_3$ so that the vertices of the particle's skeleton will be found among $c + v_1$, $c + v_2$, $c + v_3$ and $c - v_1 - v_2 - v_3$. For a sphere, $v_1 = v_2 = v_3 = 0$. For a spherocylinder, $v_2 = v_3 = 0$ and the vertices of its skeleton are $c \pm v_1$. For a spherotriangle, $v_3 = 0$ and the vertices of its skeleton are $c + v_1$, $c + v_2$ and $c - v_1 - v_2$. The vertices of a spherotetrahedron's skeleton are $c + v_1$, $c + v_2$, $c + v_3$ and $c - v_1 - v_2 - v_3$. A further step in the development of the code is to split this class into classes that correspond to each particle shapes, including more complex shapes (convex ones to begin with, like *spherocubes*). This would allow to save memory by avoiding the storage of useless information.

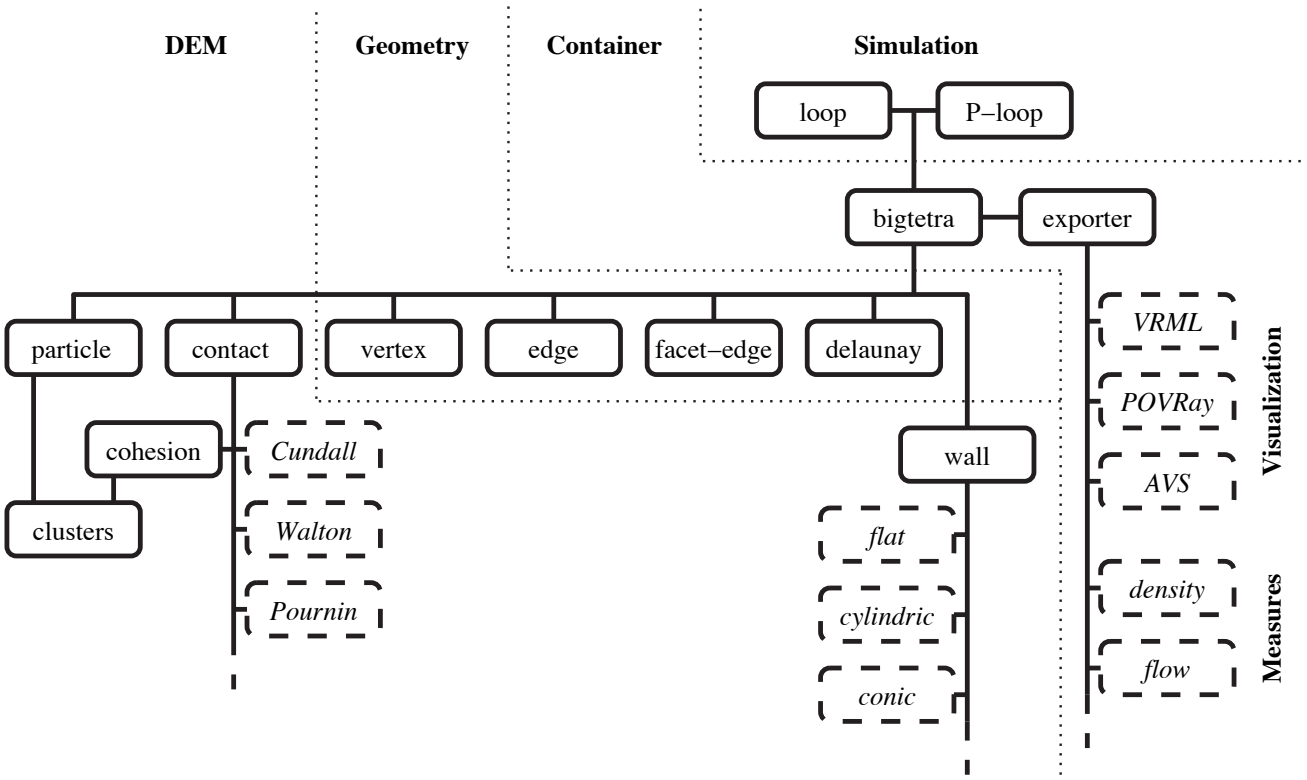


Figure 4.2: Modified structure with implementation of non-spherical particles.

In our implementation, all particles are convex and only one contact per particle pair is possible. Knowing the two contacting particles, one can define a contact entirely. However, in the case of non-convex particles, several contacts may occur between the same particle pair and tracking them between time steps is required. Indeed, some of the quantities used to compute contact forces, such as the tangential overlap need to be remembered from one time step to the next. If several contacts are possible, one has to be able to find which is the contact this information belongs to. The handling of non-convex particles requires that such tracking procedures be available, which requires further implementation work.

## 4.3 Enhancing the robustness of triangulation maintenance

The original implementation implicitly assumed that when moving the vertices of a triangulation between times $t$ and $t'$ without changing its topology, the resulting collection $T(t,t')$ of simplices still was a triangulation. This assumption is indeed valid when $t$ and $t'$ are close enough. In practical cases though the time step $\Delta t = t' - t$ used for the integration of the motion equations is limited by the available computing power and some experiments with particularly large setups caused the regularization algorithm to fail, even with time steps less than $10^{-6}$ s. This failure was not a theoretical failure of the regularization algorithm. The set $T(t,t')$ could not be regularized because it was geometrically too far from a triangulation. Observe though, that for limited degeneracies, algorithm 1 would still be able to repair $T(t,t')$. The first solution was to decrease the value of $\Delta t$, which would solve the problem in most practical cases, but would not guarantee the robustness of the algorithm. Further, this assumes that such small time steps are computationally affordable.

We chose instead to implement a tracking algorithm that detects the degeneracies that occur in the triangulation when its vertices move. Observe first that within a time step of the integration process, accelerations are kept constant, meaning that the positions of the spheres can be easily known. Assume that some spheres move with constant accelerations between times $t$ and $t'$. Call $T(u)$ the weighted Delaunay triangulation generated by those spheres at time $u \in [t,t']$. Let $f(u)$ be an interior facet of $T(u)$, $a(u)$, $b(u)$, $c(u)$ its vertices and $d(u)$ and $e(u)$ the vertices of $T(u)$ so that $\mathrm{conv}(f(u) \cup \{d(u)\})$ and $\mathrm{conv}(f(u) \cup \{e(u)\})$ are maximal faces of $T(u)$. At time $t$, $f$ is legal according to theorem 6. When the vertices of $f$ move with time, $f$ may become illegal. From the definition of legality, and from equation (1.1), the time when $f$ becomes illegal is the smallest zero in $[t,t']$ of the following determinant taken as a function of $u$:

$$D_f(u) = \begin{vmatrix} a_x(u) & a_y(u) & a_z(u) & \|a(u)\|^2 - R_a^2 & 1 \\ b_x(u) & b_y(u) & b_z(u) & \|b(u)\|^2 - R_b^2 & 1 \\ c_x(u) & c_y(u) & c_z(u) & \|c(u)\|^2 - R_c^2 & 1 \\ d_x(u) & d_y(u) & d_z(u) & \|d(u)\|^2 - R_d^2 & 1 \\ e_x(u) & e_y(u) & e_z(u) & \|e(u)\|^2 - R_e^2 & 1 \end{vmatrix}, \tag{4.1}$$

where $R_p$ is the radius of the sphere centered at vertex $p$, and $p_x(u)$, $p_y(u)$ and $p_z(u)$ its coordinates along each axis at time $u$. If determinant taken as a function of $u$ does not have a zero in $[t,t']$, $f$ will remain legal in this time interval. The overall idea of our tracking algorithm is the following. Solving $D_f(u) = 0$ for $u$ provides the time $u_f \in [t,t']$ when $f$ becomes illegal, if there is one. Doing this for every interior facet of $T(t)$, one obtains the list of facets to be flipped to obtain the weighted Delaunay triangulations generated by our spheres at time $t'$, but also the order in which they should be flipped. Indeed, if $u_f < u_{f'}$, $f$ should be flipped before $f'$. Performing those flips topologically in this sequence from $T(t,t')$ produces successive sets of simplices. Those sets of simplices will be topologically identical to the weighted Delaunay triangulations successively generated by our spheres while their centers move between times $t$ and $t'$. As a consequence, the collection of simplices eventually obtained is the

expected weighted Delaunay triangulation generated by our set of spheres at time $t'$. Of course, each time a facet is flipped, one needs to update the value of $u_f$ for the facets $f$ topologically affected by this flip (including the facets created by this flip).

Observe that the algorithm which we have just sketched requires that $D_f(u) = 0$ be solved. Since the vertices of triangulation $T$ have constant accelerations between times $t$ and $t'$, their coordinates are quadratic functions of time. According to equation (4.3), $D_f(u)$ is therefore a polynomial of degree 10. In our regularization context though, only positions at times $t$ and $t'$ matter. In between, the trajectories of the triangulation's vertices are only required to be continuous and we can simplify the physical quadratic motions to abstract linear ones between times $t$ and $t'$. The position of a vertex $p$ of $T$ at time $u \in [t, t']$ will then read:

$$p(u) = (1 - u)p(t) + up(t'). \tag{4.2}$$

Using equation (4.2), $D_f(u)$ simplifies to a polynomial of degree 5. Observe that this polynomial has no analytical expression for its roots, and solving $D_f(u) = 0$ for $u$ then requires that some numerical method be used. Following the above observations, we propose algorithm 2 for the regularization of our triangulations.

**Algorithm 2** Robust regularization algorithm

```
L ← ∅
for all facet f interior to T do
  compute the roots of D_f(u)
  if D_f(u) admits a root in [t, t'] then
    u_f ← the smallest root of D_f(u) in [t, t']
    insert f in L in increasing order of u_f
  end if
end for
while L ≠ ∅ do
  flip the first element g of L
  for all facets f affected by the flip do
    if f is in L then
      remove f from L
    end if
    compute the roots of D_f(u)
    if D_f(u) admits a root in ]u_g, t'] then
      u_f ← the smallest root of D_f(u) in ]u_g, t']
      insert f in L in increasing order of u_f
    end if
  end for
end while
```

Algorithm 2 has three advantages over algorithm 1. According to the above discussion, the first of these advantages is that its convergence is guaranteed even if the flip-graph is not connected. Its second advantage is that the sequence of flips it performs is

uniquely determined, which was not the case for algorithm 1. The third advantage of algorithm 2 over algorithm 1 is that it handles the case of degenerated triangulations, which is the reason why we designed it.

We now propose an alternate robust regularization algorithm. Again, let $f(u)$ be an interior facet of $T(u)$, $a(u)$, $b(u)$, $c(u)$ its vertices and $d(u)$ one of the vertices of $T(u)$ so that $\text{conv}(f(u) \cup \{d(u)\})$ is a maximal face of $T(u)$. Call $\alpha(u)$ the vector product $(b(u) - a(u)) \wedge (c(u) - a(u))$. When the spheres move with time, $\text{conv}(f \cup \{d\})$ may become flat. The time when simplex $\text{conv}(f \cup \{d\})$ becomes flat is the smallest zero in $[t, t']$ of the following expression taken as a function of $u$:

$$H_f(u) = [(c(u) - a(u)) \wedge (b(u) - a(u))] . [d(u) - a(u)] . \tag{4.3}$$

using linear motions for the spheres according to equation (4.2), $H_f(u)$ is a polynomial of degree 3. Before any interior facet of $T(u)$ becomes flat, $T(u)$ is a triangulation that can be successfully regularized by algorithm 1. Following this observation, we propose algorithm 3 as an alternative to algorithm 2.

The integer $k$ used as a parameter of this algorithm must be strictly positive. It reflects the number of local degeneracies of $T$ algorithm 1 is able to bear. Taking $k = 1$ means that the regularizations carried out in algorithm 3 will only process triangulations. As a consequence, this algorithm prevents the failures of algorithm 1 caused by degeneracies of the triangulation. The other parameter of algorithm 3 is the real number $\varepsilon$ that should be strictly positive, yet small enough for the regularization to happen around the expected value of $u$.

While algorithm 3 solves the degeneracy problems that caused algorithm 1 to fail, it still relies on it for the regularization of a number of triangulations. Therefore, its theoretical convergence is not guaranteed since it depends on the connectivity of the flip-graph. Again, since this theoretical failure never occurred in practical cases, this does not seem to be much of a threat. Observe though that algorithm 3 has the advantage over algorithm 2 that analytical expressions exist for the roots of $H_f(u)$ since they are polynomials of degree 3.

## 4.4 Experimental complexity analysis

As already mentioned in chapter 3, the complexity of our triangulation-based contact detection method is proportional to the number of edges of the involved triangulations. There exist weighted Delaunay triangulations in three dimensions whose number of edges are quadratic functions of their number of vertices. Following this, the theoretical upper bound for the complexity of our contact detection method is $O(n^2)$. Since the computational cost of managing the triangulation is high, this suggests that our contact detection algorithm is slower than the naive quadratic algorithm ! However, the examples of quadratic Delaunay triangulations involve degenerate situations where most vertices lie on few line segments. Intuition suggests that the probability

**Algorithm 3** Alternative robust regularization algorithm

$L \leftarrow \emptyset$
**for all** facet $f$ interior to $T$ **do**
  compute the roots of $H_f(u)$
  **if** $H_f(u)$ admits a root in $[t, t']$ **then**
    $u_f \leftarrow$ the smallest root of $H_f(u)$ in $[t, t']$
    insert $f$ in $L$ sorted in increasing order of $u_f$
  **end if**
**end for**
**while** $L \neq \emptyset$ **do**
  **if** $L$ admits more than $k$ elements **then**
    $g \leftarrow$ the $k^{th}$ element of $L$.
  **else** {$L$ has less than $k$ elements}
    $g \leftarrow$ the last element of $L$
  **end if**
  move the vertices of $T$ to their position at $u_g - \varepsilon$
  regularize $T$ using algorithm 1
  **for all** interior facets $f$ affected by the regularization **do**
    **if** $f$ is in $L$ **then**
      remove $f$ from $L$
    **end if**
    compute the roots of $H_f(u)$
    **if** $H_f(u)$ admits a root in $]u_g, t']$ **then**
      $u_f \leftarrow$ the smallest root of $H_f(u)$ in $]u_g, t']$
      insert $f$ in $L$ in increasing order of $u_f$
    **end if**
  **end for**
**end while**
move the vertices of $T$ to their position at $t'$
regularize $T$ using algorithm 1

of such events is small, and the bet of J.-A. Ferrez was that in all practical cases the number of edges of the triangulation is a linear number of its vertices. In this section we present results on the overall complexity of the simulation process, obtained from a set of simulations and corresponding measures of the number of edges of the weighted Delaunay triangulation.

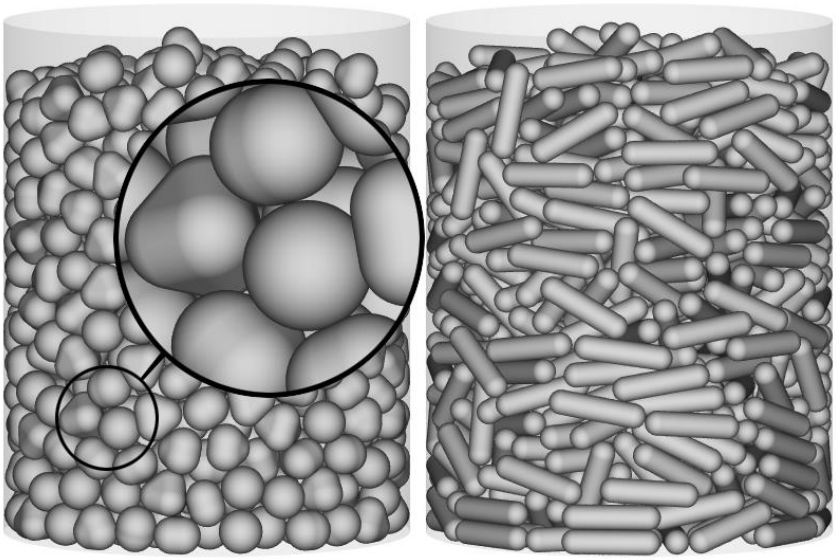

Figure 4.3: Snapshots of final states of numerical experiments. Left : experiment 1, right : experiment 3.

Snapshots of simulations performed with the non-spherical version of our code are shown in figure 4.3. Those experiments consist in pouring particles into a cylindrical container of diameter 20 mm. This means that the number of particles gradually increases while the simulation proceeds. All particles have eight times the volume of a sphere of diameter 1 mm, independently of their shape. Experiment 1 involves 250 spherosimplices of each kind. Experiment 2 involves 500 spheres and 500 spherotetrahedra, and experiments 3 and 4, 1000 spherocylinders each.

For the first two experiments, each particle only uses only one covering sphere for contact detection. This is achieved by calibrating every shape the same way the spherotetrahedra have been calibrated at the end of chapter 3. This constraint actually limits the particle's sharpness. Still, those particles are far from spherical and this way, the complexity of contact detection is the same as if all particles were spheres. In experiment 3, spherocylinders have an elongation coefficient $l/r$ of 3, where $l$ is half the length of the segment constituting their skeletons and $r$ is their radius. With such elongated shapes, 5 covering spheres per particle are needed. In experiment 4, the elongation coefficient $l/r$ is 6, and 9 covering spheres are needed for a particle. In every experiment, $\xi_m = 5 \times 10^{-5}$ m.

The computing time of the DEM process, including contact detection, is plotted in figure 4.4 against the number of simulated particles. In all cases it is almost linear. Observe that the slope of this linearity increases with particle elongation, naturally reflecting that the number of possible contacts is higher for elongated particles. The inset

shows the number of edges of the triangulation, plotted against the number of covering spheres and the four cases turn out to be identically linear. The slope of around 7 is close to the coordination number of random close-packed spheres, indicating that our method appropriately identifies the pairs of particles to be tested for contact.

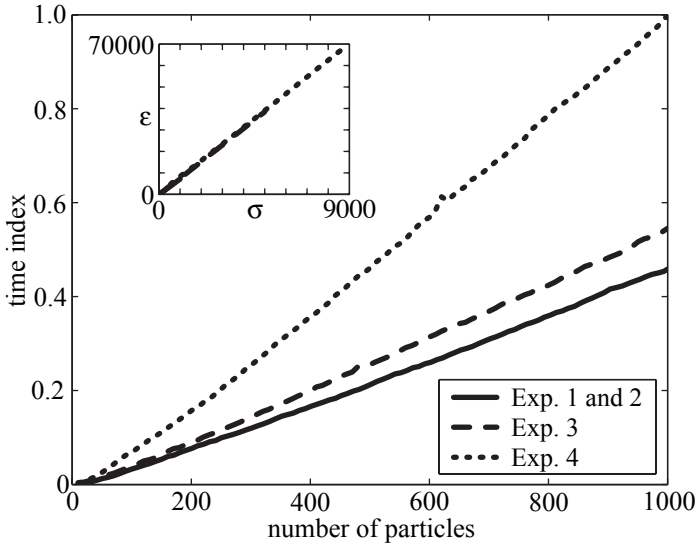


Figure 4.4: Actual computing time of the DEM process plotted against the number of simulated particles for all four experiments. The *time index* is normalized to 1 for 1000 of the last experiment's spherosegments. Each point is averaged over 400 DEM iterations. Inset : number $\varepsilon$ of edges in the triangulation versus the number $\sigma$ of covering spheres for the same experiments.

## 4.5 Some inertia matrices

Let $P$ be a homogeneous particle, $G$ its mass center and $\omega$ its spin vector. If $P$ is submitted to a total force $f$ and a total momentum $M_G(f)$ at point $G$, the motion equations read:

$$\left\{ \begin{array}{rcl} m\ddot{G} & = & f \\ I_G\dot{\omega} & = & M_G(f) \end{array} \right. . \tag{4.4}$$

where $m$ is the mass of the particle and $I_G$ its inertia matrix at point $G$. One sees that $I_G$ is required when integrating the motion equations. Let $(G, x, y, z)$ be an orthonormal referential centered at point $G$. In this referential, the inertia moments of $P$ read:

$$\begin{cases} I_{xx} &= \rho \int_P y^2 + z^2 dxdydz \\ I_{yy} &= \rho \int_P x^2 + z^2 dxdydz \\ I_{zz} &= \rho \int_P x^2 + y^2 dxdydz \\ I_{xy} &= -\rho \int_P xydxdydz \\ I_{xz} &= -\rho \int_P xzdxdydz \\ I_{yz} &= -\rho \int_P yzdxdydz \end{cases}, \tag{4.5}$$

where $\rho$ is the density of $P$. Using equations (4.5.1), $I_G$ reads:

$$I_G = \begin{pmatrix} I_{xx} & I_{xy} & I_{xz} \\ I_{xy} & I_{yy} & I_{yz} \\ I_{xz} & I_{yz} & I_{zz} \end{pmatrix}. \tag{4.6}$$

In order to apply the DEM process, it is required that $I_G$ be known. If $P$ is a sphere with radius $r$, $I_G$ simply is the diagonal matrix whose diagonal elements are identically equal to $\frac{2}{5}mr^2$. However, analytical expressions of the inertia matrices of more complex shapes may be difficult to find. In this section we describe the methods we use to estimate integrals (4.5.1) and give analytical expressions of $I_G$ for regular spherosimplices.

### 4.5.1 Inertia matrix estimation

The inertia moments of a particle $P$ with any shape can be statistically estimated using a reject method. Let $V$ be the random variable uniform on $P$. Calling $v$ the volume of $P$, the density of $V$ reads:

$$f_V = \frac{1}{v}\mathbb{1}_P. \tag{4.7}$$

Let $X$, $Y$ and $Z$ be the margins of $V$. According to equation (4.7), their variances and covariances read:

$$\begin{cases} \mathrm{var}(X) = \frac{\rho}{m} \int_P x^2 dxdydz \\ \mathrm{var}(Y) = \frac{\rho}{m} \int_P y^2 dxdydz \\ \mathrm{var}(Z) = \frac{\rho}{m} \int_P z^2 dxdydz \\ \mathrm{cov}(X,Y) = \frac{\rho}{m} \int_P xydxdydz \\ \mathrm{cov}(X,Z) = \frac{\rho}{m} \int_P xzdxdydz \\ \mathrm{cov}(Y,Z) = \frac{\rho}{m} \int_P yzdxdydz \end{cases}. \tag{4.8}$$

Comparing the inertia moments and products of $P$ with those variances and covariances we obtain the following expression for the inertia matrix:

$$I_G = m \begin{pmatrix} \mathrm{var}(Y)+\mathrm{var}(Z) & -\mathrm{cov}(X,Y) & -\mathrm{cov}(X,Y) \\ -\mathrm{cov}(X,Y) & \mathrm{var}(X)+\mathrm{var}(Z) & -\mathrm{cov}(Y,Z) \\ -\mathrm{cov}(X,Z) & -\mathrm{cov}(Y,Z) & \mathrm{var}(X)+\mathrm{var}(Y) \end{pmatrix}. \tag{4.9}$$

A convenient way to estimate $I_G$ is therefore to estimate the variances and covariances of the margins of $V$. This can be done by using an accept-reject method to simulate $V$ and by building the covariance matrix of the obtained data.

This method is convenient since it allows to compute the inertia matrix of any kind of shapes. The following subsection gives exact expressions of this matrix for spherocylinders and regular spherotetrahedra.

### 4.5.2 Exact inertia matrices of some spherosimplices

Let $P$ be a spherocylinder with mass center $G$ in the referential $(G,x,y,z)$ as that shown in figure 4.5.

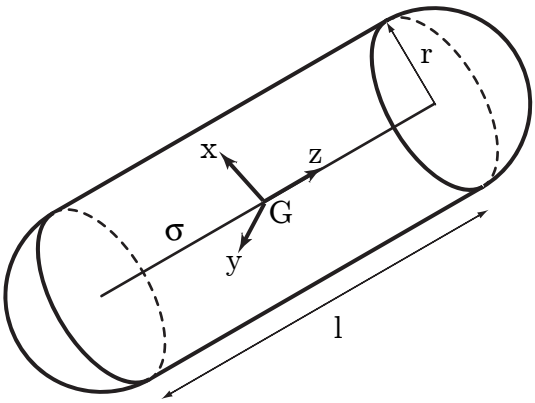


Figure 4.5: A spherocylinder of radius $r$ and skeleton $\sigma$ of length $l$ in the referential $(G,x,y,z)$.

The integrals (4.5.1) then express as follow:

$$\begin{cases} I_{xx} = I_{yy} = \frac{1}{3}\pi\rho r^3 l^2 + \frac{1}{12}\pi\rho r^2 l^3 + \frac{3}{4}\pi\rho r^4 l + \frac{8}{15}\pi\rho r^5 \\ I_{zz} = \frac{1}{2}\pi\rho r^4 l + \frac{8}{15}\pi\rho r^5 \\ I_{xy} = I_{xz} = I_{yz} = 0 \end{cases}. \tag{4.10}$$

Now assume that $P$ is a regular spherotetrahedron with mass center $G$ and radius $r$.

Calling $A$, $B$, $C$ and $D$ the vertices of $P$'s skeleton, and $l$ the distance between $G$ and any of those vertices. Let $(G,x,y,z)$ be the referential shown in figure 4.5 in which the

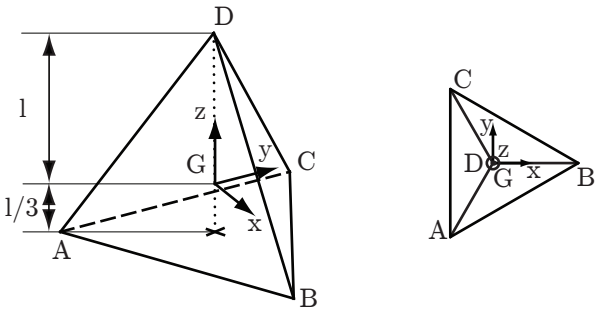


Figure 4.6: The skeleton of a regular spherotetrahedron of mass center $G$ and its associated referential $(G,x,y,z)$. Right : view from above.

coordinates of $A$, $B$, $C$ and $D$ are:

$$\begin{cases} A &= (-\frac{\sqrt{2}}{3}l, -\sqrt{\frac{2}{3}}l, -\frac{1}{3}l) \\ B &= (\frac{2\sqrt{2}}{3}l, 0, -\frac{1}{3}l) \\ C &= (-\frac{\sqrt{2}}{3}l, \sqrt{\frac{2}{3}}l, -\frac{1}{3}l) \\ D &= (0,0,l) \end{cases} . \tag{4.11}$$

The spherotetrahedron $P$ is composed of the tetrahedron $ABCD$ (figure 4.6), four prisms with thickness $r$ and triangles $ABC$, $ABD$, $ACD$ and $BCD$ as bases, six portions of a cylinder of radius $r$ corresponding to the edges of $ABCD$ and four portions of a sphere of radius $r$ corresponding to the vertices of $ABCD$. The last three basic shapes are shown on figure 4.7 with the referentials we use to represent them.

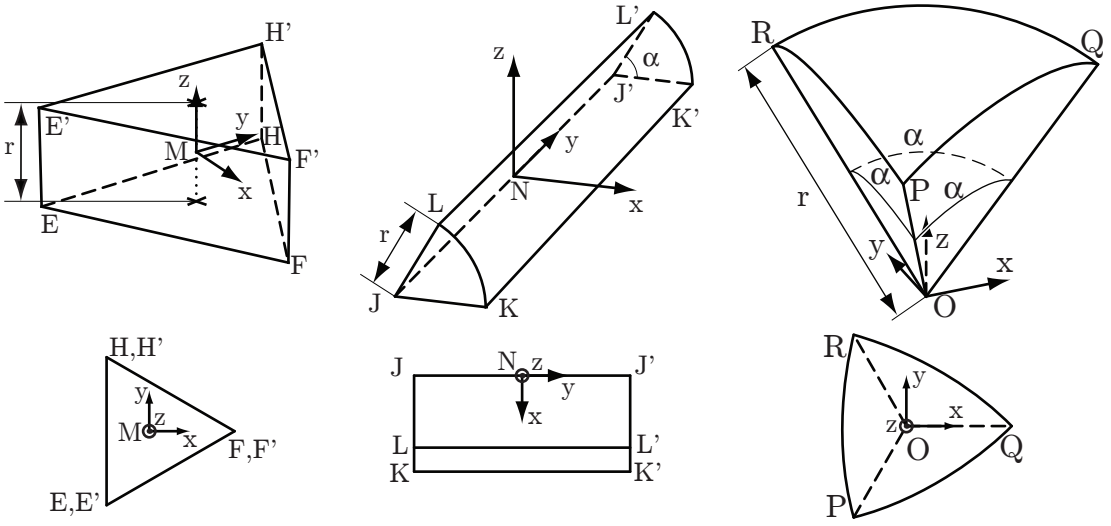


Figure 4.7: The three basic shapes that constitute a spherotetrahedron in addition to its skeleton. The referentials used to represent them are shown as well. Bottom : view from above.

In order to find $I_G$, we first calculate integrals (4.5.1) for each of the four basic shapes. By using Huygens theorem to translate the inertia moments and products, and rotating

them appropriately, one obtains the inertia matrices of each basic part constituting our spherotetrahedron. We then find the inertia matrix of $P$ by simply summing those matrices.

First of all, the angle $\alpha$ shown on the middle and right parts of figure 4.7 is the complementary to $\pi$ of the inner angle between two adjacent facets of a regular tetrahedron:

$$\alpha = \pi - \operatorname{atan}(2\sqrt{2}). \tag{4.12}$$

Integrating expressions (4.5.1) over tetrahedron $ABCD$ in the referential $(G, x, y, z)$, one obtains a diagonal inertia matrix whose diagonal elements are identically equal to:

$$I_{\text{tetrahedron}} = \rho \frac{16}{135\sqrt{3}} l^5. \tag{4.13}$$

This means that a regular tetrahedron has the same inertial behavior than a sphere. The inertia moments and products of the triangular shape $EFHH'F'E'$ left of figure 4.7 in the referential $(M, x, y, z)$ are:

$$\begin{cases} I_{xx} = I_{yy} = \frac{1}{6\sqrt{3}} \rho r^3 l^2 + \frac{2}{9\sqrt{3}} \rho r l^4 \\ I_{zz} = \frac{4}{9\sqrt{3}} \rho r l^4 \\ I_{xy} = I_{xz} = I_{yz} = 0 \end{cases}. \tag{4.14}$$

The inertia moments and products of the third shape $JKLL'K'J'$ in the middle of figure 4.7 in the referential $(N, x, y, z)$ are:

$$\begin{cases} I_{xx} = I_{zz} = \frac{1}{36\sqrt{3}} \rho \left( -4r^2 + \sqrt{2} \left( 8l^2 + 9r^2 \right) \alpha \right) r^2 l \\ I_{yy} = \frac{1}{\sqrt{6}} \rho \alpha r l^4 \\ I_{xz} = \frac{2\sqrt{2}}{9\sqrt{3}} \rho r^4 l \\ I_{xy} = I_{yz} = 0 \end{cases}. \tag{4.15}$$

The total inertia matrix of the four sphere portions $OPQR$ (right of figure 4.7) can be deduced from the inertia matrix of a sphere of radius $r$ and from the center of mass of $OPQR$ by using Huygens theorem and rotating the resulting matrices appropriately. The distance $d_v$ between $O$ and the mass center of $OPQR$ is:

$$d_v = \frac{3\sqrt{6}}{8\pi} r\alpha \tag{4.16}$$

One then finds that the total inertia matrix of the four parts $OPQR$ in referential $(G, x, y, z)$ of figure 4.6 is diagonal with its diagonal elements identically equal to:

$$I_{\text{vertices}} = \rho \frac{2}{405} \left( 108\pi r^5 + 135\sqrt{6}\alpha r^4 l + 180\pi r^3 l^2 \right). \tag{4.17}$$

The total inertia matrix of the four cylinder portions $JKLL'K'J'$ (middle of figure 4.7) can be deduced from equations (4.15) and from the center of mass of $JKLL'K'J'$ by using Huygens theorem and rotating the resulting matrices appropriately. The distance $d_e$ between $N$ and the mass center of $JKLL'K'J'$ reads:

$$d_e = \frac{4\sqrt{2}r}{3\sqrt{3}\alpha} \tag{4.18}$$

The total inertia matrix of the six parts $JKLL'K'J'$ in referential $(G,x,y,z)$ of figure 4.6 is diagonal with its diagonal elements identically equal to:

$$I_{\text{edges}} = \rho\frac{2}{9\sqrt{3}}\left(32rl + \sqrt{2}\left(9r^2 + 10l^2\right)\alpha\right)r^2 l. \tag{4.19}$$

The total inertia matrix of the four triangular portions $EFHH'F'E'$ (left of figure 4.7) can be deduced from equations (4.14) by using Huygens theorem and rotating the resulting matrices appropriately. This total inertia matrix, expressed in the referential $(G,x,y,z)$ of figure 4.6 is diagonal with its diagonal elements identically equal to:

$$I_{\text{triangles}} = \rho\frac{16}{9\sqrt{3}}\left(r^2 + rl + l^2\right)rl^2. \tag{4.20}$$

According to expressions (4.13), (4.20), (4.19), (4.17), $I_G$ is diagonal with its diagonal elements identically equal to:

$$I_P = \tfrac{4}{3}\rho\left(\tfrac{2}{5}\pi r^5 + \sqrt{6}\alpha r^4 l + \tfrac{2}{3}\left(\pi + \tfrac{10}{\sqrt{3}}\right)r^3 l^2 + \tfrac{1}{3\sqrt{3}}\left(4 + 5\sqrt{2}\alpha\right)r^2 l^3 + \tfrac{4}{3\sqrt{3}}rl^4 + \tfrac{4}{45\sqrt{3}}l^5\right). \tag{4.21}$$

This means that the inertia matrix of $P$ is that of a sphere.

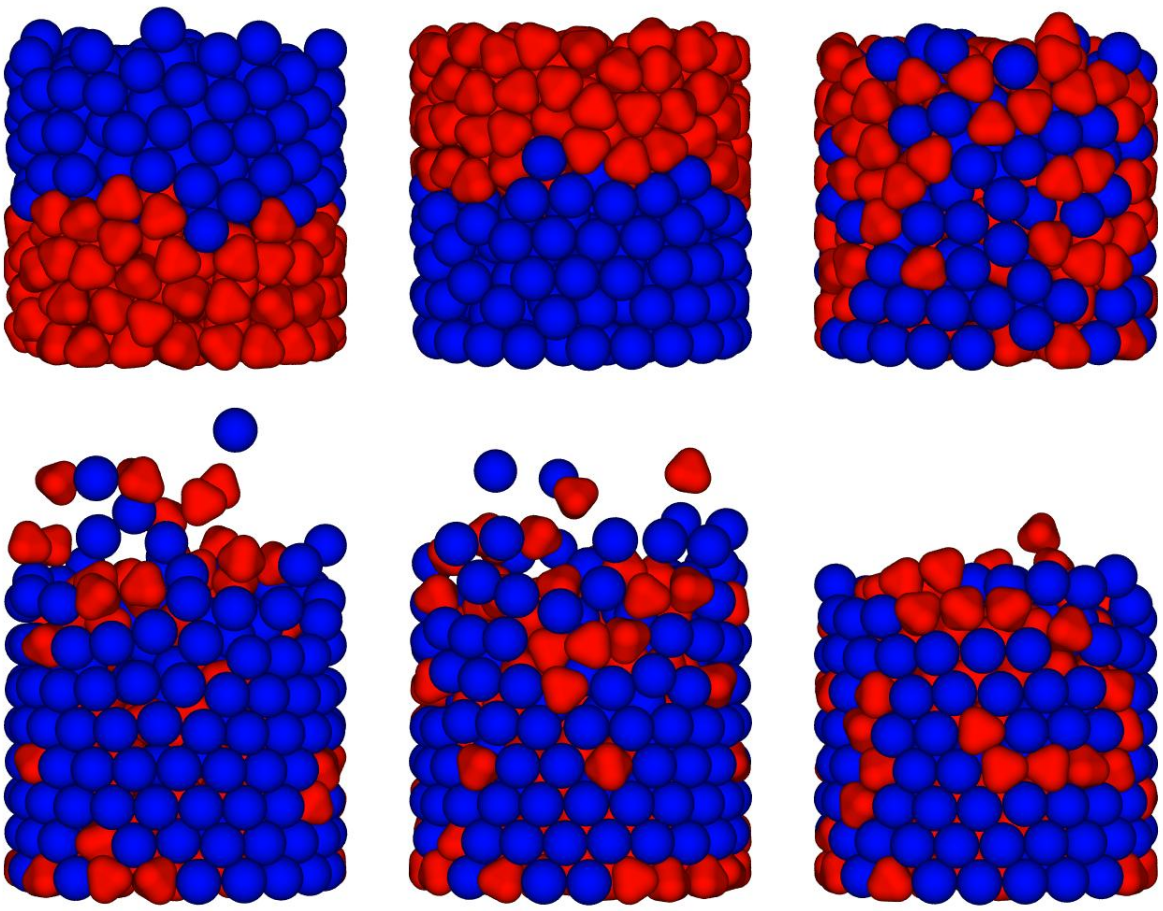

# Part II

# Applications

# Chapter 5

# A Study of Arching Effects and Flowability

Confined granular flows are known to arch suddenly about their confining bounaries under certain circumstances. As an effect, this causes jamming, i.e. prevents any further flowing motion of the medium. While this phenomenon may be due to microscopic interactions in fine powders, it also occurs with large grains in the form of mechanical equilibria induced by macroscopic forces. This phenomenon, refered to as "arching effect" is still little understood. It is a limiting cause for the *flowability* of powders, i.e. their ability to flow.

While the arching effect itself is difficult to encompass as a complex collective behaviour, flowability is a simple property that can be measured in a variety of ways and may provide insights into the mechanisms underlying the formation of arches. We choose here to investigate the flowability experiment that consists in opening a hole at the bottom of a grain-filled container and to check whether or not the medium flows.

The probability for such an assembly of beads of given *granulometry* and *surface properties* to flow in this experiment will be estimated as a function of the opening hole's diameter $D$. This will allow to determine the opening hole's diameter for which the probability for this medium to flow is 0.5, which we call its *mean critical diameter* $\bar{D}_c$. This diameter is the quantity we use to characterize the flowability of an assembly of beads.

Surface properties of the involved beads will be characterized with their mutual statical friction coefficient $\mu$. Numerical trials have been conducted with monodisperse bead assemblies and several friction coefficients. Experiments performed on the same monodisperse assemblies composed of steel beads show that those numerical models provide realistic values for $\bar{D}_c$.

Finally, measures of $\bar{D}_c$ for bidisperse assemblies of beads are obtained from numerically simulated trials of our flowability experiment. Those results show that for a given

friction coefficient, $\bar{D}_c$ only depends on the bead's mass-average diameter, which suggests that a law be formulated about the flowability of polydisperse bead assemblies.

## 5.1 The flowability experiment

In order to measure the flowability of a powder, we proceed with the following experiment. The setup used is a plexiglas cylinder with interchangeable aluminum discs at the bottom that feature circular holes in their centers. The inner diameter of the cylinder is 5 cm and the bottom discs have various diameters $D$ for their central holes. The hole of the bottom disc can be obturated using a shutter in aluminum as shown on the left side of figure 5.1.

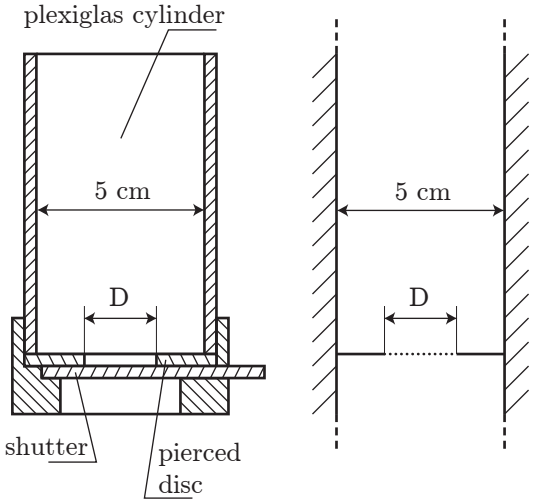


Figure 5.1: The experimental setup we use to measure the flowability of a bead assembly (left) and its numerical model (right). The shutter and the pierced disc of the experimental setup are numerically modeled by a circular hole sketched as a dotted line that can either be opened or closed.

The experiment proceeds as follows : the beads are poured into the cylinder while the hole of the bottom disc is obturated by the shutter. The granular piling to be processed is then obtained when a mechanical equilibrium is reached, all the beads being at rest. Finally the shutter is suddenly pulled out and the medium either flows through the hole of the bottom disc or blocks which is the result of the experiment. For our experimental trials, we used steel beads of diameters 1.0 mm, 4.0 mm, 5.0 mm and 7.0 mm. All trials were carried out with as close as possible to 0.575 kg of those steel beads, resulting in a filling height of around 6.5 cm independently of the bead diameters. When processing fine powders, a funnel is used to pour the medium into the cylinder. In our case of large beads however, this is superfluous. Indeed, using a funnel with a large enough opening for our beads to flow freely through it actually amounts to use no funnel at all.

Our flowability experiment were numerically reproduced with the Distinct Elements Method. Contacts will be modeled with a contact time of $t_c = 6.10^{-4}$ s and a restitu-

tion coefficient of $e_n = 0.4$ respectively quantifying the duration and the energy loss of simple contacts. Our numerical beads have a density of 7.8, which is that of our steel beads. The numerical setup is shown on the right part of figure 5.1.

Of course, numerical and experimental trials will not be carried out exactly the same way, due to their specific frameworks. Observe first that the combination of the pierced disc with the shutter acts as a slightly uneven bottom in the experimental setup while its numerical counterpart is perfectly flat. Then, removing the shutter in experimental trials applies a shear at the bottom of the granular piling. This is not the case in numerical trials where the area of the opening hole instantaneously disappears together with the contacting forces acting on it. The numerical bead-wall friction coefficients will be identical to the bead-bead friction coefficient, unlike in our experiments where friction occurs between steel, plexiglas and aluminum bodies. Finally, the initial pouring of the beads in the numerical framework and in the experimental one are quite different. Several methods exist to prepare numerical pilings [Bag05]. Those methods will produce initial situations that are often difficult to achieve in experimental preparations like homogeneous polydisperse pilings. This is our reason to use a simplified version of the sedimentation technique [Bag05] : we generate the beads randomly inside the containing cylinder, and we lower them vertically as densely as possible and as low as possible above the bottom plate which provides a preliminary state. Then, we simply let the beads fall under the action of gravity from this state which is already dense enough such that only few rearrangements are needed to producing the initial piling. In particular those rearrangements will not significantly disturb the homogeneity of the preliminary state in the case of bidisperse assemblies. It is noteworthy that in the experimental procedure, the pouring is from above the cylinder instead, which produces segregation in the case of bidisperse media. In the following, we assume that the effects of those differences between numerical and experimental trials can be neglected.

## 5.2 The mean critical diameter of a granular piling

The result of a flowability experiment will either be the observation “the medium blocks” or “the medium flows”. We will say that the medium flows if at the end of the experiment, no bead remains above the hole. Observe that this almost never corresponds to all beads flowing through the hole, as figure 5.2 suggests.

One could think of other ways to quantify the results of flowability trials. Call $m_i$ the mass of beads lying above the opening hole in the initial piling and $m_f$ the same mass taken at the end of the experiment. Then, the result of a flowability trial could be the ratio $m_f/m_i$. Figure 5.3 features a bar plot where the probability function $P(m_f/m_i)$ has been estimated over around 6000 numerical trials. As one can see, the probability for $m_f/m_i$ to lie between 0.01 and 0.99 is around 0.17. This shows that most of the arches occur immediately after the hole has been opened, which justifies our choice of a binary quantification of the experiment’s results.

By repeating the flowability experiment several times using assemblies of the same

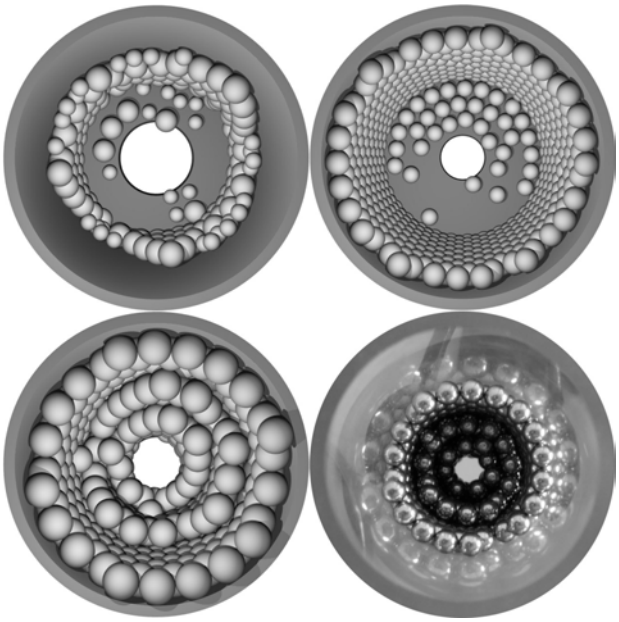

Figure 5.2: Top view of the final situations for four flowability experiments where the medium flowed. A photo of a real-world experiment is shown bottom-right while the three others are snapshots of the simulated setup.

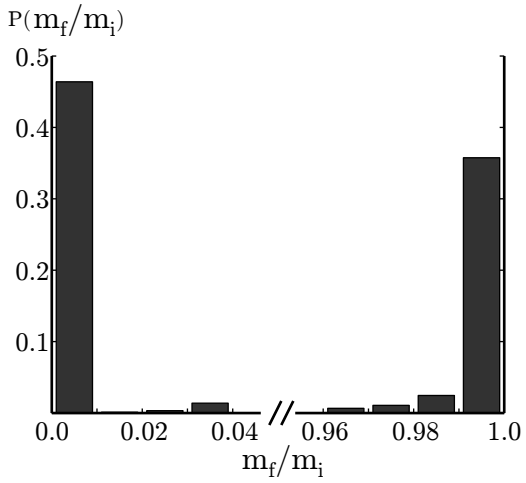


Figure 5.3: The probability function $P(m_f/m_i)$ of the ratio of the masses lying above the opening hole after ($m_f$) and before ($m_i$) the hole has been opened, estimated over 6246 monodisperse numerical trials.

beads, one can estimate the probability for them to flow through a hole of given diameter $D$. This allows in particular to find the statistical diameter $\bar{D}_c$ of the opening hole for which the probability for a medium to flow is 0.5. This diameter, called *mean critical diameter* is the quantity we choose to characterize the flowability of bead assemblies. In order to estimate $\bar{D}_c$, we process the flowability results using a generalized linear model [DH97]. An example of estimation this statistical model provides for $\bar{D}_c$ is shown on figure 5.4. All the confidence intervals we provide for $\bar{D}_c$ were found by

applying a bootstrap method [DH97] on the flowability results.

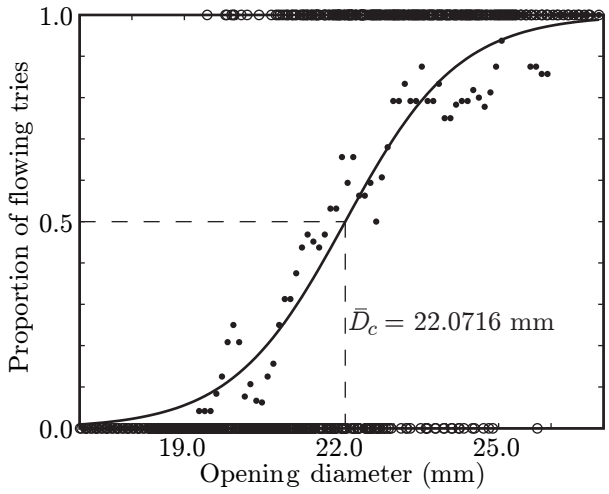


Figure 5.4: The proportion of flowing trials as a function of the diameter of the opening hole obtained from 510 numerical trials with monodisperse assemblies of beads of diameter 6 mm and mutual friction coefficient of $\mu = 0.8$. The raw results are indicated as small circles of coordinates $(D, r)$ where $D$ is the opening diameter and $r$ is 1 when the medium flows and 0 instead. The dots show the proportion of flowing trials in windows 0.4 mm large. The solid line shows the fit of the raw data obtained with an appropriate generalized linear model.

Intuition suggests that for a large enough number of flowability trials, the proportion of flowing trials will be an increasing function of the diameter of the opening hole. While it seems relevant to assume it, this property still needs to be checked. Indeed, we made at most 990 trials per medium with same granulometry and mutual friction coefficient. If ever this property turns out to be false, our mean critical diameter would be of a purely statistical nature but still could be defined as the diameter $\bar{D}_c$ for which the probability for the opening diameter of a flowing trial to be inferior to $\bar{D}_c$ is 0.5. Thus, our statistical measure keeps its intrinsic physical meaning.

Now consider some granular piling obtained prior to the hole opening. Our numerical framework makes it possible to try several diameters for the hole opening under this particular piling. One may wonder if a critical diameter exists for the hole, above which this piling will flow and below which an arch will form. Observe that this question cannot be answered by performing trials in our experimental framework. A same piling, prepared with beads of diameter 6 mm and mutual friction coefficient of $\mu = 0.8$, was subject to a set of 5000 flowability experiments with different diameters. The results of those trials, depicted in figure 5.5 clearly show that the answer to the above question is no. There are values $D_-$ and $D_+$ so that arching always occurs for $D < D_-$ and never for $D > D_+$, but the interval $[D_-, D_+]$ is significantly wide. This phenomenon could be further investigated, for example by finding how $D_+ - D_-$ depends on beads' diameters and mutual friction coefficients.

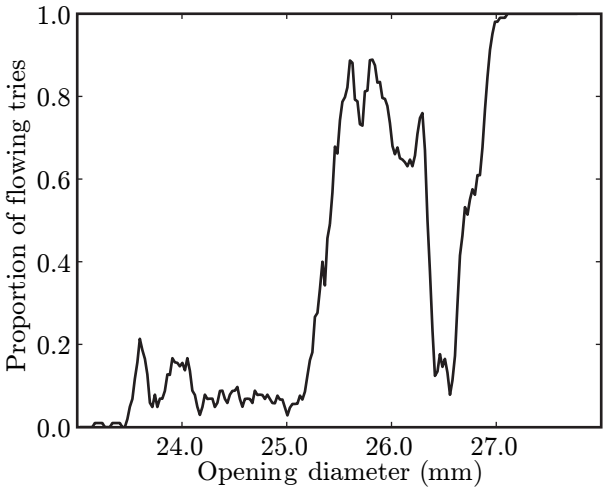


Figure 5.5: The proportion of flowing trials in windows 0.1 mm large obtained by submitting a given monodisperse piling of beads to a series of 5000 flowability tries with opening diameters ranging from 23.0 mm to 28.0 mm. The diameter of the beads is 6 mm and their mutual friction coefficient is $\mu = 0.8$.

## 5.3 The influence of friction

The flowability of a powder is known [Gio80] to reflect the friction coefficient of its constituting particles. In our macroscopic framework, this is still the case as shown in figure 5.6 for monodisperse sets of beads with diameters 4 mm, 5 mm and 7 mm. In particular, the mean critical diameter is a globally increasing function of the inter-particulate friction coefficient. Observe also that the influence of friction on the mean critical diameter is well marked for low values of the friction coefficient while it can practically be neglected for high ones.

| $\Phi$ (mm) | $\bar{D}_c$ (mm) |
|---|---|
| 1.0 | $3.88 \pm 0.15$ |
| 4.0 | $14.92 \pm 0.23$ |
| 5.0 | $17.46 \pm 0.37$ |
| 7.0 | $21.85 \pm 1.24$ |

Table 5.1: Results of experimental trials on monodisperse sets of steel beads.

The mean critical diameters measured from our experiments with steel beads are shown in table 5.1 and reported on figure 5.6 for $\Phi = 4.0$ mm, $\Phi = 5.0$ mm and $\Phi = 7.0$ mm. One can see that numerical and experimental trials show good agreement even though their respective frameworks are different. Observe that the differences between experimental values of $\bar{D}_c$ are qualitatively identical to the differences between numerical curves. This shows that the numerical model is coherent in the way it handles friction, and proves appropriate in the framework of flowability experiments.

Mean critical diameters were measured for monodisperse media with various bead diameters and friction coefficients. All those monodisperse results are shown on figure

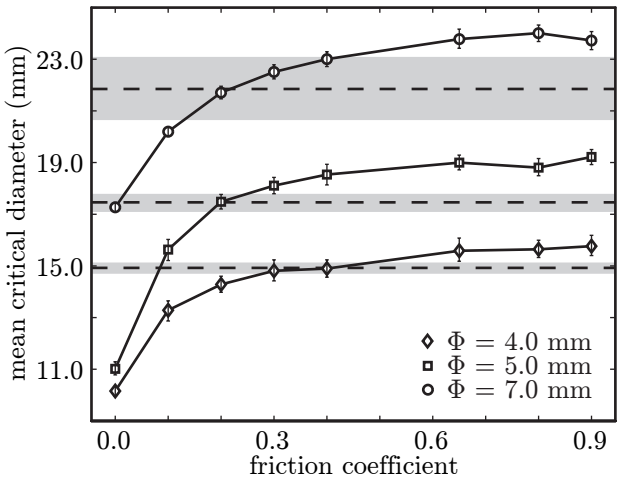


Figure 5.6: The mean critical diameter obtained from numerical trials as a function of the friction coefficient for beads of diameter 4 mm, 5 mm and 7 mm. Experimental values of table 5.1 together with their confidence intervals are reported on the graph respectively as dashed lines and greyed zones.

5.7. Observe that except for $\mu = 0.0$, the mean critical diameters are increasing, nearly affine functions of the beads diameters. The ratio of the mean critical diameter and the diameter of the beads lies between 3 and 4 for high friction coefficients.

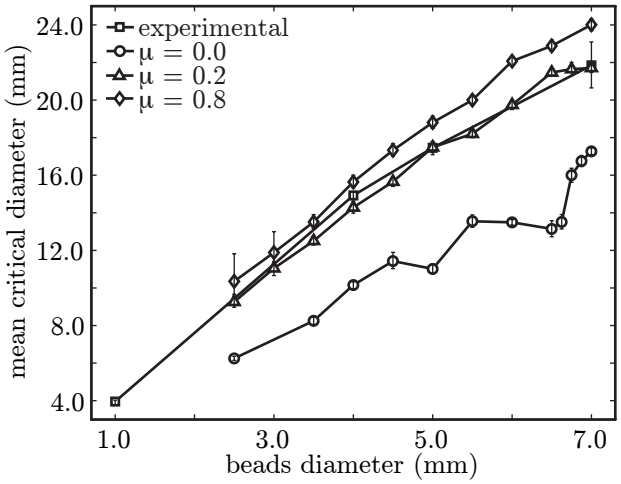


Figure 5.7: Results of experimental and numerical trials for monodisperse assemblies of beads with diameters ranging from 1.0 mm to 7.0 mm and mutual friction coefficients between 0.0 and 0.8.

Those results for monodisperse assemblies of beads will be used as a reference in the next section, where the behavior of bidisperse media will be compared to that of monodiperse ones.

## 5.4 Flowability of bidisperse granular media

While physical monodisperse experiments are easy to carry out, bidisperse ones turn out to be a lot trickier. Indeed, strong segregation occurs when pouring beads of two distinct diameters into the initial piling of a flowability trial. In the course of the experiment the medium therefore behaves like a succession of monodisperse media. In order to overcome these difficulties, the numerical framework is quite convenient, since the bidisperse pilings obtained with our preparation method are homogeneous, as already discussed above. All our bidisperse trials have therefore been performed numerically. The friction coefficient was kept constant at $\mu = 0.2$.

In the case of monodisperse media, the mean critical diameter can be plotted against the bead's diameters as in figure 5.7. Bidisperse media, though are characterized by two distinct bead diameters $\Phi_1$ and $\Phi_2$ and in order to plot bidisperse results in a similar way as monodisperse ones, we choose to use the mass-average diameter of the beads $\bar{\Phi}$ :

$$\bar{\Phi} = \frac{\Phi_1^4 + \Phi_2^4}{\Phi_1^3 + \Phi_2^3} \tag{5.1}$$

Observe that expression (5.1) is valid under the assumption that all beads have the same densities, which is the case here. Measures of the mean critical diameter have been performed for bead assemblies with mass-average diameters $\bar{\Phi}$ ranging from 3.0 mm to 6.0 mm. The resulting mean critical diameters are plotted against $\bar{\Phi}$ on figure 5.8 together with the monodisperse results obtained with $\mu = 0.2$.

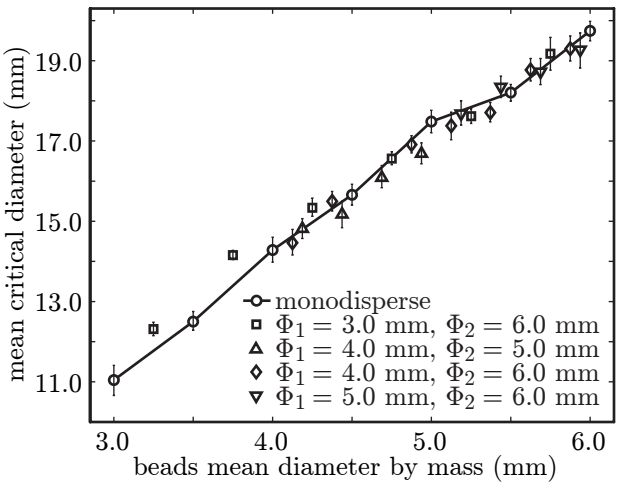


Figure 5.8: The mean critical diameters of monodisperse and bidisperse bead assemblies with $\mu = 0.2$ and $\bar{\Phi}$ ranging from 3 mm to 6 mm.

In this representation, bidisperse measures collapse on the monodisperse curve with very good accuracy. This observation has to be slightly relativized though, for bidisperse media with $\Phi_1$ significantly smaller than $\Phi_2$, yet close enough to $\bar{\Phi}$. In those cases, the mean critical diameters are statistically greater for bidisperse media than

for monodisperse ones. This can be explained in terms of segregation. Indeed, such granular assemblies feature a small number of large beads that are significantly larger than the others. This leads to a strong tendency to segregate. Large beads actually migrate to the top and remain there while small beads flow through the hole. When the large beads finally reach the hole, most of the time they gather in an arch such as those shown in figure 5.9.

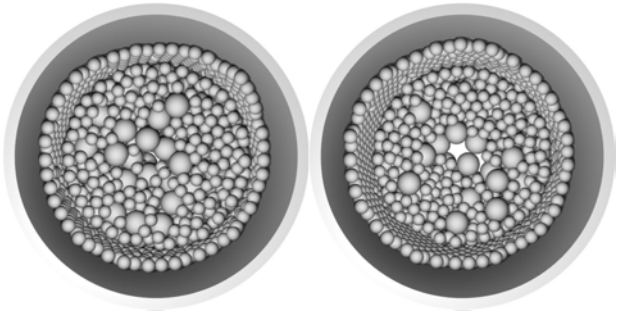

Figure 5.9: Top view of two arches involving mostly big beads that segregated during the flow.

Apart from this, bidisperse and monodisperse results fit very well. Moreover, one may observe that two bidisperse media with same $\bar{\Phi}$ but different diameters for their constituting beads will have the same mean critical diameter. Those observations lead us to formulate the following tentative law : *for fixed interparticulate friction, mean critical diameters of homogeneous bidisperse bead assemblies only depend on their mass-average diameters*.

For low friction coefficients, the dependence of flowability on the diameter of the beads is more erratic than for high frictions (figure 5.7). A further question is the validity of the above law for such frictions, which would allow to decide whether it is intrinsic to bead assemblies or only a linear dependance between the set of involved bead diameters. Figure 5.10 reports results of either monodisperse and bidisperse tries obtained with $\mu = 0.0$ and $\bar{\Phi}$ ranging from 5.0 mm to 7.0 mm. Observe that the monodisperse curve is strongly increasing for $\Phi < 5.5$ and $\Phi > 6.5$ and approximately constant in between. One can see that bidisperse results collapse well on this highly non-linear curve, which further validates our flowability law.

Observe that this law was checked for bidisperse and monodisperse bead sets with $\mu = 0.0$ and $\mu = 0.2$. Polydisperse media with wider ranges of diameters still have to be investigated, though.

## 5.5 Conclusions

By performing both experimental and numerical trials, we have shown that distinct element methods are appropriate to evaluate the flowability of monodisperse bead assemblies. Once again, this suggests that those numerical models successfully capture the behavior of statical granular media. It has also been observed that the dependence

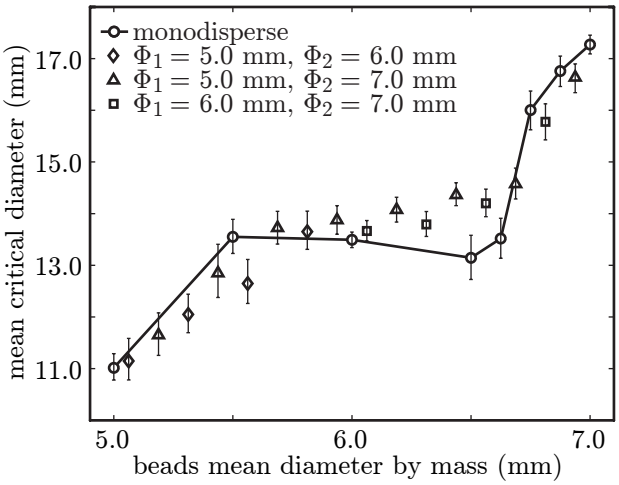


Figure 5.10: The mean critical diameters of monodisperse and bidisperse bead assemblies with $\mu = 0.0$ and $\bar{\Phi}$ ranging from 5 mm to 7 mm.

of flowability on friction decreases with increasing friction coefficients. Then, numerical trials suggested that the flowability of homogeneous bidisperse bead assemblies only depend on their mass-average diameters, leading to the formulation of a law. Further work include the validation of this law on bead assemblies with higher polydispersity, using a wider range of friction coefficients.

# Chapter 6

# Spherocylinder Crystallization

For our first numerical experiments with non-spherical particles, we use spherocylinders, and shake them in a cylindrical container. As a result, we observe them crystallize vertically and faithfully reproduce the corresponding results of physical experiments from the literature [VLMJ00].

We discuss the mechanisms underlying to this phenomenon that recalls of a crystalline growth germinating about the boundaries of the container. Note that while this crystallization is catalyzed by the boundaries in our setup, there actually are several causes for this phenomenon. It has been suggested [BNK03; RPL05b] that the void-filling process is another mechanism leading to spherocylinder crystallization. Moreover, it has been shown [RPL05b] that vertical ordering also happens without the influence of walls.

## 6.1 The Experiments

We simulate the rearrangement of mono-disperse populations of spherocylinders enclosed within a cylindrical container subject to vertical tapping. In order to do this, we use a cylindrical container of base diameter $D$, which is sufficiently high so that the particles cannot escape from it. Its base is mobile and can be subject to a 30 Hz sinusoidal vertical oscillation whose amplitude $a$ can be chosen, whereas its vertical wall remains motionless. The grains used for the rearrangement are spherocylinders of diameter $\delta$ and elongation parameter $\phi = \lambda/\delta$. Population size is $N_p$. Simulation processes are initialized by randomly placing the particles within the cylinder, the directions of their shafts being uniformly distributed, and letting them settle under the action of gravity. Once the kinetic energy has dropped to zero, we start the vibrations. We monitor the intensity of the vibrations via the ratio $\Gamma = \frac{a(2\pi\nu)^2}{g}$, that is the maximal acceleration brought by the bottom plane to the granular packing. Individual grains have density $\rho$ and we further define the medium's volumetric density $\rho_m$ as the ratio of the total volume occupied by the grains divided by the volume of the enclosing

truncated cylinder (upon elimination of outliers). In order to capture the reordering behavior as a function of the height of the enclosing cylinder, the latter is subdivided into four horizontal layers of equal thickness $h = 4$ mm, numbered in increasing order from bottom to top. In other words, layer $i$ is lying between heights $(i-1).h$ and $i.h$.

We monitor the behavior of the medium in terms of the mean angle between the grain shafts and the bottom plane as well as its volumetric density $\rho_m$, both globally and layer by layer. Experiments $an_3, ..., an_9$ were designed to investigate the way elongated grains rearrange, and in particular to observe possible re-orderings which would recall a phase transition. Among those seven experiments, the main one is $an_6$. Experiment $an_9$ involves shorter grains in order to show how the elongation parameter $\phi$ changes the rearrangement behavior. In this experiment, the number of grains is chosen so that the initial filling height is closest possible to that of $an_6$. The other five experiments were carried out to investigate possible influence of the restitution coefficient $e_n$ and the vibration intensity $\Gamma$ on the results.

The parameter values for the various simulations we carried out are given in table 6.1

| | $\Delta t$ (s) | $t_c$ (s) | $e_n$ | $\Gamma$ | $\phi$ | $\delta$ (m) | $D$ (m) | $N_p$ |
|---|---|---|---|---|---|---|---|---|
| $an_3$ | $2 \times 10^{-5}$ | $6 \times 10^{-4}$ | 0.1 | 2.0 | 4.00 | $0.523 \times 10^{-3}$ | $8 \times 10^{-3}$ | 1000 |
| $an_4$ | $2 \times 10^{-5}$ | $6 \times 10^{-4}$ | 0.2 | 2.0 | 4.00 | $0.523 \times 10^{-3}$ | $8 \times 10^{-3}$ | 1000 |
| $an_5$ | $2 \times 10^{-5}$ | $6 \times 10^{-4}$ | 0.4 | 1.5 | 4.00 | $0.523 \times 10^{-3}$ | $8 \times 10^{-3}$ | 1000 |
| $an_6$ | $2 \times 10^{-5}$ | $6 \times 10^{-4}$ | 0.4 | 2.0 | 4.00 | $0.523 \times 10^{-3}$ | $8 \times 10^{-3}$ | 1000 |
| $an_7$ | $2 \times 10^{-5}$ | $6 \times 10^{-4}$ | 0.4 | 2.5 | 4.00 | $0.523 \times 10^{-3}$ | $8 \times 10^{-3}$ | 1000 |
| $an_8$ | $2 \times 10^{-5}$ | $6 \times 10^{-4}$ | 0.8 | 2.0 | 4.00 | $0.523 \times 10^{-3}$ | $8 \times 10^{-3}$ | 1000 |
| $an_9$ | $2 \times 10^{-5}$ | $6 \times 10^{-4}$ | 0.4 | 2.0 | 2.83 | $0.523 \times 10^{-3}$ | $8 \times 10^{-3}$ | 1414 |

Table 6.1: Experiments of vibrating mono-disperse media

## 6.2 Crystallization mechanisms

Lateral snapshots of experiment $an_6$ at various evolution stages are given in figure 6.1. In a qualitative way, we see that the spherocylinders rearrange vertically to a highly ordered state, at least along the cylinder boundary. The cuts of the cylinder with a plane through its axis shown in figure 6.1 further show that this particular rearrangement also occurs in the middle of the container. Obviously the concurring shapes and sizes of both container and grains play a decisive role on crystallization processes. In particular, this is why the spherocylinders tend to crystallize vertically, achieving a high volumetric density. The final arrangements reported in [ATC03] for Metropolis-Monte-Carlo simulations of spherocylindric populations are not crystalline. For obvious reasons one can not draw any conclusions about the dynamic behavior of real grain rearrangements from the Monte-Carlo process. Furthermore, the final density attained in [ATC03] corresponds to a metastable state of significantly lower volumetric density than that of the crystallized medium. This does not come as a surprise since such a metastable state is very hard to escape, the crystallization process certainly having a

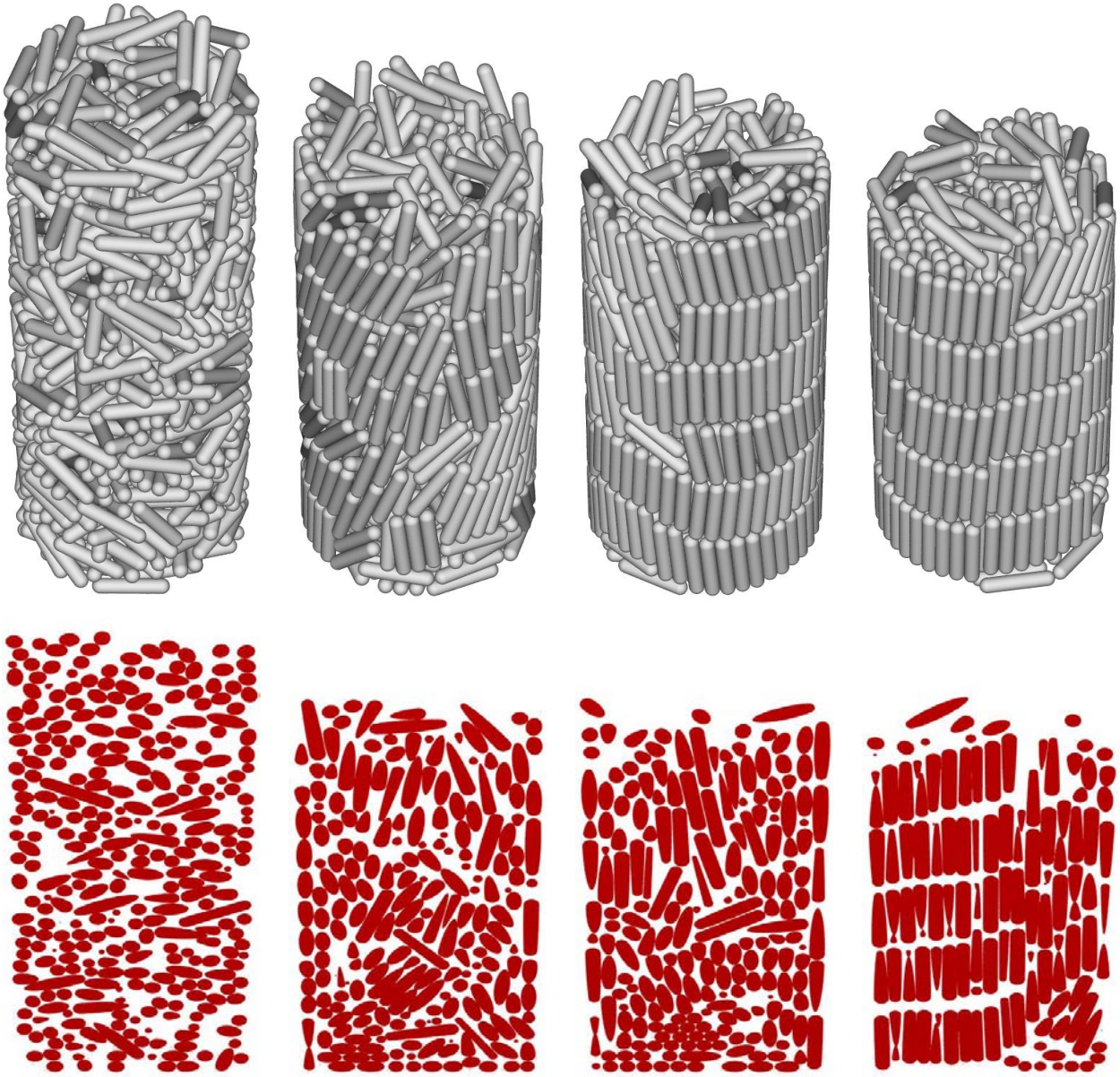

Figure 6.1: Snapshots and cuts of experiment $an_6$. Upper line : lateral snapshots. Lower line : corresponding cuts by a vertical plane containing the cylinder axis. From left to right : initial situation, after 300 tapping steps, after 900 tapping steps, after 4134 tapping steps

logarithmic behavior also in the Metropolis-Monte-Carlo simulations. The transformations in that model only allowing for rearrangements of individual grains one at a time, crystallization becomes extremely unlikely. Moreover, many of the experiments in [ATC03] are carried out on the periodic boundary conditions, hence there are no crystalline nucleation sites, which further slows down crystallization.

We measured the volumetric density $\rho_m$ of the considered medium. The inset in Figure 6.3 shows its graph against the number of tapping steps. As can be seen, the density

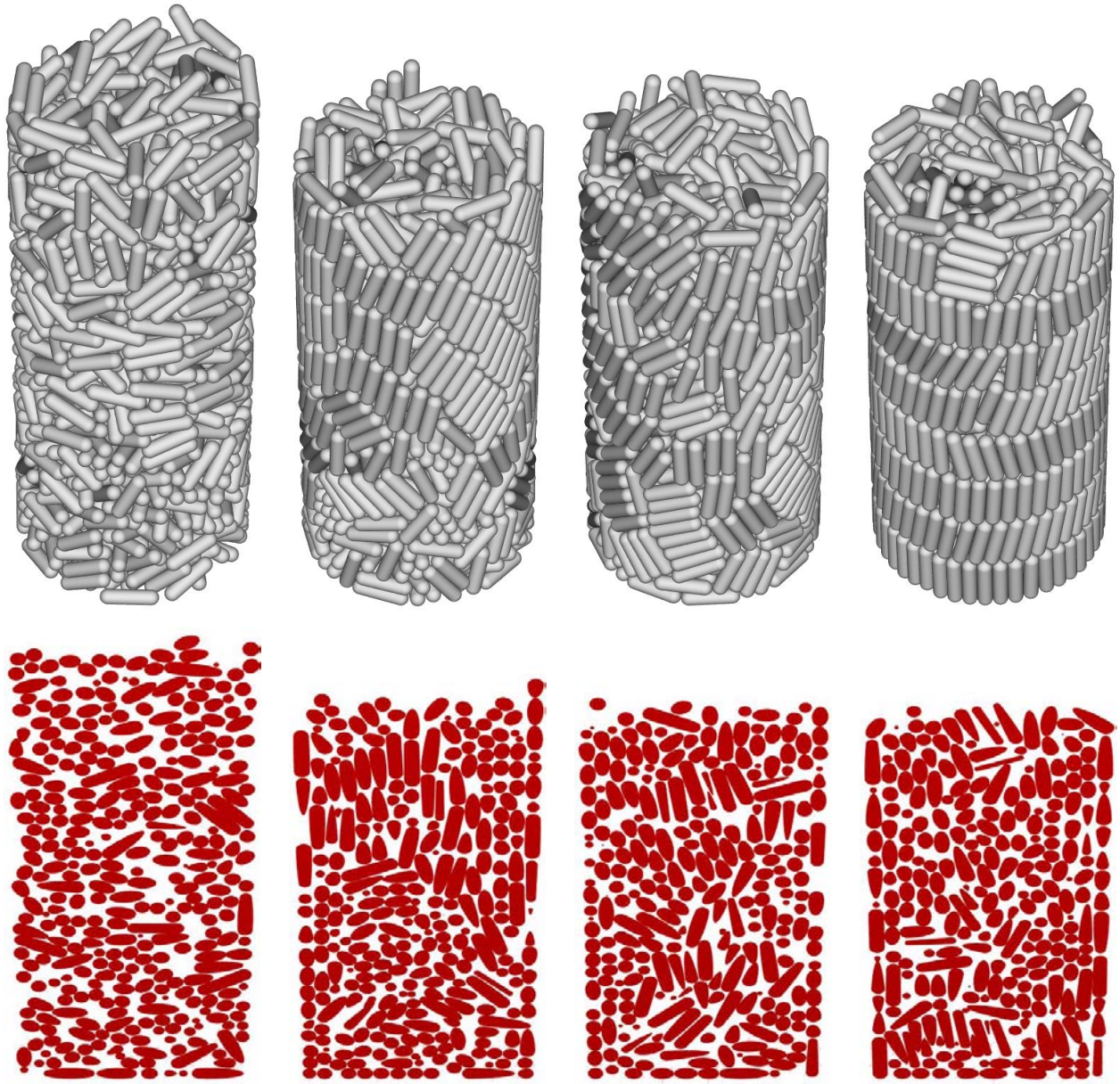

Figure 6.2: Snapshots and cuts of experiment $an_9$. Upper line : lateral snapshots. Lower line : corresponding cuts by a vertical plane containing the cylinder axis. From left to right : initial situation, after 300 tapping steps, after 900 tapping steps, after 4134 tapping steps

plot shows quite strong oscillations which can be explained by the effect of the sinusoidal tapping, the overall medium behaving like an elastic spring. In order to filter out this effect we smoothen the curve with a moving average as shown on the inset of Figure 6.3 for experiment $an_6$. The smoothed version of the volumetric density $\rho_m$ is given in figure 6.3 for the whole set of experiments.

In figure 6.4 we plot the mean angle between the grain shafts and the bottom plane against the number of tapping steps. Figure 6.5 depicts the mean angle within several

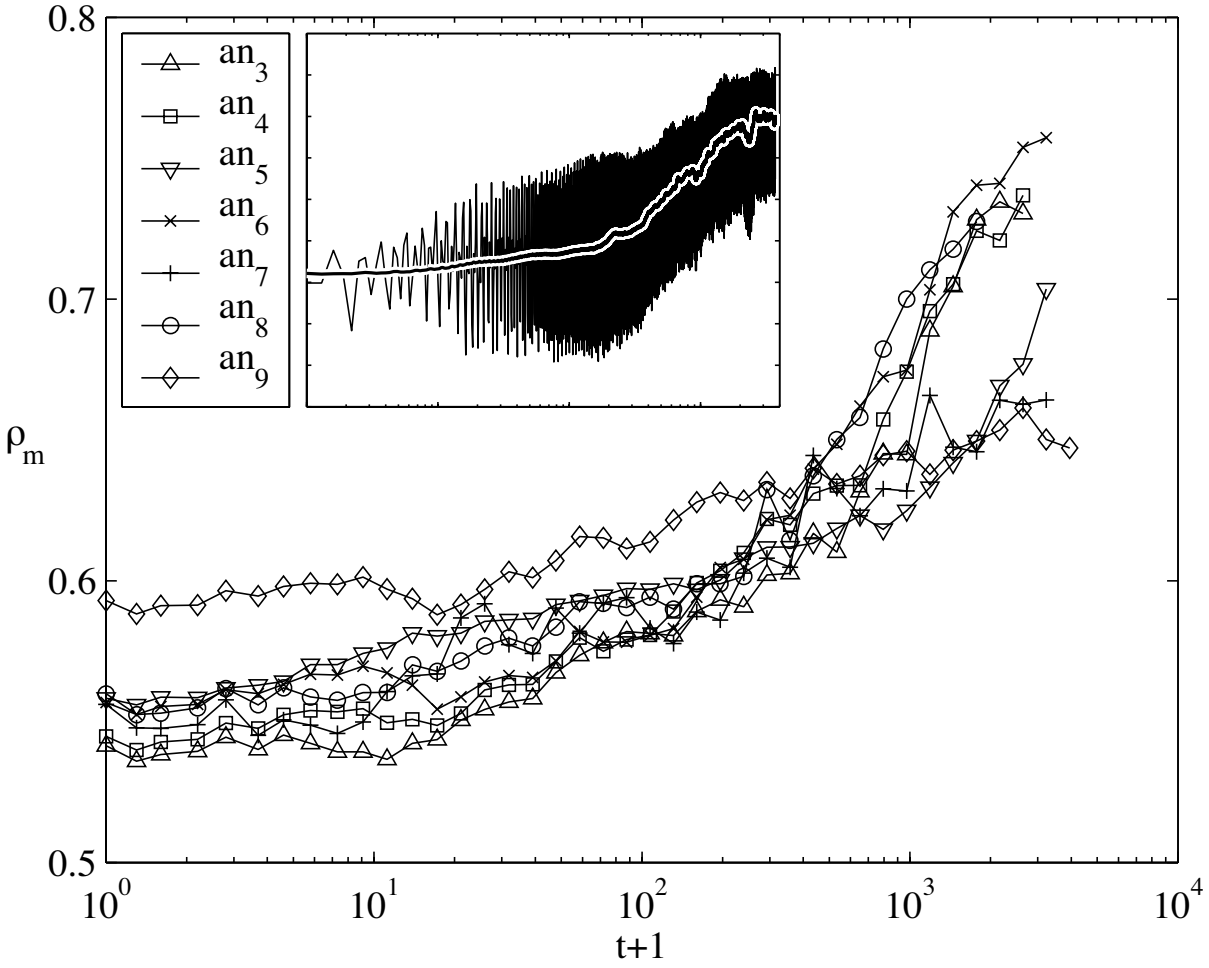


Figure 6.3: Smoothed density $\rho_m$ plotted versus the number of tapping steps $t$ for experiments $an_3$-$an_9$. Inset : oscillations of the measured density and its moving average smoothed version for experiment $an_6$

horizontal subdivisions of the container. The mean angle does not show the same oscillatory behavior as the volumetric density. A possible explanation might be that during a tapping oscillation, the angle variations tend to average out. We see that the beginning of a phase transition with respect to the angle takes place at approximately constant density (between 10 and 100 tapings). Observe that the crystallization process as measured by the volumetric density starts after about 100 tapping steps, behaving logarithmically from there on until it reaches a value of $\rho_m = 0.75$ for the highest after about 2000 tapings. This value is not very far from the maximum possible density of tightly packed spherocylinders in an unbounded three-dimensional space, which equals $\rho_m^{\max} = \frac{\pi}{6}\frac{3\phi+2}{\sqrt{3\phi+\sqrt{2}}}$, that is $\rho_m^{\max} = 0.8787$ when $\phi = 4.0$.

Measured by the mean angle, the crystallization process starts after 10 tapings already and behaves logarithmically until it saturates after approximately 1000 tapings for experiments $an_3$, $an_5$ and $an_9$. Experiments $an_3$ and $an_5$ do not show a logarithmic behavior during the re-ordering process. The restitution coefficient used in experiment $an_3$ is much lower than that used in the other experiments. This causes the energy reaching

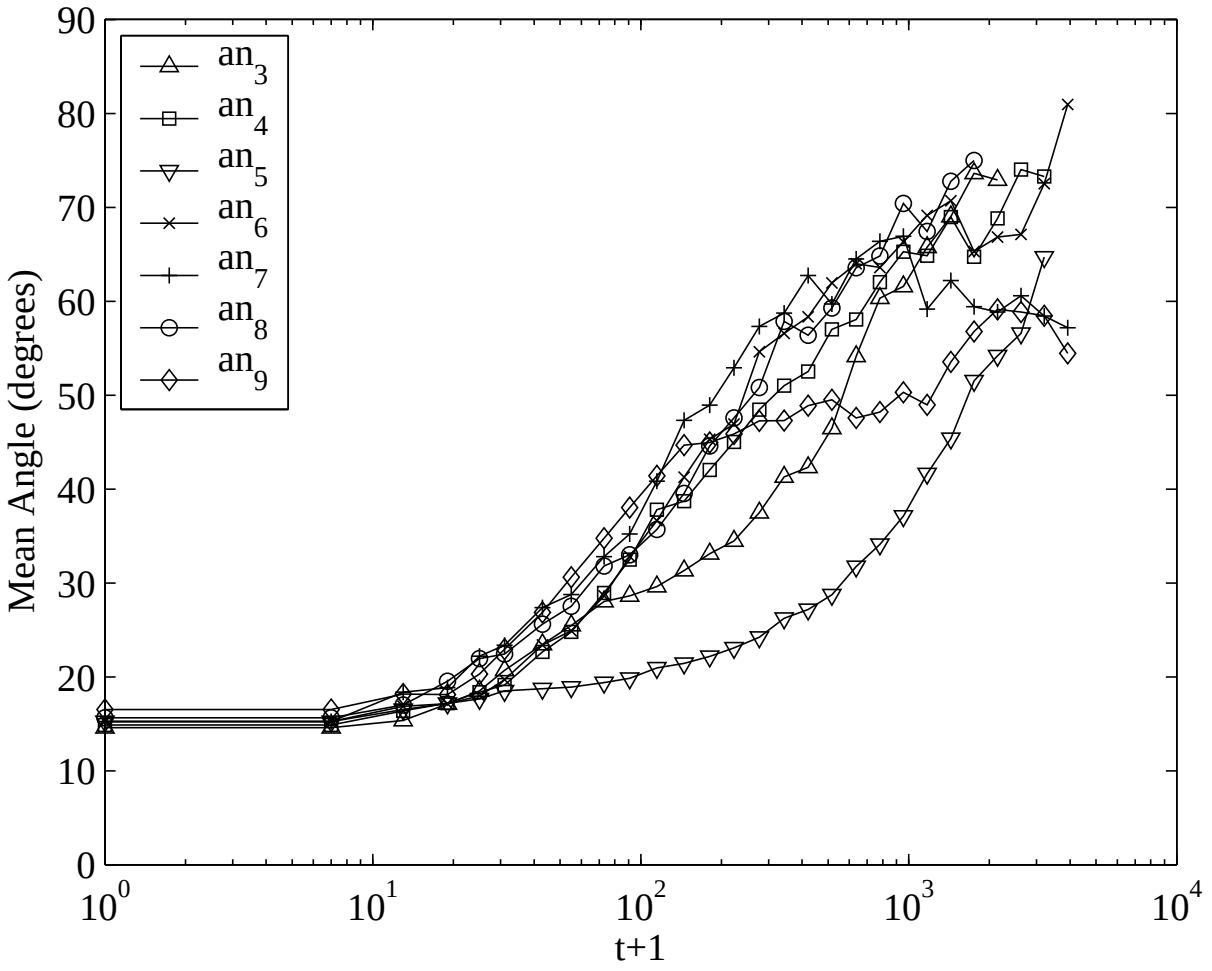


Figure 6.4: Mean angle between the particles shafts and the bottom plane versus the number $t$ of tapping steps for several experiments

the grains to be small, which limits their motion. However, we see no dependence on $e_n$ for $e_n \geq 0.2$ (experiments $an_4$, $an_6$, $an_8$). This would mean that in experiment $an_3$ the energy available to the system is too small for it to reach the dynamical regime found in experiments $an_4$, $an_6$ and $an_8$. For experiment $an_5$, the value of $\Gamma$ is pretty low, which means that little energy is brought to the system. In this case also, the other experiments ($an_6$, $an_7$) show there is no dependence on $\Gamma$ for $\Gamma \geq 2.0$. Again, this suggests that the energy available to the system is not sufficient to reach the dynamics of experiments $an_4$, $an_6$ and $an_8$. While experiment $an_9$ exhibits the same logarithmic re-ordering as experiments $an_4$, $an_6$, $an_7$ and $an_8$, figure 6.4 shows that this logarithmic part is shorter and that the saturation takes place at a lower value of the mean angle. This shows that while the dynamics of the re-ordering seems not to be dependent of the elongation parameter, the saturation process is. It might be that with small values of $\Phi$, the grains have more freedom to arrange in a disordered state, and the transition to a crystalline ordering is less probable.

Another possibility is that the cylinder shape has less influence on short grains than on long ones. Indeed when a slanted particle touches a cylindrical wall at two points,

a torque develops that tends to erect it. The magnitude of this torque increases with particle lenght. It can be observed that the logarithmic stage of reordering is mainly due to global rearrangement processes (convection), whereas the saturation stage is ruled by local rearrangements. The logarithmic rearrangement behavior corresponds to that observed for media composed of identical spherical grains.

Figure 6.5 shows that excepting top and bottom layers, the mean angle increases monotonically to eventually stay between 80 and 90 degrees for experiments $an_3$, $an_4$, $an_6$, $an_8$ and between 60 and 80 degrees for experiments $an_5$, $an_7$, and $an_9$. This means that the crystallization does not only occur along the container wall but involves all grains in those layers. Figure 6.5 also shows that in the logarithmic re-ordering stage, layers seem to reorder from the top to the bottom as the mean angle in a layer is always lower than that of the higher layers. In the saturation stage, this behavior inverts for the two central layers while the mean angle still increases in the lowest layer and drops in the topmost layer as it gradually empties. Again, this suggests that the nature of rearrangement processes in the logarithmic and saturation phases is not the same, the former being essentially due to global phenomena and the latter involving local rearrangements in a mostly static medium. This behavior matches that observed in [VLMJ00] on experiments with real elongated grains. Quantitatively, the dynamics of our simulated media fits well that reported there. In particular, the time slots for both reordering processes match. The reordering is logarithmic in both cases, and the initial and final volumetric densities also agree.

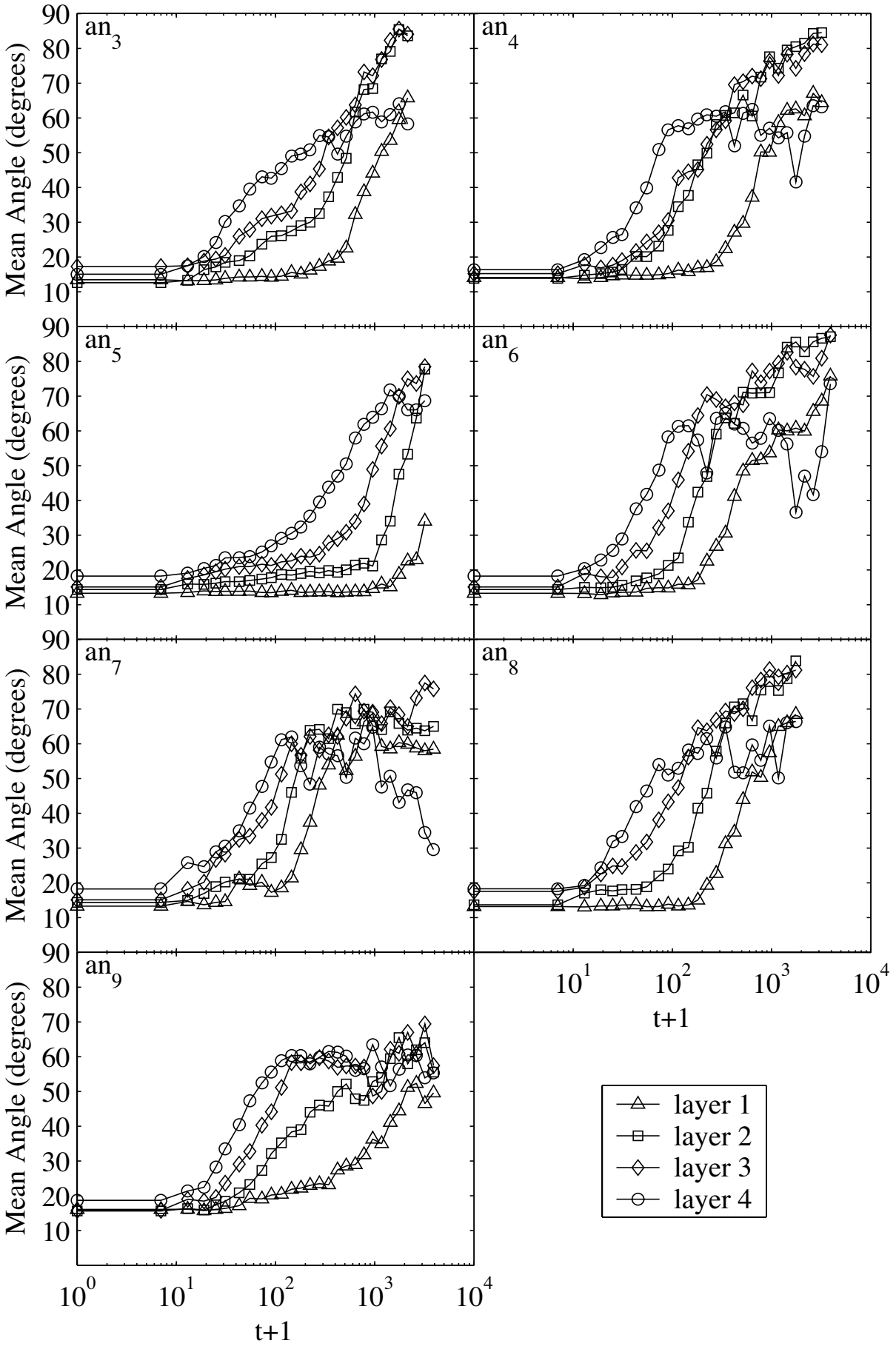


Figure 6.5: Mean angle between particle shafts and the bottom plane plotted versus the number of tapping steps $t$ in four horizontal layers. Layers are numbered in increasing order from bottom to top and their thickness is $h = 4$ mm, that is layer $i$ is lying between heights $(i-1).h$ and $i.h$.

# Chapter 7

# On the segregation of spheres and tetrahedra

Granular media can behave like solids, liquids and also gas depending on the conditions they are submitted to. Some of their behaviors though, cannot be classified in any of these three states of matter. Granular segregation, also known as *Brazil nut effect* belongs to this range of behavior that escapes usual classifications. The Brazil nut effect is observed in particular when particles of different sizes are shaken. Particles with same sizes will gather, producing size inhomogeneities that contradict the intuition whereby diffusion should occur. It was first observed that large particles would migrate upwards under vibrations [MLNJ01; KJN93; DRC93; RSPS87]. Particle density was found to play a role too, though less important than particle size in segregation phenomena [SM98] as well as interstitial gas [RTLM03; NSK03]. The Brazil nut effect also occurs in a reverse way, large particles migrating to the bottom of the mixture [Shi04; BEKR03; HQL01]. Recently the phenomenon of size segregation was addressed [RPL05a; ATC03; Mak97]. Particles with same mass and volume, but with different shapes were found to segregate. Up to now, these studies were mostly conducted on mixtures of spheres and spherocylinders [RPL05a; ATC03]. Experimental trials have shown that DEM simulations were able to capture this behavior [RPL05a].

In general, particles that differ in size, density, shape or other materials properties will most of the time tend to segregate under dynamical regimes like vibration. While mixing particles with different properties is needed for many industrial applications, spontaneous homogenization will not take place, except under very special conditions [RPL05a; ATC03].

Thus, it is interesting to study granular segregation in mixtures involving more complicated shapes. This chapter addresses granular segregation of mixtures of spheres and regular spherotetrahedra submitted to vertical vibrations.

## 7.1 The experiments

The first set of experiments takes place in a cylindrical container of diameter $D = 8$ mm. The base of this container is mobile and can be subject to a 30 Hz sinusoidal vertical oscillation whose amplitude $a$ can be chosen. The vertical walls remain motionless. The intensity of the vibrations is monitored using the maximal acceleration $\Gamma$ brought by the bottom disc to the medium:

$$\Gamma = \frac{a(2\pi\nu)^2}{g}. \tag{7.1}$$

We use spheres with diameter 1 mm and density 1910 kg.m$^{-3}$ and regular spherotetrahedra of same volume and density whose sphericity ratio is $l/r = 0.616$, where $r$ is the radius of a particle and $l$ is the distance between its mass center and any vertex of its skeleton. In each simulation, 250 spheres and 250 spherotetrahedra are poured in the container. The spheres can either be poured on top of the spherotetrahedra (sph↑) or inversely (tet↑) which produces initially unmixed states. Of course one can choose to pour the two species together in order to produce a mixed initial state. Once a mechanical equilibrium is reached, the vibrations begin.

The behavior of the medium is monitored in terms of the ratio $R$ between the height $h_t$ of the mass center of the spherotetrahedra and the height $h_s$ of the mass center of the spheres. For the simulations we chose a friction coefficient of $\mu = 0.2$, a restitution coefficient of $e_n = 0.4$, a contact time of $t_c = 6\,10^{-4}$ s and a time step of $\Delta t = 2\,10^{-5}$ s for the integration of the motion equations.

A second set of experiments is performed under periodic boundary condition affecting the two directions orthogonal to gravitation. The period $p$ is equal in both directions and chosen so that the basis surface of the periodic square is equal to the basis surface of the cylindrical container. A simple calculation provides $p = 7.09$ mm. Table 7.1 shows the parameter values for the various simulations we carried out.

| exp. | $\Gamma$ | initial mix. | boundaries |
|---|---|---|---|
| 1 | 2.0 | sph↑ | periodic |
| 2 | 2.0 | tet↑ | periodic |
| 3 | 2.0 | mixed | periodic |
| 4 | 2.0 | sph↑ | cylinder |
| 5 | 2.0 | tet↑ | cylinder |
| 6 | 2.0 | mixed | cylinder |
| 1 | 3.0 | sph↑ | periodic |
| 2 | 3.0 | tet↑ | periodic |
| 3 | 3.0 | mixed | periodic |
| 4 | 3.0 | sph↑ | cylinder |
| 5 | 3.0 | tet↑ | cylinder |
| 6 | 3.0 | mixed | cylinder |

Table 7.1: Experiments of vibrating mixtures of spheres and spherotetrahedra.

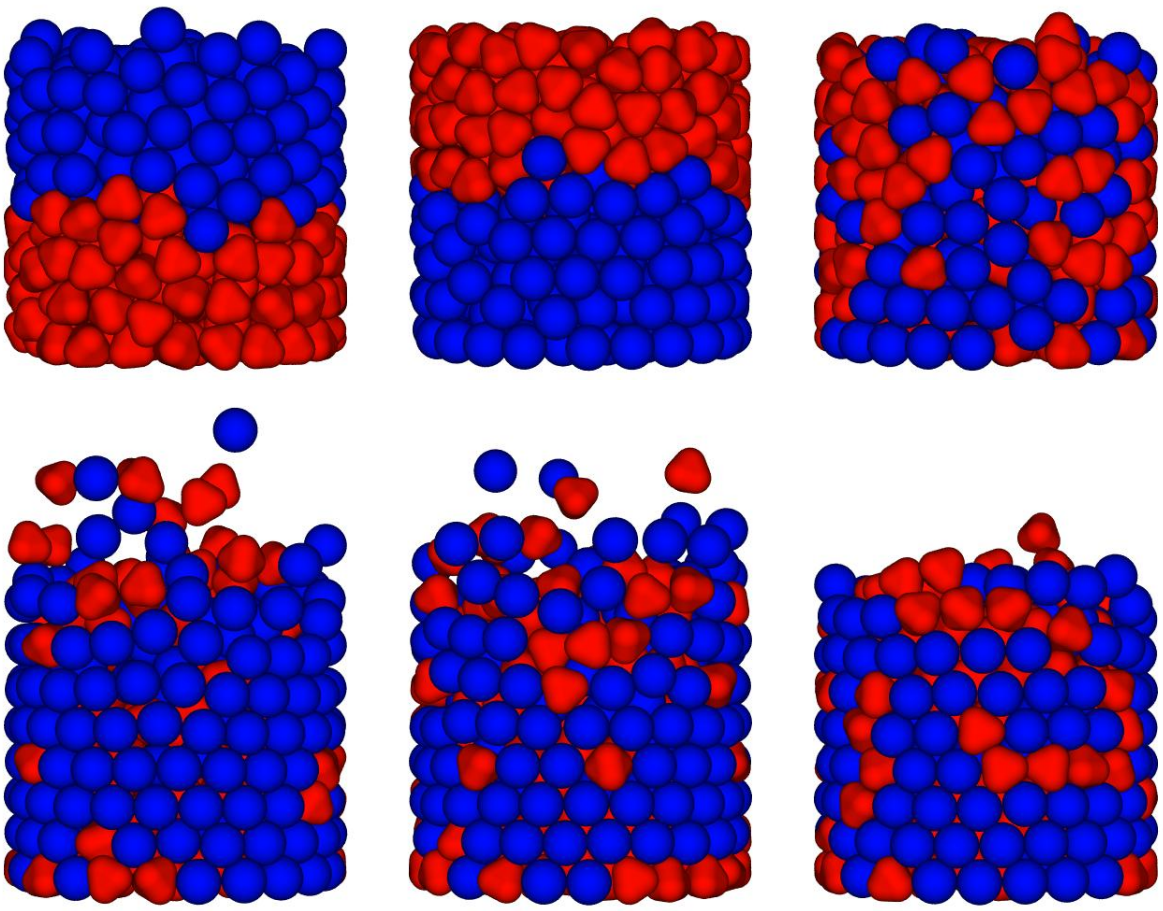

Figure 7.1: . Lateral Snapshots of the initial (top row) and final (bottom row) situations for experiments 4, 5 and 6 (from left to right).

## 7.2 Results and discussion

Figure 7.2 shows the ratio $R$ drawn against time for experiments 4, 5 and 6. One can see that the initially homogeneously mixed state (experiment 6) does not segregate. As a possible cause for this, one could invoke the intensity of the vibrations which is not sufficient to produce rearrangements. It is clear, however, that the initially unmixed states (experiments 4 and 5) are unstable under those vibrations, meaning that the rearrangements actually occur with this acceleration. Moreover, those rearrangements tend to mix spheres and spherotetrahedra.

Looking at figure 7.3, one can see that at the end of the experiments, most of the particles about the cylinder boundary are spheres. This suggests that segregation indeed occurs with mixtures of spheres and spherotetrahedra but in a radial way. Indeed, figure 7.3 shows the proportion $P$ of spheres among all the particles whose centers are at a distance less than $l + r$ of the boundary. The proportion $P$ of spheres reaches 0.8

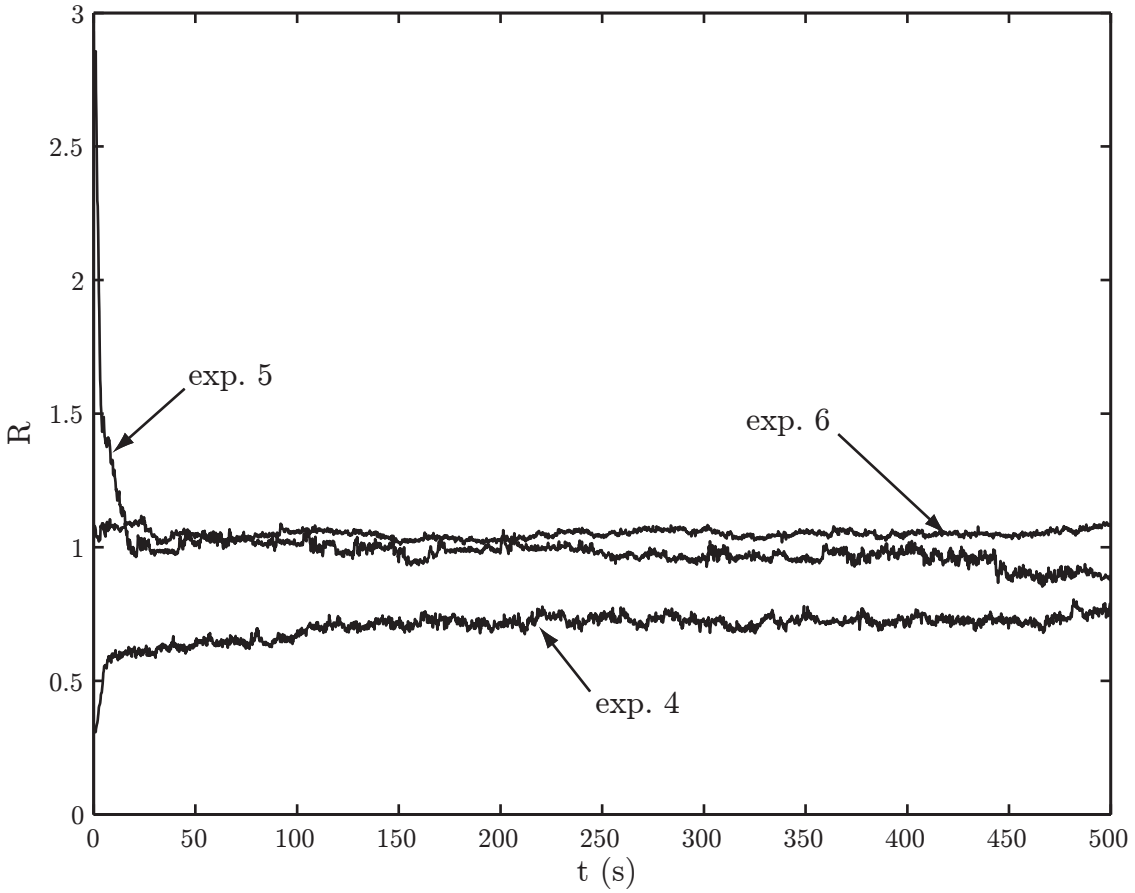


Figure 7.2: . The ratio $R$ drawn against time for experiments 4 (sph↑), 5 (tet↑) and 6 (initially mixed) carried out with cylindrical boundaries and $\Gamma = 2.0$.

meaning that segregation occurs radially. Intuition suggests that this may be due to the curvature of the spheres which is closer to that of the cylinder than the curvature of spherotetrahedra.

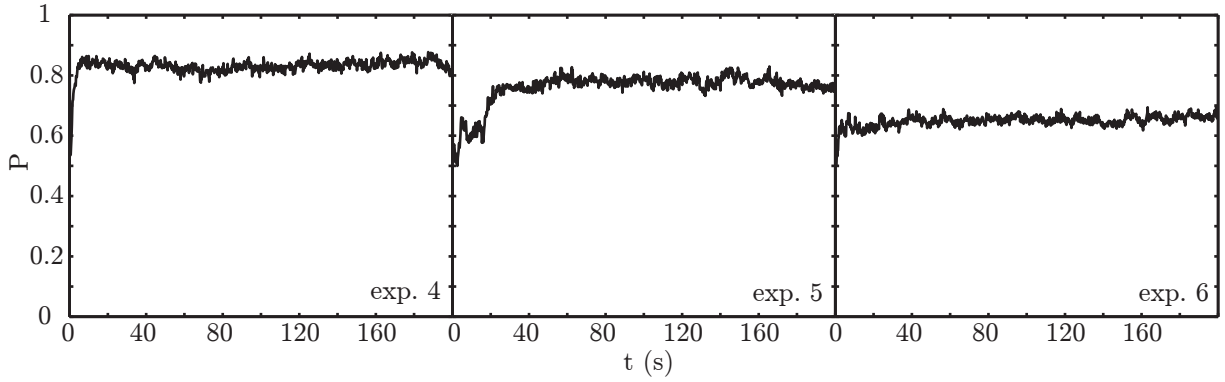


Figure 7.3: . The proportion $P$ of sphere about the boundary for experiments 4 (sph↑), 5 (tet↑) and 6 (initially mixed) carried out with $\Gamma = 2.0$.

Experiments with periodic boundary conditions have the nice property that radial segregation will not occur in such setups. This allows to separate vertical mixing and radial segregation. Figure 7.4 shows the ratio $R$ drawn against time for experiments 1, 2 and 3. As one can see, nothing happens. The initially mixed medium (experiment 3), and the initially unmixed ones (experiments 1 and 2) remain unmixed. One would expect that either mixing or segregation would occur under vibrations. This suggests that our vibrations are not strong enough to allow the medium to rearrange. With periodic boundary conditions there will be no convection. The rearrangements then only rely on the size of the voids created by the agitation of the medium.

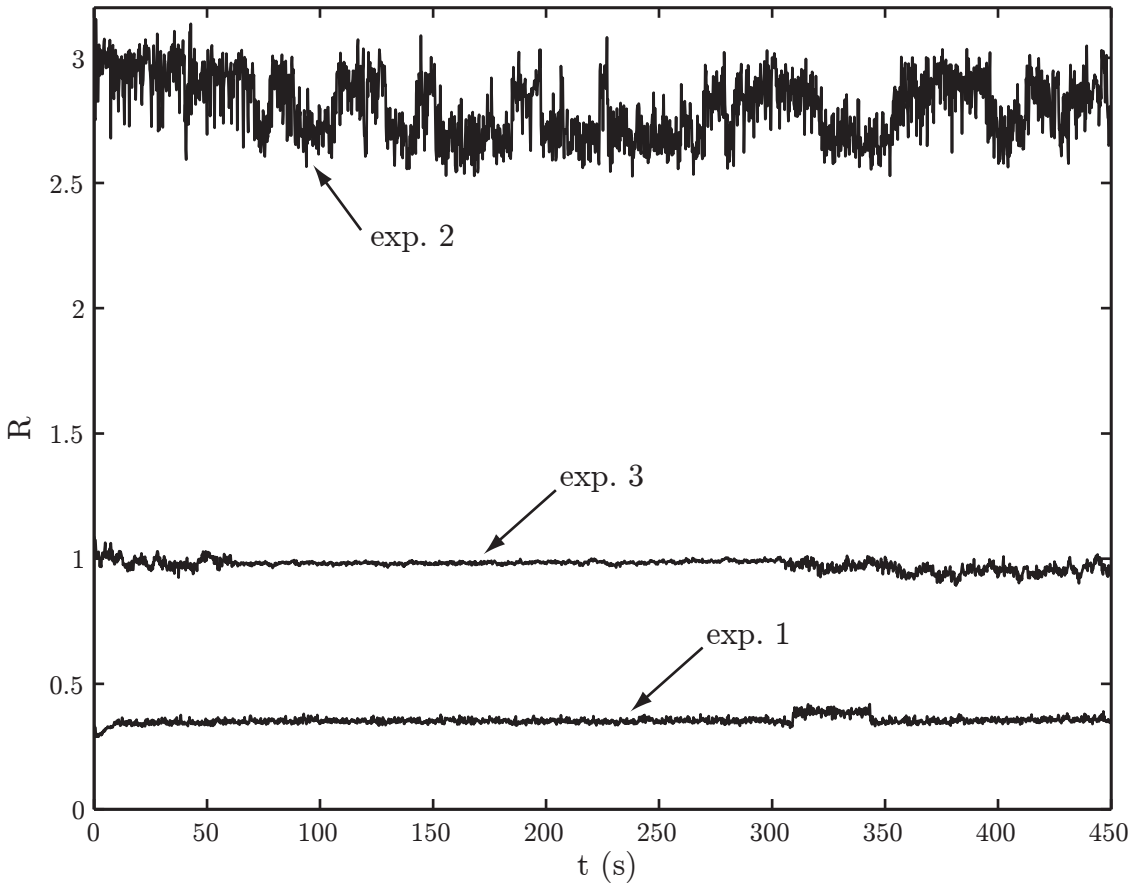


Figure 7.4: . The ratio $R$ drawn against time for experiments 1 (sph↑), 2 (tet↑) and 3 (initially mixed) carried out with periodic boundary conditions and $\Gamma = 2.0$.

The ratio $R$ is drawn against time for experiments 7, 8 and 9 in figure 7.5. Those experiments are identical to experiments 1, 2, and 3 but with $\Gamma = 3.0$ instead of $\Gamma = 2.0$. One can see that the medium not only rearranges but also converges to a final state that is identical in terms of mixing for all three experiments. This means that our spheres and spherotetrahedra have a clear affinity for mixing.

The ratio $R$ is shown in figure 7.6 for experiments 10, 11 and 12 identical to experiments 7, 8 and 9 except that the periodic boundary has been replaced with cylindrical ones. One can see that the grains mix as well. Again, the final situation do not depend on the

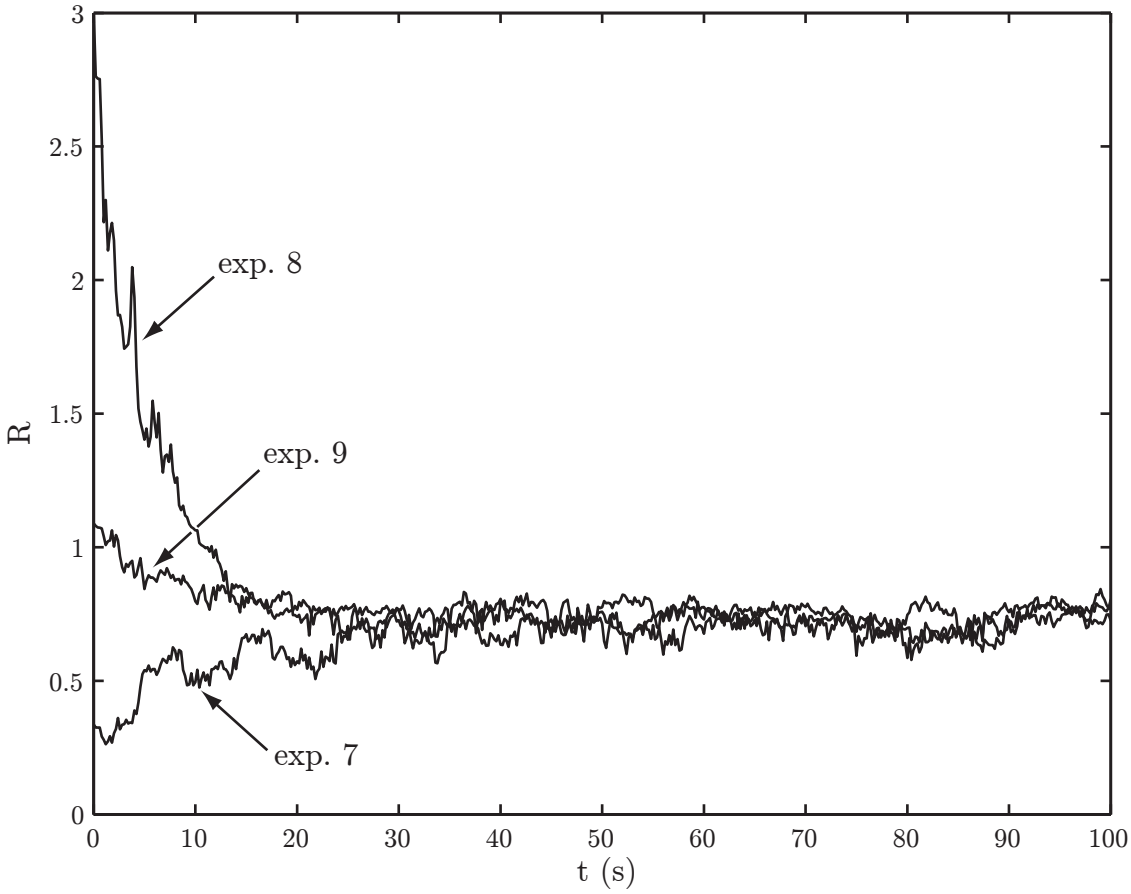


Figure 7.5: . The ratio $R$ drawn against time for experiments 7 (sph↑), 8 (tet↑) and 9 (initially mixed) carried out with periodic boundary conditions and $\Gamma = 3.0$.

initial states. This homogenization is spectacular, since less than five seconds suffice to reach the final mixed state. One sees on figure 7.2 that the homogenization was not as perfect in experiments 4, 5 and 6 as it is in experiments 10, 11 and 12. It seems that with $\Gamma = 2.0$, the agitation is not sufficient for a strong mixing to occur.

One can see that the final mix of experiments 7-12 is obtained with $R$ slightly lower than 1. This means that the average height of spherotetrahedra is lower than that of spheres in the final mixed situation. This may be caused by a greater geometrical affinity of spherotetrahedra with the bottom plane. Indeed spherotetrahedra have flat surfaces corresponding to the facet of their skeletons. Those flat surfaces may lie more easily on the bottom plane than spherical ones, just in the same way spheres gather about cylindrical boundaries in experiments 4, 5 and 6. Figure 7.7 shows the proportion $P$ of spheres about the boundary of the cylinder for experiments 10, 11 and 12. One can see that the radial segregation is dramatically less marked than with lower agitation.

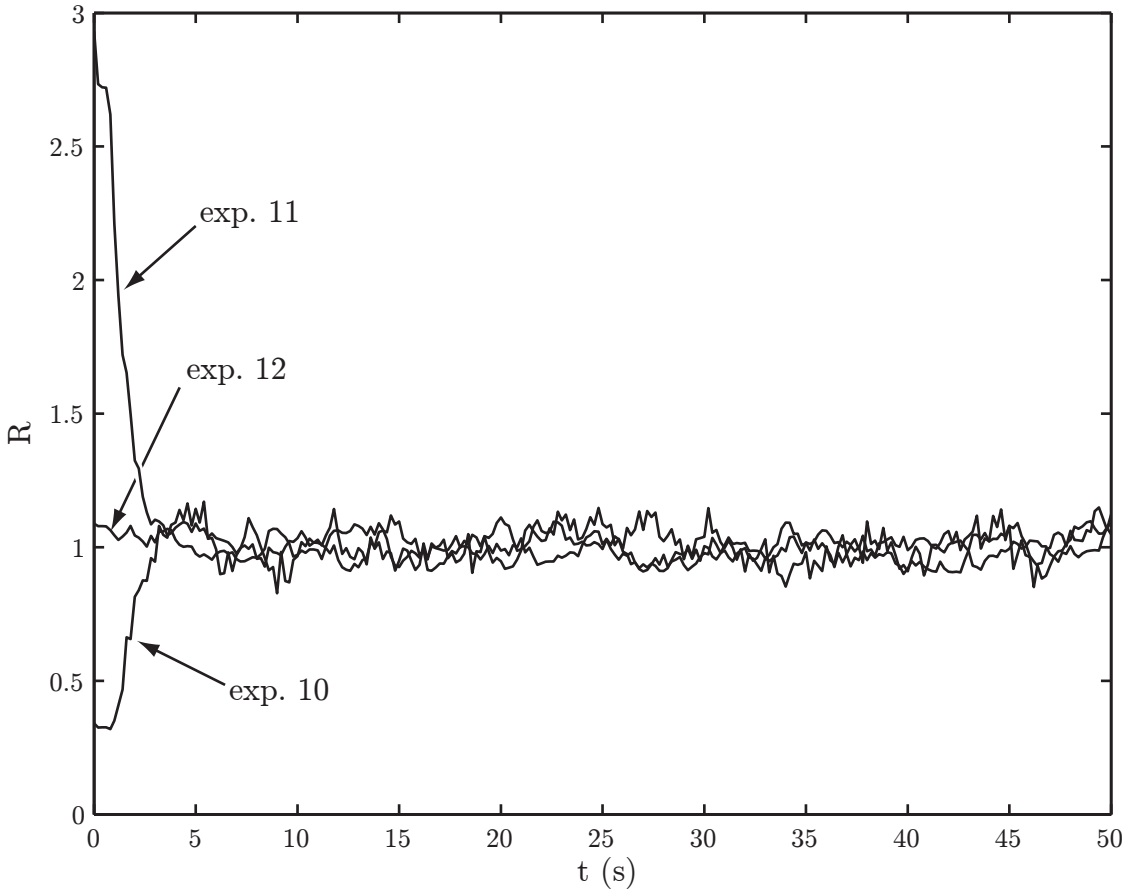


Figure 7.6: . The ratio $R$ drawn against time for experiments 10 (sph↑), 11 (tet↑) and 12 (initially mixed) carried out with cylindrical boundaries and $\Gamma = 3.0$.

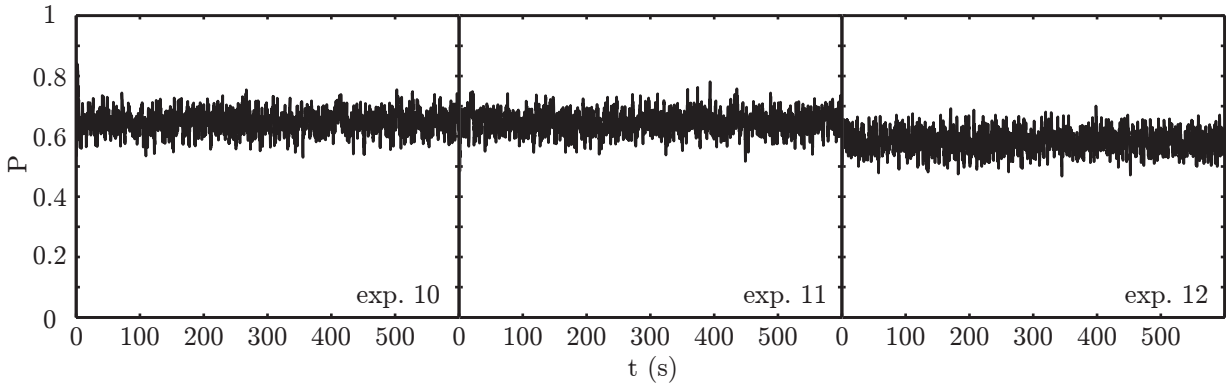


Figure 7.7: . The proportion $P$ of sphere about the boundary for experiments 10 (sph↑), 11 (tet↑) and 12 (initially mixed) carried out with $\Gamma = 3.0$.

## 7.3 Conclusion

We have shown that spheres and spherotetrahedra with same volume and density tend to mix under sufficiently strong vibrations. This constitutes a rather unexpected result since grains with different properties most of the time segregate when submitted to vibrations. Still these conclusions need to be further validated. In particular the sensibility of the process to the sphericity ratio $l/r$ should be investigated as well as the dynamics of the mixing in function of the agitation intensity. We suggest that this mixing behavior may be linked to the fact that the inertia matrix of regular spherotetrahedra is that of a sphere, which has to be validated as well, for example with experiments involving several other shapes (spherocylinders or spherotriangles to begin with). The other interesting effect reported in this chapter is the radial segregation occuring in cylinders. Spheres seem to have a greater affinity with the cylindrical boundaries than spherotetrahedra. This may be due to the curvature of the spheres that is closer to the curvature of the cylinder than that of the spherotetrahedra, which is still to be checked by trying mixtures between particles with different curvatures like spherocylinders and spherotriangles.

# Conclusion

The central result of this thesis is the generalization to non-spherical particles of the simulation techniques developed by D. Müller [ML95; Mül96a] for discs and polygons and J.-A. Ferrez [Fer01; FL02] for spheres. In particular, a description of a wide range of particle shapes was proposed, as well as an extension of molecular dynamics contact models to such particles. The other important issue that was addressed is that of contact detection between bodies with those shapes. A generalization of triangulation-based contact detection methods to non-spherical particles was proposed. The case of convex particle shapes was fully covered, while for non-convex particles a method for tracking contacts between two time steps still needs to be worked out. Finally, three experiments were investigated numerically that provide validations of the numerical model as well as new insights on the behavior of granular media. Below we sum up what has been achieved in each direction addressed in this thesis and propose possible future developments.

The implementation was based on the existing code by J.-A. Ferrez whose evolutionary structure showed to be convenient. The simulation code can now handle mixed populations of spherosimplices using generalized contact models and our linear complexity triangulation-based contact detection method. Developing the code to be able to handle more general spheropolyhedra represents a challenge for future work. This will involve redesigning the simulation environment as well as finding solutions to store such shapes in all their generality.

The contact detection algorithm was mathematically proven to work in a wide range of situations. The particular cases of one covering sphere per particle and that of spherocylinders covered by many spheres were especially addressed. In the former case, detecting contacts between arbitrary shaped bodies or between spheres has the same complexity. In numerical trials, the actual complexity was found to be nearly linear in the number of particles with a slope that increases with particle elongation. This reflects the fact that the number of possible contacts is higher for elongated particles than for round ones.

In addition to the original algorithm 1, the robust regularization algorithm 3 has been implemented that fixes a problem occurring in some practical cases. While the theoretical convergence of this last algorithm is not proven, up to now, no case was ever encountered in practice where the algorithm failed to converge. Hence it might always be the case that changing a non-regular triangulation into a regular one with the same vertex set can be done by only flipping *illegal* facets.

In this thesis it has been shown that the flip-graph of *regular* triangulations that share a same vertex set is connected. The general case that also includes non-regular triangulations in three dimensions remains open, though. The behavior of our regularization algorithm may point to a direction for further investigating the connectivity of the flip-graph in three dimensions.

With the help of the simulation code, several phenomena concerning various forms of behavior of granular media were studied. A first experiment about the flowability of bead assemblies was performed both with real-world setups and numerical simulation. The results of those trials indicate that the distinct element method is appropriate to measure the flowability of monodisperse bead assemblies, thus that the proposed numerical models successfully capture the behavior of statical granular media. The dependence of flowability on friction was investigated and found to decrease with increasing friction coefficients. Finally, according to numerical trials, the flowability of homogeneous bidisperse bead assemblies was found to depend only on their mass-average diameters. It is expected that future work on the influence of particle shape on flowability using our tools will disclose interesting features.

The second set of experiments was carried out with spherocylinders. Monodisperse assemblies of such particles were vibrated vertically inside a cylindrical container. A vertical reordering recalling a crystallization was observed that agrees with experimental observations. The reasons for this behavior have been discussed and while our cylindrical boundaries probably play an important role, it is however very likely that other causes are also responsible for this verticalization phenomenon.

The last set of experiments was designed to investigate the shape segregation in mixtures of spheres and spherotetrahedra with same volume and density. Such mixtures were vibrated in cylindrical containers and also with periodic boundary conditions. With cylindrical boundaries, radial segregation was found to occur while unexpectedly, no vertical segregation was observed neither with cylindrical containers, nor with periodic boundaries. Starting from completely unmixed situations, spheres and spherotetrahedra would even mix and reach an homogeneous state that turns out to be independent of the initial situation.

Such experiments with non-spherical particles should be followed by others, for we believe that the behavior of granular media composed of non-spherical particles will lead to more interesting and unexpected findings. For shape-segregation alone, with the current version of our simulation code, investigating other kinds of mixtures still needs to be done. The influence of boundary conditions is another field with many open questions. Radial segregation should be investigated with a larger range of particle shapes and the boundary-driven shape-segregation may be related to the curvature of the confining boundaries. Observations on such experiments should lead to gain precious insights on the behavior of granular media composed of particles with arbitrary shapes.

# Bibliography


[AD99] S. Douady A. Daerr. Two types of avalanche behaviour in granular media. *Nature*, 399(6733):241–243, may 1999.

[ADS98] P. Alliez, O. Devillers, and J. Snoeyink. Removing degeneracies by perturbing the problem or the world. In *Proc. 10th Canad. Conf. Comput. Geom.*, 1998. INRIA Research Report 3316, 1997.

[Alg01] Algorithmic Solutions Software GmbH. LEDA, a Library of Efficient Data types and Algorithms. http://www.algorithmic-solutions.com/, 2001.

[AR01] B. Andrade and S. Reinmann. Simulation d'amas de grains sphériques. Projet de semestre, EPFL-DMA, 2001.

[AT87] M. P. Allen and D. J. Tildesley. *Computer simulation of liquids*. Clarendon Press, Oxford, 1987.

[ATC03] C. R. A. Abreu, F. W. Tavares, and M. Castier. Influence of particle shape on the packing and on the segregation of spherocylinders via monte carlo simulations. *Powder Tech.*, 134:167, 2003.

[Aur87] F. Aurenhammer. Power diagrams: properties, algorithms and applications. *SIAM J. Comput.*, 16(1):78–96, 1987.

[Aur88] F. Aurenhammer. Improved algorithms for discs and balls using power diagrams. *J. Algorithms*, 9:151–161, 1988.

[Bag05] K. Bagi. An algorithm to generate random dense arrangements for discrete element simulations of granular assemblies. *Granular Matter*, 7(1):31–43, 2005.

[Bar94] G. C. Barker. Computer simulations of granular materials. In A. Mehta, editor, *Granular Matter: An interdisciplinary approach*. Springer-Verlag, 1994.

[BEG+99] J. Basch, J. Erickson, L. J. Guibas, J. Hershberger, and L. Zhang. Kinetic collision detection for two simple polygons. In *Proc. 10th ACM-SIAM Sympos. Discrete Algorithms*, pages 102–111, 1999.

[BEKR03] A. J. P. Breu, H. M. Ensner, C. A. Kruelle, and I. Rehberg. Reversing the brazil-nut effect: Competition between percolation and condensation. *Phys. Rev. Lett.*, 90(1):014302, jan 2003.

[Ber99] R. Berger. Triangulations dynamiques en 3D avec LEDA. Projet de semestre, EPFL-DMA, 1999.

[Ber00] R. Berger. Simulation de la chute d'un bloc rocheux sur un remblai. Projet de semestre, EPFL-DMA, 2000.

[BGH97] J. Basch, L. J. Guibas, and J. Hershberger. Data structures for mobile data. In *Proc. 8th ACM-SIAM Sympos. Discrete Algorithms*, pages 747–756, 1997.

[BGSZ97] J. Basch, L. J. Guibas, C. D. Silverstein, and L. Zhang. A practical evaluation of kinetic data structures. In *Proc. 13th ACM Symposium on Computational Geometry*, pages 388–390, 1997.

[BGZ97] J. Basch, L. J. Guibas, and L. Zhang. Proximity problems on moving points. In *Proc. 13th ACM Symposium on Computational Geometry*, pages 344–351, 1997.

[BK94] R. Barriuso and A. Knies. *SHMEM User's Guide for C (Rev. 2.2)*. Cray Research Inc., 1994.

[BKS99] P. Bakucz, G. Krause, and D. Stoyan. Force distribution in loaded planar disc systems. In L. Gaul and C. A. Brebbia, editors, *Computational Methods in Contact Mechanics IV*, pages 273–282. WIT Press, Southampton/Boston, 1999.

[BNK03] D. L. Blair, T. Neicu, and A. Kudrolli. Vortices in vibrated granular rods. *Phys. Rev. E*, 67(3):031303, 2003.

[BSV01] H. Brönnimann, S. Schirra, and R. Veltkamp. The CGAL Reference Manual. http://www.cgal.org/Manual/, 2001.

[BY95] J.-D. Boissonnat and M. Yvinec. *Géométrie Algorithmique*. Ediscience international, Paris, 1995. Published in english as Algorithmic Geometry, Cambridge University Press, 1998.

[BY97] H. Bronnimann and M. Yvinec. Efficient exact evaluation of signs of determinants. In *Proc. 13th Annu. ACM Sympos. Comput. Geom.*, pages 166–173, 1997.

[CCC+97] R. Chandra, D. Chen, R. Cox, D. E. Maydan, N. Nedeljkovic, and J. M. Anderson. Data distribution support on distributed shared memory multiprocessors. In *Proc. SIGPLAN 97*, 1997.

[Cla99] Ph. Claudin. *La physique des tas de sable*. EDP Sciences, 1999.

[Cle98] P. W. Cleary. Discrete element modelling of industrial granular flow applications. *TASK Quarterly*, 2(3):385–415, 1998.

[CLM+95] P. Cignoni, D. Laforenzy, C. Montani, R. Perego, and R. Scopigno. Evaluation of parallelization strategies for an incremental Delaunay triangulator in E3. *Concurrency: Practice and Experience*, 7(1):61–80, 1995.

[CMPS93] P. Cignoni, C. Montani, R. Perego, and R. Scopigno. Parallel 3D Delaunay triangulation. *Computer Graphics Forum*, 12(3):129–142, 1993.

[CS79] P. A. Cundall and O. D. L. Strack. A discrete numerical model for granular assemblies. *Géotechnique*, 29(1), 1979.

[CS99] P. W. Cleary and M. L. Sawley. Three-dimensional modelling of industrial granular flows. In *Second International Conference on CFD in the Minerals and Process Industries*. CSIRO, Melbourne, Australia, 1999.

[CSSC95] J. Carreira, L. M. Silva, J. G. Silva, and S. Chapple. Implementing Virtual Shared Memories on MPI. In *MPI Developers Conference*, University of Notre Dame, June 1995.

[Cun88] P. A. Cundall. Formulation of a three-dimensional distinct-element model — Part I. A scheme to detect and represent contacts in a system composed of many polyhedral blocks. *Int. J. Rock Mech. Min. Sci. & Geomech. Abstr.*, 25(3), 1988.

[CW96] K. Chung and W. Weng. Quick collision detection of polytopes in virtual environments. In *Proc. 3rd ACM Sympos. Virtual Reality Software and Technology*, pages 125–132, 1996.

[CWBC98] M. E. Cates, J. P. Wittmer, J.-P. Bouchaud, and P. Claudin. Development in stresses in cohesionless poured sand. *Phil. Trans. R. Soc. Lond. A*, 356:2535–2560, 1998.

[DFM04] R. Dougherty, V. Faber, and M. Murphy. Unflippable tetrahedral complexes. *Discrete Comput. Geom.*, 32:309–315, 2004.

[DGKS96] O. Devillers, M. Golin, K. Kedem, and S. Schirra. Queries on Voronoi diagrams of moving points. *Comput. Geom. Theory Appl.*, 6:315–327, 1996.

[DH97] A. C. Davison and D. V. Hinkley. *Bootstrap Methods and Their Application*. Cambridge University Press, 1997.

[DL89] D. P. Dobkin and M. J. Laszlo. Primitives for the manipulation of three-dimensional subdivisions. *Algorithmica*, 4:3–32, 1989.

[dLRS04] J. A. de Loera, J. Rambau, and F. Santos. *Triangulations of point sets. Applications, structures, algorithms*. 2004. manuscript.

[dLSU99] J. A. de Loera, F. Santos, and J. Urrutia. The number of geometric bistellar neighbors of a triangulation. *Discrete Comput. Geom.*, 21:131–142, 1999.

[DMO05] E. D. Demaine, J. S. B. Mitchell, and J. O'Rourke. The open problems page, problem 28. Web page stating the conjecture, http://maven.smith.edu/~orourke/TOPP/P28.html, 2005.

[Dos98] G. Dos Reis. Vers une nouvelle approche du calcul scientifique en C++. Technical Report RR-3362, INRIA, 1998. http://www.inria.fr/rrrt/rr-3362.html.

[Dra91] T. G. Drake. Granular flow: physical experiments and their implications for microstructural theories. *J. Fluids. Mech.*, 12(225), 1991.

[DRC93] J. Duran, J. Rajchenbach, and E. Clément. Arching effect model for particle-size segregation. *Phys. Rev. Lett.*, 70(16):2431–2434, apr 1993.

[DS00] Y. Dai and A. Sutou. A study of the global optimization approach to spherical packing problems. Technical Report B-361, Tokyo Institue of Technology, May 2000. http://www.is.titech.ac.jp/research/research-report/B/.

[Dur00] J. Duran. *Sands, Powders, and Grains: An introduction to the Physics of Granular Materials*. Springer, 2000.

[Ede87] H. Edelsbrunner. *Algorithms in Combinatorial Geometry*. Springer-Verlag, 1987.

[EGSZ99] J. Erickson, L. J. Guibas, J. Stolfi, and L. Zhang. Separation-sensitive collision detection for convex objects. In *Proc. 10th ACM-SIAM Sympos. Discrete Algorithms*, pages 327–336, 1999.

[EM90] H. Edelsbrunner and E. P. Mücke. Simulation of simplicity: a technique to cope with degenerate cases in geometric algorithms. *ACM Trans. Graph.*, 6:66–104, 1990.

[EPW90] H. Edelsbrunner, F. P. Preparata, and D. B. West. Tetrahedrizing point sets in three dimensions. *J. Symbolic Comput.*, 10(3-4):335–347, 1990.

[ES96] H. Edelsbrunner and N. R. Shah. Incremental topological flipping works for regular triangulations. *Algorithmica*, 15:223–241, 1996.

[Fer01] J.-A. Ferrez. *Dynamic Triangulations for Efficient 3D Simulation of Granular Materials*. Thèse N° 2432, EPFL, 2001.

[FFDH90] S. Feiner, J. Foley, A. Van Dam, and J. F. Hughes. *Fundamentals of interactive computer graphics*. Addison Wesley, USA, 2nd edition, 1990.

[FL00] J.-A. Ferrez and Th. M. Liebling. Using dynamic triangulations in distinct element simulations. In M. Deville and R. Owens, editors, *Proceedings of the 16th IMACS World Congress*, August 2000.

[FL02] J.-A. Ferrez and Th. M. Liebling. Dynamic triangulations for efficient detection of collisions between sheres with applications in granular media simulations. *Phil. Mag. B*, 82(8):905–929, 2002.

[FLCA94] S. F. Foester, M. Y. Louge, H. Chang, and K. Allia. Measurement of the collision properties of small spheres. *Phys. Fluids*, 6(1108), 1994.

[FML00] J.-A. Ferrez, D. Müller, and Th. M. Liebling. Dynamic triangulations for granular media simulations. In K. R. Mecke and D. Stoyan, editors, *Statistical Physics and Spatial Statistics*, Lecture Notes in Physics. Springer, 2000.

[FV93] S. Fortune and Ch. J. Van Wyk. Efficient exact arithmetic for computational geometry. In *Ninth Annual Symposium on Computational Geometry*, pages 163–172, 1993.

[GB90] J. Ghaboussi and R. Barbosa. Three-dimensionnal discrete element method for granular materials. *Int J. for Numerical and Analytical Methods in Geomechanics*, 14(451), 1990.

[Gio80] A. Gioia. Intrinsic flowability: a new technology for powder-flowability classification. *Pharm. Tech.*, pages 65–68, february 1980.

[GKS92] L. J. Guibas, D. E. Knuth, and M. Sharir. Randomized incremental construction of Delaunay and Voronoi diagrams. *Algorithmica*, 7:381–413, 1992.

[GKZ94] I. M. Gel'fand, M. M. Kapranov, and A. V. Zelevinsky. *Discriminants, resultants, and multidimensional determinants, Mathematics: Theory & Applications*. Birkhäuser, Boston, 1994.

[GMR91] L. Guibas, J. S. B. Mitchell, and T. Roos. Voronoi diagrams of moving points in the plane. In *Proc. 17th Internat. Workshop Graph-Theoret. Concepts Comput. Sci.*, volume volume 570 of Lecture Notes in Computer Science, pages 113–125. Springer-Verlag, 1991.

[Gol91] D. Goldberg. What every computer scientist should know about floating-point arithmetic. *ACM Computing Surveys*, 23(1):5–48, 1991.

[GS85] L. Guibas and J. Stolfi. Primitives for the manipulation of general subdivisions and the computation of Voronoi diagrams. *ACM Transactions on Graphics*, 4(2):74–123, 1985.

[GZ98] L. J. Guibas and L. Zhang. Euclidean proximity and power diagrams. In *Proc. 10th Canadian Conference on Computational Geometry*, 1998.

[GZK90] I. M. Gel'fand, A. V. Zelevinskii, and M. M. Kapranov. Discriminants of polynomials of several variables and triangulations of newton polyhedra. *Leningrad Math J.*, 2:449–505, 1990.

[HKBS96] B. P. B. Hoomans, J. A. M. Kuipers, W. J. Briels, and W. P. M. Van Swaaij. Discrete particle simulation of bubble and slug formation in a two-dimensional gas-fluidised bed: a hard-sphere approach. *Chemical Engineering Science*, 51(1):99–118, 1996.

[HQL01] D. C. Hong, P. V. Quinn, and S. Luding. Reverse brazil nut problem: Competition between percolation and condensation. *Phys. Rev. Lett.*, 86(15):3423–3426, apr 2001.

[HSS83] J. E. Hopcroft, J. T. Schwartz, and M. Sharir. Efficient detection of intersections among spheres. *Intl. J. Robotics Research*, 2(4):77–80, 1983.

[IIM85] H. Imai, M. Iri, and K. Murota. Voronoi diagram in the Laguerre geometry and its applications. *SIAM J Computing*, 14(1):93–105, 1985.

[Ind95] C. Indermitte. *Modélisation et simulation de la croissance d'un mycélium*. Thèse N° 1404, EPFL, 1995.

[Joe89] B. Joe. Three-dimensional triangulations from local transformations. *SIAM J. Sci. Stat. Comput.*, 10(4):718–741, 1989.

[Joe91] B. Joe. Construction of three-dimensional Delaunay triangulations using local transformations. *Computer Aided Geometric Design*, 8:123–142, 1991.

[Joe92] B. Joe. Three-dimensional boundary-constrained triangulations. In E. N. Houstis and J. R. Rice, editors, *Artificial Intelligence, Expert Systems, and Symbolic Computing*, pages 215–222. Elsevier Science Publishers, 1992. ftp://ftp.cs.ualberta.ca/pub/geompack/Papers/Joe92.ps.Z.

[Joe93] B. Joe. Construction of k-dimensional Delaunay triangulations using local transformations. *SIAM J. Sci. Comput.*, 14(6):1415–1436, 1993.

[Joe95] B. Joe. Construction of three-dimensional improved-quality triangulations using local transformations. *SIAM J. Sci. Comput.*, 16:1929–1307, 1995.

[Joh85] K.L. Johnson. *Contact Mechanics*. Cambridge Univ. Press, New York, 1985.

[JS83] J. T. Jenkins and S. B. Savage. A theory for the rapid flow of identical, smooth, nearly elastic, spherical particles. *J Fluid Mech*, 130:187–202, 1983.

[KG99] P. Kuonen and R. Gruber. Parallel computer architectures for commodity computing and the Swiss-T1 machine. *EPFL Supercomputing Review*, 11, 1999. Online at http://sawww.epfl.ch/SIC/SA/publications/SCR99/scr11-page3.html.

[KJN93] J. B. Knight, H. M. Jaeger, and S. R. Nagel. Vibration-induced size separation in granular media - the convection connection. *Phys. Rev. Lett.*, 70(24):3728–3731, jun 1993.

[KK87] G. Kuwabara and K. Kono. Restitution coefficient in a collision between two spheres. *Jap. J. Appl. Phys.*, 26(1230), 1987.

[KMZ91] W. Kurz, J. P. Mercier, and G. Zambelli. *Introduction à la Science des Matériaux*, volume 1 of *Traité des Matériaux*. Presses Polythechniques et Universitaires Romandes, 2ème edition, 1991.

[Law77] C. L. Lawson. *Mathematical Software III*, chapter Software for $C^1$ interpolation. Academic Press, New York, 1977.

[LCB+94] S. Luding, E. Clément, A. Blumen, J. Rajchenbach, and J. Duran. Anomalous energy dissipation in molecular-dynamics simulations of grains: The "detachment" effect. *Phys. Rev. E*, 50(4113), 1994.

[LDCR05] S. Luding, J. Duran, E. Clément, and J. Rajchenbach. Simulations of dense granular flow: Dynamic arches and spin organization. *J. Phys. I*, 6(6):823–836, 2005.

[LL90] F. Lamarche and C. Leroy. Evaluation of the volume of intersection of a sphere with a cylinder by elliptic integrals. *Computer Phys. Comm.*, 59:359–369, 1990.

[LMB92] J. Levine, T. Mason, and D. Brown. *lex & yacc*. O'Reilly, 2nd edition, 1992.

[LMT+92] Th. M. Liebling, A. Mocellin, H. Telley, F. Righetti, H. Clémençon, and C. Indermitte. Nouvelles approches dans la modélisation et simulation de processus de croissance en science des matériaux et en biologie. *Cahiers du CERO*, 34:117–138, 1992.

[LNS+95] C. H. Liu, S. R. Nagel, D. A. Schecter, S. Majumdar, O. Narayan, and T. A. Witten. Force fluctuations in bead packs. *Science*, 269(5223):513–515, jul 1995.

[LRD97] L. Labous, A. D. Rosato, and R. N. Dave. Measurements of collisional properties of spheres using high-speed video analysis. *Phys. Rev. E*, 56(5717), 1997.

[Mak97] H. A. Makse. Stratification instability in granular flows. *Phys. Rev. E*, 56(6):7008–7016, dec 1997.

[Man88] M. Mantyla. *An introduction to solid modeling*. Computer Science Press, USA, 1988.

[MC95] B. Mirtich and J. Canny. *Impulse-based dynamic simulation, The agorithmic Foundations of robotics*. A. K. Peters, 1995.

[MD98] S.-A. Magnier and F. V. Donzé. Numerical simulation of impacts using a discrete element method. *Mech. Cohes.-frict. Mater.*, 3, 1998.

[Mei01] E. Meichtry. Simulation d'amas de grains sphériques. Projet de semestre, EPFL-DMA, 2001.

[MEL05] B. Muth, P. Eberhard, and S. Luding. Collisions between particles of complex shapes. In R. García-Rojo, H. J. Herrmann, and S. McNamara, editors, *Powders and Grains 2005*, volume II, pages 1379–1383. A.A.Balkema, 2005.

[Mir97] B. Mirtich. V-clip: Fast and robust polyedral collision detection. Technical Report TR-97-05, Mitsubishi Electrical Research Laboratory, 1997.

[ML95] D. Müller and Th. M. Liebling. Detection of collisions of polygons by using a triangulation. In M. Raous et al., editor, *Contact Mechanics*, pages 369–372. Plenum Publishing Corporation, New York, 1995.

[MLH00] H.-G. Matuttis, S. Luding, and H. J. Herrmann. Discrete element methods for the simulation of dense packings and heaps made of spherical and non-spherical particles. *Powder Technology*, 109(1-3):278–292, 2000.

[MLNJ01] M. E. Mobius, B. E. Lauderdale, S. R. Nagel, and H. M. Jaeger. Brazil-nut effect - size separation of granular particles. *Nature*, 414(6861):270, nov 2001.

[MMEL04] B. Muth, M.-K. Müller, P. Eberhard, and S. Luding. Contacts between many bodies. *Machine Dynamics Problems*, 28(1):101–114, 2004.

[MN99a] P. McCullagh and J. A. Nelder. *Generalized Linear Models*. Chapman and Hall/CRC, second edition edition, 1999.

[MN99b] K. Mehlhorn and S. Näher. *LEDA*. Cambridge University Press, 1999.

[Mon92] J. J. Monaghan. Smoothed particle hydrodynamics. *Annu. Rev. Astron. Astrophys.*, 30:543–574, 1992.

[Mon98] S. Montani Stoffel. *Sollicitation dynamique de la couverture des galeries de protection lors de chutes de blocs*. Thèse N° 1899, EPFL, 1998.

[MP00] E Meichtry and S. Paroz. Animations interactives de triangulations 3D. Projet de semestre, EPFL-DMA, 2000.

[MTT00] Y. Muguruma, T. Tanaka, and Y. Tsuji. Numerical simulation of particulate flow with liquid bridge between particles (simulation of centrifugal tumbling granulator). *Powder Technology*, 109:49–57, 2000.

[Mül96a] D. Müller. *Techniques informatiques efficaces pour la simulation de mileux granulaires par des méthodes d'éléments distincts*. Thèse N° 1545, EPFL, 1996.

[Mül96b] D. Müller. Web page with example simulations of granular media. http://rosowww.epfl.ch/dm/sigma.html, 1996.

[Mül98] D. Müller. Mieux comprendre les milieux granulaires. *IAS Bulletin*, 9, 1998.

[MY92] S. McNamara and W. R. Young. Inelastic collapse and clumping in a one-dimensional granular medium. *Phys. Fluids A*, 4(496), 1992.

[MY96] S. McNamara and W. R. Young. Dynamics of a freely evolving, two-dimensional granular medium. *Phys. Rev. E*, 53(5):5089–5100, may 1996.

[Müc93] E. Mücke. *Shapes and Implementations in Three-Dimensional Geometry*. PhD thesis, Department of Computer Science, University of Illinois at Urbana-Champaign, 1993. Technical Report UIUCDCS-R-93-1836, ftp://cs.uiuc.edu/pub/TechReports/UIUCDCS-R-93-1836.ps.Z.

[ND94] T.-T. Ng and R. Dorby. Numerical simulations of monotonic and cyclic loading of granular soil. *J. of Geotechnical Engineering*, 120(338), 1994.

[NSK03] M. A. Naylor, M. R. Swift, and P. J. King. Air-driven brazil nut effect. *Phys. Rev. E*, 68(1):012301, jul 2003.

[O'C96] R. M. O'Connor. *A distributed discrete element modeling environment - Algorithms, implementation and applications*. PhD thesis, MIT, 1996.

[PB95] T. Pöschel and V. Buchholtz. Molecular dynamics of arbitrary shaped granular particles. *J. Phys. I*, 5(1431), 1995.

[PL05a] L. Pournin and Th. M. Liebling. A generalization of distinct element method to tridimensional particles with complex shapes. In R. García-Rojo, H. J. Herrmann, and S. McNamara, editors, *Powders and Grains 2005*, volume II, pages 1375–1378. A.A.Balkema, 2005.

[PL05b] L. Pournin and Th. M. Liebling. Monotone paths in the flip-graph of regular triangulations. *Submitted*, 2005.

[PLM02] L. Pournin, Th. M. Liebling, and A. Mocellin. Molecular-dynamics force models for better control of energy dissipation in numerical simulations of dense granular media. *Phys. Rev. E*, 65:011302, 2002.

[Pou99] L. Pournin. Triangulations dynamiques pour la simulation de milieux granulaires. Projet de diplôme, EPFL-DMA, 1999.

[PRFL05] L. Pournin, M. Ramaioli, P. Folly, and Th. M. Liebling. A law for the flowability of bead assemblies. *Submitted*, 2005.

[Pri91] D. M. Priest. Algorithms for arbitrary precision floating point arithmetic. In P. Kornerup and D. Matula, editors, *Tenth Symposium on Computer Arithmetic*, pages 132–143. IEEE Computer Society Press, 1991.

[PWT+05] L. Pournin, M. Weber, M. Tsukahara, J.-A. Ferrez, M. Ramaioli, and Th. M. Liebling. Three-dimensional distinct element simulation of spherocylinder crystallization. *Granular Matter*, 7(2–3):119–126, 2005.

[Ramar] J. Rambau. On a generalization of schönhardt's polyhedron. *MSRI-Preprint 2003-013*, to appear.

[Rig92] F. Righetti. *Modélisation 3D d'amas polycristallins et méthodologie et méthodologie d'analyse de leurs images microscopiques*. Thèse N° 1016, EPFL, 1992.

[Ris00] G. H. Ristow. *Pattern formation in Granular Materials*. Springer Tracts in Modern Physics. Springer, 2000.

[RJMR96] F. Radjai, M. Jean, J.-J. Moreau, and S. Roux. Force distributions in dense two-dimensional granular systems. *Phys. Rev. Lett.*, 77(2):274–277, July 1996.

[Rog85] D. Rogers. *Procedural Elements for Computer Graphics*. McGraw Hill, 1985.

[RPL05a] M. Ramaioli, L. Pournin, and Th. M. Liebling. Numerical and experimental investigation of alignment and segregation of vibrated granular media composed of rods and spheres. In R. García-Rojo, H. J. Herrmann, and S. McNamara, editors, *Powders and Grains 2005*, volume II, pages 1359–1363, Rotterdam, 2005. A.A.Balkema.

[RPL05b] M. Ramaioli, L. Pournin, and Th. M. Liebling. Why rods align vertically under vertical vibrations. *Submitted*, 2005.

[RSPS87] A. Rosato, K. J. Strandburg, F. Prinz, and R. H. Swendsen. Why the brazil nuts are on top - size segregation of particulate matter by shaking. *Phys. Rev. Lett.*, 58(10):1038–1040, mar 1987.

[RTLM03] M. Rhodes, S. Takeuchi, K. Liffman, and K. Muniandy. The role of interstitial gas in the brazil nut effect. *Granular Matter*, 5(3):107–114, dec 2003.

[Sam84] H. Samet. The quadtree and related hierarchical data structures. *ACM Computing Surveys*, 16:187–260, 1984.

[San00a] F. Santos. A point configuration whose space of triangulations is disconnected. *J. Amer. Math. Soc.*, 13(3):611–637, 2000.

[San00b] F. Santos. Triangulations with very few geometric bistellar neighbors. *Discrete Comput. Geom.*, 23:15–33, 2000.

[SCB90] R. Sondergaard, K. Caney, and C. E. Brennen. Measurements of solid spheres bouncing off flat plates. *ASME J. Appl. Mech.*, 57(694), 1990.

[Sch28] E. Schönhardt. Über die zerlegung von dreieckspolyedern in tetraeder. *Math. Ann.*, 98:309–312, 1928.

[Sch99] A. Schinner. Fast algorithms for the simulation of polygonal particles. *Granular Matter*, 2(1):35–43, 1999.

[SDW96] J. Schäfer, S. Dippel, and D. E. Wolf. Force schemes in simulations of granular materials. *J. Phys. I*, 6(5), 1996.

[She96] J. R. Shewchuk. Robust adaptive floating-point geometric predicates. In *Proceedings of the Twelfth Annual Symposium on Computational Geometry*. ACM, 1996. http://www.cs.cmu.edu/~quake/robust.html.

[She97] J. R. Shewchuk. Adaptive precision floating-point arithmetic and fast robust geometric predicates. *Discrete & Computational Geometry*, 18:305–363, 1997. http://www.cs.cmu.edu/~quake/robust.html.

[She05] J. R. Shewchuk. General-dimensional constrained delaunay and constrained regular triangulations i: Combinatorial properties. *To appear in Discrete and Computational Geometry*, 2005. Available online at http://www.cs.cmu.edu/~jrs/jrspapers.html#cdt.

[Shi04] T. Shinbrot. Granular materials - the brazil nut effect - in reverse. *Nature*, 429(6990):352–353, may 2004.

[SM98] T. Shinbrot and F. J. Muzzio. Reverse buoyancy in shaken granular beds. *Phys. Rev. Lett.*, 81(20):4365–4368, nov 1998.

[SOB92] K. Sugihara, A. Okabe, and B. Boots. *Spatial Tesselations — Concepts and Applications of Voronoi Diagrams*. John Wiley, 1992.

[SSW00] H. Sigurgeirsson, A. Stuart, and W.-L. Wan. Collision detection for particles in a flow. http://www.maths.warwick.ac.uk/~stuart/hersir2.ps, 2000.

[Str97] B. Stroustrup. *The C++ Programming Language*. Addison Wesley, 3rd edition, 1997.

[STS93] M. H. Sadd, Q. Tai, and A. Shukla. Contact law effects on wave propagation in particulate materials using distinct element modeling. *Int. J. Non-Linear Mechanics*, 28(251), 1993.

[Tel89] H. Telley. *Modélisation et simulation bidimensionnelle de la croissance des polycristaux*. Thèse N° 780, EPFL, 1989.

[The01] The CGAL Team. CGAL, Computational Geometry Algorithm Library. http://www.cgal.org/, 2001.

[TLM96a] H. Telley, Th. M. Liebling, and A. Mocellin. The Laguerre model of grain growth in two dimensions: Part I. Cellular structures viewed as dynamical Laguerre tesselations. *Phil. Mag. B*, 73(3):395–408, 1996.

[TLM96b] H. Telley, Th. M. Liebling, and A. Mocellin. The Laguerre model of grain growth in two dimensions: Part II. Examples of coarsening simulations. *Phil. Mag. B*, 73(3):409–427, 1996.

[TSBP93] Y. A. Teng, F. Sullivan, I. Beichl, and E. Puppo. A data-parallel algorithm for the three-dimensional Delaunay triangulation and its implementation. In *Proceedings of Supercomputing '93, Portland, Oregon*, pages 112–121, 1993.

[Tsu03] M. Tsukahara. Simulations numériques de milieux granulaires avec des grains cylindriques. Projet de diplôme, EPFL-SB-IMA-ROSO, 2003.

[VLMJ00] F. X. Villarruel, B. E. Lauderdale, D. M. Mueth, and H. M. Jaeger. Compaction of rods : Relaxation and ordering in vibrated, anisotropic granular material. *Phys. Rev. E*, 61(6):6914, 2000.

[WB86] O. R. Walton and R. L. Braun. Viscosity, granular-temperature, and stress calculations for shearing assemblies of inelastic, frictional discs. *J. of Rheology*, 30(949), 1986.

[WB93] O. Wenzel and N. Bicanic. A quad tree based contact detection algorithm. In *Proceedings of the 2nd international conference on discrete element methods (DEM), MIT*. IESL Publications, 1993.

[Wei00] Ch. Weibel. Parallélisation d'un algorithme de simulation de milieux granulaires. Projet de diplôme, EPFL-DMA, 2000.

[XRT+97] X. Xue, F. Righetti, H. Telley, Th. M. Liebling, and A. Mocellin. The Laguerre model for grain growth in three dimensions. *Phil. Mag. B*, 75(4):567–585, 1997.

[Xue95] X. Xue. *Laguerre models for grain growth*. Thèse N° 1466, EPFL, 1995.

**Lionel Pournin** rosowww.epfl.ch/lp
Born December 22, 1975 lionel.pournin@epfl.ch

## EDUCATION

**1999 – 2005** **École Polytechnique Fédérale de Lausanne**, Lausanne, Switzerland: www.epfl.ch
*PhD student in Operations Research, Institute of Mathematics,*
*under the supervision of Prof. Th. M. Liebling.*
*Thesis subject: "on the behavior of spherical and non-spherical grain assemblies,*
*its modeling and numerical simulation".*

**1996 – 1999** **École Nationale Supérieure des Mines de Nancy**, Nancy, France: mines.u-nancy.fr
*Engineering degree obtained june 1999,*
*(Diplôme d'ingénieur civil des Mines de Nancy).*
*Master equivalent degree in materials science obtained september 1999,*
*(DEA de science et ingénieurie des materiaux).*

**1997 – 1998** **Henri Poincaré University (Nancy II)**, Nancy, France: www.uhp-nancy.fr
*Bachelor equivalent degree in mathematics obtained june 1998,*
*(Maîtrise de mathématiques).*

**1993 – 1996** **Lycée Chaptal**, Paris, France: www.lycee-chaptal-paris.com
*Classes préparatoires de mathématiques supérieures et spéciales M'.*

**1990 – 1993** **Lycée Honoré de Balzac**, Mitry-Mory, France:
*Baccalauréat C (scientific) obtained june 1993.*

## PROFESSIONAL EXPERIENCE

**2005 – 2006** **EPFL – Institute of Mathematics, Lausanne**: roso.epfl.ch/cours/rosc/hiver05-06/
*Lecturer of the operations research course for 5th semester students*
*in Communication Systems, winter semester.*

**1999 – 2005** **EPFL – Institute of Mathematics, Lausanne**: roso.epfl.ch/lp/teaching.html
*Assistant of Prof. Th. M. Liebling, chair of Operations Research.*

## PUBLICATIONS

**2005** L. Pournin, M. Weber, M. Tsukahara, J.-A. Ferrez, M. Ramaioli, Th. M. Liebling, *Three-dimensional distinct element simulation of spherocylinder crystallization*,
Granular Matter 7, 2-3, 119-126 (2005).

**2002** L. Pournin, Th. M. Liebling, and A. Mocellin, *Molecular-dynamics force models for better control of energy dissipation in numerical simulations of dense granular media*,
Phys. Rev. E 65, 011302 (2002).

## VARIOUS

**Languages**: Fluent in **French** and **English**, good knowledge of **Romanian**, basic knowledge of **German**.
*CAE (Cambridge Certificate in Advanced English) obtained december 1997.*
*ZDAF (Zertifikat Deutsch als Fremdsprache) obtained march 1999.*